MODELLING OF HIGH TEMPERATURE METHANOL-FUELLED SOLID OXIDE FUEL CELLS

XU QIDONG

PhD

The Hong Kong Polytechnic University

2023

The Hong Kong Polytechnic University
Department of Building and Real Estate

Modelling of High Temperature Methanol-Fuelled Solid Oxide Fuel Cells

Xu Qidong

A thesis submitted in partial fulfilment of the requirements for the degree of Doctor of Philosophy

February 2023

CERTIFICATE OF ORIGINALITY

I hereby declare that this thesis is my own work and that, to the best of my knowledge and belief, it reproduces no material previously published or written, nor material that has been accepted for the award of any other degree or diploma, except where due acknowledgement has been made in the text.

_____ (Signed)

_____Xu Qidong_____ (Name of student)

ABSTRACT

Solid oxide fuel cells (SOFCs) have been recognized as one of the most important energy conversion technologies due to high energy efficiency and low emission. In addition, fuel flexibility is the most significant advantage of SOFCs since direct utilization of the carbon-containing fuel (alkanes, alcohols, biomass etc.) is possible at the typical high operating temperature of SOFCs. Among these fuels, Methanol is a promising fuel for SOFCs due to its easy storage and transportation compared with hydrogen. However, in the current literature, computer simulation work on methanol-fuelled SOFCs is limited, and comprehensive understandings of chemical reactions, gas composition and temperature distributions inside the SOFC are unclear. Therefore, a 2D numerical model is developed to study a tubular direct methanol SOFC.

A simulation model without considering the heat transfer is developed to study a tubular direct methanol SOFC. The model fully considers the methanol decomposition reaction (MDR) and water gas shift reaction (WGSR) in the anode, electrochemical oxidations of H_2 and CO, fluid flow and mass transfer in the cell. The model is validated by the direct methanol SOFC experiment. At a temperature of 1073K, a peak power density of 1.3 W cm^{-2} is achieved, which is much higher than room temperature direct methanol fuel cells (typically less than 0.1 W cm^{-2}). Subsequent parametric simulations are conducted to understand the effects of operating and structural parameters on the SOFC performance, such as temperature, potential, anode thickness and cell length. Increasing the temperature enhances chemical/electrochemical reaction rates and ion conduction, leading to improved cell performance. Increasing the anode thickness improves methanol conversion and increases the average current density to some extent. For comparison, a longer cell can also improve methanol conversion but decreases the average cell current density.

Thermo-electrochemical modelling study is subsequently conducted to consider heat transfer effects on the electrochemical performance of a methanol-fuelled SOFC. Parametric simulations are performed to investigate the effects of operating potential, steam to carbon ratio, inlet temperature and fuel/air flow rates on the performance of SOFCs. At 1073K, the peak power density of methanol-fuelled SOFC is higher than 10000 W m^{-2} with a steam to carbon ratio of 1. In addition, the temperature distribution in SOFC could be remarkably affected by the working conditions because of chemical/electrochemical reactions and overpotential losses. Large temperature variation (nearly 180 K) between the inlet and outlet is observed mainly due to greatly improved current density at a low operating potential. Also, temperature reduction could be achieved by increasing the steam to carbon ratio and gas flow rates (higher than 170 SCCM for air and 0.1 ml min^{-1} for fuel mixture, respectively), which could improve the long-term stability from the perspective of thermal stress but inevitably lower the efficiency of SOFC. Meanwhile, higher inlet temperature not only enhances the power output but improves the uniformity of cell temperature distribution.

Further investigation on thermal responses of methanol-fuelled SOFC is also conducted since thermal management is a challenging issue given the non-uniform electrochemical reactions and convective flows within SOFCs. Results show that unlike the low-temperature condition of 873 K where peak temperature gradient occurs in the cell centre, it is likely to appear near the fuel inlet because of rapid temperature rise induced by elevated current density at 1073 K. Despite large heat convection capacity, excessive air could not effectively eliminate the harmful temperature gradient caused by large current density. Fortunately, well control of current density by properly selecting operating potential could result in a local thermal neutral state. Interestingly, the maximum axial temperature gradient could be reduced by about 18% at 973 K and 20% at 1073 K when the air with a 5 K higher temperature is supplied. Also, despite the higher electrochemical performance observed, the cell with a counter-flow

arrangement featured by a larger hot area and higher maximum temperature gradients is not preferable for a ceramic SOFC system considering thermal durability.

The results of the current study form a basis for subsequent performance enhancement of methanol-fuelled SOFCs by optimization of the cell structure and operating parameters. Besides, this study could also provide insightful thermal information for operating condition selection, structure design and stability assessment of realistic SOFCs running on methanol fuel.

AUTHOR'S PUBLICATIONS

[1] **Xu Q**, Ni, M. Modelling of high temperature direct methanol solid oxide fuel cells. International Journal of Energy Research. 2021;45:3097-112.

[2] **Xu Q**, Xia L, He Q, Guo Z, Ni M. Thermo-electrochemical modelling of high temperature methanol-fuelled solid oxide fuel cells. Applied Energy. 2021;291:116832.

[3] **Xu Q**, Guo Z, Xia L, He Q, Li Z, Bello IT, Zheng K, Ni M. A comprehensive review of solid oxide fuel cells operating on various promising alternative fuels. Energy Conversion and Management. 2022;253:115175.

[4] **Xu Q**, Guo M, Xia L, Li Z, He Q, Zhao D, Zheng K, Ni M. Temperature gradient analyses of tubular SOFC fuelled by methanol fuel. Transactions of Tianjin University, Accepted.

ACKNOWLEDGEMENTS

First of all, I would like to express my highest respect and sincerest gratitude to my supervisor, Professor NI Meng. Under his careful guidance, considerable support and generous help, I was able to complete my research study during the Ph.D. period. His enthusiasm for academic research and modest attitude towards life are the wealth of my life and could always inspire me to move forward. I am very grateful and lucky to have Professor NI Meng as my supervisor. Take this opportunity, I hope Professor NI could be happy every day and work smoothly.

Great thanks to Professor Keqing ZHENG from China University of Mining and Technology, her kind suggestions on my research helped me a lot.

Meanwhile, I also want to thank all the group members in PolyU, including Dr. XU Haoran, Dr. Chen Bin, Dr. GUO Meiting, Dr. LIAO Tianjun, Dr. ZHANG Zhenbao, Dr. YU Jie, Dr. LIU Tong, Dr. GUAN Daqin, Dr. WANG Bowen, Dr. DAI Yawen, Dr. Zhai Shuo, CHENG Chun, HE Qijiao, XIA Lingchao, GUO Zengjia, ZHAO Siyuan, LI Zheng, YU Na, WANG Chen, ZHU Meng, WANG Yang, XIE Biao and ZHAO Dongqi. Thanks for their kind help and generous supports.

Besides, many thanks to our university and BRE department. I will always cherish the moments of those days at PolyU. Importantly, congratulations on the 85th anniversary of PolyU.

Thanks to my family for their unconditional love. Thanks to my girlfriend for her ongoing support. It's because of you that I could be fully engaged in my study. Thank you and I do love you all.

TABLE OF CONTENTS

LIST OF FIGURES

LIST OF TABLES

LIST OF ABBREVIATIONS

AFC	Alkaline fuel cell
BSCF	Strontium-doped barium cobalt ferrite
CHP	Combined heat and power
GDC	Gadolinium-doped ceria
HHV	Higher heating value
LSCF	Strontium-doped lanthanum cobalt ferrite
LSGM	Strontium and magnesium-doped lanthanum gallate
LSM	Strontium-doped lanthanum manganite
MCFC	Molten carbonate fuel cell
MDR	Methanol decomposition reaction
MIEC	Mixed ionic/electronic conducting
O/C	Oxygen to carbon
OCV	Open-circuit voltage
ORR	Oxygen reduction reaction
OSC	Oxygen storage capacity
PAFC	Phosphoric acid fuel cell
PEMFC	Proton exchange membrane fuel cell
P_{max}	Maximum power density
SCCM	Standard cubic centimetre per minute
S/C	Steam to carbon
SDC	Samarium-doped ceria
SEM	Scanning electron microscopy
SOFC	Solid oxide fuel cell

TEC	Thermal expansion coefficient
TPB	Triple phase boundary
WGSR	Water gas shift reaction
YSZ	Yttria-stabilized zirconia

Roman

C_p	Heat capacity, J mol^{-1} K^{-1}
D_{ij}	Binary diffusion coefficient of *i* and *j*, cm^2 s^{-1}
D_{ik}	Knudsen diffusion coefficient of *i*, cm^2 s^{-1}
D_{ij}^{eff}	Effective binary diffusion coefficient of *i* and *j*, cm^2 s^{-1}
E	Equilibrium Nernst potential, V
F	Faraday constant, 96,485 C mol^{-1}
ΔG	Gibbs free energy, kJ mol^{-1}
h	Enthalpy of formation, kJ mol^{-1}
ΔH	Enthalpy change of formation, kJ mol^{-1}
i	Current density, A m^{-2}
i_0	Exchange current density, A m^{-2}
J_i	Molar diffusion flux of species *i*, mol m^{-2} s^{-1}
M_i	Molecular weight of species *i*, kg mol^{-1}
n	Number of electrons transferred per electrochemical reaction
N_i	Molar flux of species *i*, mol m^{-2} s^{-1}
p	(partial) Pressure, Pa
Q_e	Energy source, W m^{-3}
Q_m	Mass source, kg m^{-3} s^{-1}
r	Mean pore radius, m
R	Gas constant, 8.3145 J mol^{-1} K^{-1}

R_r	Rate of chemical reaction, mol m^{-3} s^{-1}
R_i	Rate of generation or consumption of species *i*, mol m^{-3} s^{-1}
S	Entropy, J mol^{-1} K^{-1}
ΔS	Entropy change, J mol^{-1} K^{-1}
S_{TPB}	Specific surface area, m^2 m^{-3}
T	Temperature, K
u	Molar-averaged velocity, m s^{-1}
U	Mass-averaged velocity, m s^{-1}
V	Volume fraction
y_i	Molar fraction of species *i*

Greek letters

α	Charge transfer coefficient
ε	Porosity
η	Polarization, V
κ	Permeability, m^2
λ	Thermal conductivity, W m^{-1} K^{-1}
μ	Dynamic viscosity of gas mixture, Pa s
μ_i	Dynamic viscosity of species *i*, Pa s
ρ	Mass concentration of the mixture or the density, kg m^{-3}
σ	Electrical conductivity, S m^{-1}
τ	Tortuosity

Subscripts

a	Anode
act	Activation
c	Cathode

che	Chemical reaction
ele	Electrochemical reaction
g	Gas mixture
i	Species *i*
l	Ionic phase
s	Electronic phase
sol	Solid phase

Superscripts

eff	Effective
l	Local

Chapter 1: Research background

1.1 Introduction

With the ongoing development of the economy and rapid urbanization [1], research focusing on renewable resources such as solar, wind, tide and nuclear energies has received more and more attention [2,3]. However, owing to these alternatives' site-specific, intermittent, unstable and unpredictable natures [4], traditional fossil fuels (coal, oil and natural gas) have still been the world's principal energy sources [5]. Unfortunately, serious issues related to the current electricity generation technology which highly relies on carbon-containing fossil fuels are inefficiency and severe environmental pollution since the efficiency of the conventional thermal power plant is only about 40% because of the Carnot-cycle limitation, leading to much energy loss, and the massive increase in CO_2 concentration caused by the combustion process is the main reason for the global warming effect [6]. Therefore. considering the continuously decreasing carbonaceous fuel stock, cleaner and more effective energy conversion devices directly utilising fossil fuels have become more significantly essential for future energy sustainability and environmental issues mitigation.

Solid oxide fuel cells (SOFCs) are promising means which can directly convert chemical energy into electrical power through electrochemical reactions with a higher conversion efficiency (typically 50%) than conventional thermal power or combustion technology (40% or lower [7]). To ensure moderate ionic conductivity of the solid ceramic electrolyte, SOFCs normally operate at a temperature from 600 ° to 1000 ℃ to overcome high activation energy [8]. High operating temperature brings numerous advantages to SOFCs over other types of fuel cell (Table 1.1), such as high tolerance to fuel impurities [9]; the use of low-cost nickel catalyst instead of the prohibitively expensive platinum group metals [10]; the electrochemical utilization of carbon monoxide, one reducing gas species which may be catastrophic to other

low-temperature fuel cells like PEMFCs (proton exchange membrane fuel cells), thus reducing the requirements for gas cleaning or pre-treatment equipment [11]; and the feasible occurrences of endothermic internal reforming reaction or pyrolysis of combustible fuels, thereby producing the direct electrochemical fuels (hydrogen and carbon monoxide). In addition, the hybrid system efficiency can be up to 70% when the high-quality waste heat generated from SOFCs is recovered by the gas turbine, the CHP (combined heat and power) application [12] or other thermodynamic cycles [13,14].

Table 1.1 Typical characteristics of different fuel cells.

Types of fuel cells	Electrolyte	Operating temperature (℃)	Catalyst	Fuel
PEMFC	Proton exchange membrane	60-200	Platinum	Hydrogen
AFC	Potassium hydroxide	60-220	Platinum	Hydrogen
PAFC	Phosphoric acid	160-220	Platinum	Hydrogen
MCFC	Molten Carbonate	630-650	Nickel	Hydrogen, methane
SOFC	Ceramic	600-1000	Nickel, perovskite	Hydrogen, hydrocarbon etc.

1.2 Structure, principle, and components of SOFCs

SOFC is a whole solid-state device consisting of an ion-conductive solid ceramic electrolyte sandwiched between the porous fuel electrode (anode) and porous air electrode (cathode) [15], which is why SOFCs can operate silently (Figure 1.1). Similar to other types of fuel cells, SOFCs are supplied with the fuel in the anode channel and the air in the cathode channel which are physically separated by the dense impermeable electrolyte film, so the oxidation products (e.g., CO_2) could be easily captured via the condensation process of exhaust emission (mixture of steam and carbon dioxide, if hydrocarbon is used as the fuel). Oxygen molecules are reduced to oxygen anions at TPB (triple phase boundary) sites in the cathode (Eq. (1.3)) by the electrons conducted, and due to the oxygen chemical potential gradient, ions are transported through the ceramic electrolyte (ion conductor) into the TPB sites of anode where the direct fuels can be

electrochemically oxidized to release electrons which are simultaneously transferred into the porous cathode through the external circuit to generate the usable electricity power (Eqs. (1.1) and (1.2)). As long as the fuel and air are continuously supplied to SOFCs, the external load can operate unendingly because of the continuous electrochemical reactions.

$$H_2 + O^{2-} \rightarrow H_2O + 2e^- \quad (1.1)$$

$$CO + O^{2-} \rightarrow CO_2 + 2e^- \quad (1.2)$$

$$0.5O_2 + 2e^- \rightarrow O^{2-} \quad (1.3)$$

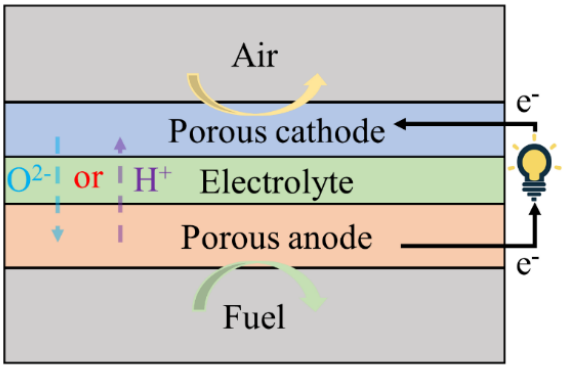

Figure 1.1 The schematic of the Solid Oxide Fuel Cell.

Based on the SOFC principle and the function of each component, anode, cathode, and electrolyte need to be equipped with specific properties by fabricating particular materials. The latest material advances of these three components could be found in various excellent review papers available in the literature [16–20], so only several frequently used materials will be briefly introduced in this section.

1.2.1 Electrolyte

For electrolyte, the permeability must be sufficiently low to separate the gases in both sides. Besides, the high ionic conductivity and extremely low electronic conductivity which minimizes the leakage current need to be maintained at high operating temperature, strong reducing (anode side) and oxidizing (cathode side) environments. State-of-the-art material for electrolyte is YSZ (yttria-stabilized zirconia, ZrO_2 + 8 mol% Y_2O_3), which is commonly used

in high-temperature SOFCs (HT-SOFCs, >850℃), so-called since yttria is doped to stabilize ZrO_2 into cubic fluorite phase instead of the unstable crystalline structure of undoped ZrO_2 and 8 mol% dopant is used to maximize the oxygen ionic conductivity of YSZ (0.1 S cm^{-1} at 1000 ℃) [21]. Typically, anode-supported YSZ-based SOFCs need to operate at a temperature above about 973 K to achieve feasible ionic conductivity (0.01 S cm^{-1} at 700 ℃) when the typical electrolyte thickness of 10 μm is assumed [17]. However, for lower working temperatures, doped-ceria is one of the most successful materials for electrolytes, such as SDC (samarium doped ceria, $Sm_xCe_{1-x}O_2$) and GDC (gadolinium doped ceria, $Gd_xCe_{1-x}O_2$), which show high conductivity, particularly in the low or intermediate temperature range from 500 ° to 750 ℃. However, doped-ceria is likely to suffer chemical instability at low oxygen fugacity (fuel electrode side) due to the redox cycle of cerium cation, which causes substantial electronic conductivity and leads to internal shorting and low OCV (open-circuit voltage) [22]. Different from doped-ceria, lanthanum strontium gallium magnesium (LSGM, Sr and Mg-doped $LaGaO_3$) with the perovskite structure possesses adequate ionic conductivity and negligible electronic conductivity at relatively low oxygen pressure, and the minimum operating temperature for LSGM is the same as that of GDC (550 ℃) [23]. However, some material compatibility problems hinder the application of thin LSGM, such as nickel interdiffusion and La loss [17]. Fortunately, these issues mentioned above related to doped-ceria and LSGM could be well addressed by a bi-layer electrolyte structure, which could incorporate the best properties of each electrolyte material [17].

Electrolyte normally contributes the most of ohmic resistance in SOFC due to the inefficiency of its ionic conduction, so electrolyte thickness reduction and utilization of high ionic-conducting electrolyte materials enable SOFCs to operate at lower temperatures, which could offer numerous benefits to the fuel cell system. Firstly, a wide range of materials for components could be used with simpler and more economical fabrication approaches; secondly,

low temperature means quick start-up or shut-down time and also ease the problems such as the sintering or grain growth of metallic phase in the anode, which in turn improves the thermal stability and prolongs the lifetime of fuel cells. Furthermore, intermediate temperature and low-temperature SOFCs (IT-SOFCs, 650 ° to 850 ℃ and LT-SOFCs, 400 ° to 650 ℃) show great potential in the application of transportation and portable devices with significant long-term economic and environmental benefits [9].

1.2.2 Cathode

The oxygen reduction reaction (ORR) takes place in the cathode, so the cathode material possessing a wonderful catalytic effect can truly improve SOFC performance since the biggest polarization loss is related to ORR. LSM perovskite-type oxide (strontium-doped lanthanum manganite, $La_xSr_{1-x}MnO_3$) is the most commonly used material for the cathode of HT-SOFC because LSM shows an excellent catalytic effect and high electronic conductivity in the temperature from 800 ° to 1000 ℃ [24]. However, LSM does not seem to be the optimal choice for intermediate or low temperatures because of the high activation energy and increased polarization resistance as a result of insufficient catalytic activity below 700 ℃ [25]. Therefore, for the temperature from 500 ° to 700 ℃, the cobalt-containing MIEC (mixed ionic/electronic conducting) materials like strontium-doped lanthanum ferro-cobaltite (LSCF, $La_{1-x}Sr_xCo_{1-y}Fe_yO_{3-\delta}$) [26] and strontium-doped barium ferro-cobaltite (BSCF, $Ba_{1-x}Sr_xCo_{1-y}Fe_yO_{3-\delta}$) [27] have received more attention due to their enhancements of cathode reaction kinetic and ionic conductivity. In addition, the distinguishing feature of MIEC cathode materials is that the TPB region is intrinsically expanded to the entire gas-cathode interface because of their mixed ionic/electronic conductive property [25]. Although LSCF cathode shows reactivity with YSZ electrolyte, forming a $La_2Zr_2O_7$ insulation layer, this problem could also be mitigated by inserting a ceria-based buffer layer into the interface between electrolyte and cathode to form

a bi-layer electrolytes structure since ceria shows more stable compatibility with LSCF cathode [8].

1.2.3 Anode

Anode is the component where fuel oxidation (e.g., hydrogen oxidation reaction) or reforming reactions occur. Therefore, the requirements for the anode involve sufficient ionic and electronic conductivities as well as an active catalytic effect for chemical/electrochemical reactions [15]. Similar to the cathode, anode is also a porous composite electrode of electronic conductor and ionically conductive ceramic, usually the same material as electrolyte. Nickel metal is the most advanced material for anode electronic phase because of its high intrinsic electronic conductivity of metal, excellent electrocatalytic activity and low cost. Besides, nickel is also the best reforming catalyst for many carbon-containing fuels, so the internal reforming reaction is possible if SOFCs operate on other promising fuels. The preferred anode ionic phase is YSZ or doped-ceria which provides enough ionic conductivity into the depth of the anode layer and also lowers the thermal expansion coefficient of the composite anode to achieve good thermal compatibility with YSZ or doped-ceria electrolyte since Ni has a relatively higher TEC than that of these electrolytes [15]. In addition, the presence of an ionic phase in anode can present a framework as a sintering inhibitor to prevent the grain growth of Ni particles since the agglomeration or interdiffusion of Ni grains is likely to occur at elevated temperatures [8].

The optimizations of microstructure and composition of the anode are also important to improve the performance of SOFCs by achieving the lowest overpotential losses [28]. Although Ni metal has high electronic conductivity (about 20,000 S cm^{-1} at 1000 ℃), the conductivity of Ni-YSZ can be more than a factor of 10 lower than that of bulk nickel metal because of possible not well-connected metallic phase, porosity, tortuosity and the nature of composite electrode. Therefore, 30-60 vol% Ni is typically recommended since the cermet

cannot meet the requirement of sufficient electronic conductivity and suffers from higher ohmic polarization resistance if the content of Ni phase is less than 30 vol% of anode solid phase [29]. In addition, the optimum volume of gas phase is essential to facilitate the easy diffusion of direct fuel gases into electrochemical active sites and the better transportation of reaction products away from the anode to minimize concentration overpotential loss, and the gas phase is also one important component of the TPB, which is directly related to the rate of electrochemical reactions. Therefore, for efficient functioning, Ni-YSZ porous anode is expected to be constituted by 30-35 vol% porosity [12]. In general, good chemical and thermal stability as well as excellent performance make Ni-YSZ cermet anode still attractive presently [18,30].

However, despite the tremendous advantages of Ni-YSZ composite cermet, several serious deactivation issues could be caused if SOFCs directly operate on alternative fuels, which will be detrimental to the performance and durability of anode catalyst [15]. For example, Carbon deposition has been considered one of the serious issues when SOFC is fed by carbon-containing fuels [10]. Therefore, to tackle this shortcoming, numerous strategies have been employed to enhance the coking stability and thus increase cell lifetime [31].

1.3 Recent research on the methanol-fuelled SOFCs

Hydrogen has been globally identified as the ideal fuel for fuel cells [32,33] because hydrogen could be efficiently electrochemically oxidized without any greenhouse gases emission [4,34]. Besides, the higher heating value (HHV) of hydrogen can be up to 141.9 MJ kg^{-1} which is the highest compared to any existing fossil fuel except nuclear energy [35]. However, although the share of hydrogen production from renewable technologies such as biomass-based approaches [36] and water electrolysis driven by alternative energies [37] is continually increasing in the future [38], global hydrogen production mainly relies on fossil fuel feedstock, accounting for 90% [39]. In addition, extreme strict requirements for hydrogen

storage and transportation have also been the challenges which impede the wide-scale application of hydrogen [40], because it is difficult and thus expensive to transport, store and distribute hydrogen in the liquid state which has a comparable volumetric energy density to liquid hydrocarbon [10]. Moreover, the low ignition energy and wide flammability range of hydrogen impose an undesired risk to the fuel cell community [41].

Fuel flexibility could be one of the most promising traits of SOFCs since high operating temperature benefits chemical reaction kinetics in the electrode. Besides, oxygen ions transferred from the cathode could oxidise any reductive fuels so, in principle, it is possible to utilize a wide range of fuels, including gaseous state fuels such as gaseous alkanes and ammonia, liquid fuels like alcohols and liquid alkanes, or even the solid phase fuels including the activated carbon, coal and biomass. Therefore, due to these unsolved problems and drawbacks of hydrogen as well as the innate characteristic of SOFCs, more and more researchers have shifted their focus to the direct operation of SOFCs on other promising fuels [42–45].

The physical state of fuel under atmospheric conditions is an important factor for the fuel suitability and applicability of SOFCs since liquid fuel could be conveniently stored, transported, and distributed with the existing gasoline supply chain. Therefore, the direct utilization of oxygenated liquid hydrocarbons, such as alcohols primarily including methanol and ethanol fuels, in SOFCs has received much attention from researchers. Unlike liquid higher hydrocarbons (e.g., octane), alcohols exhibit less coking risk due to fewer carbon atoms and the intrinsic relatively high oxygen/carbon ratio in their chemical structures. However, carbon formation is still a deteriorative cause for SOFCs directly running on alcohol fuels, especially for ethanol [11,46,47]. For example, the delamination of Ni-YSZ anode caused by severe carbon deposits was observed for both OCV and the current load (0.6 V) conditions after the 12 hours of operation when pure methanol was used as the fuel at 800 ℃ [48]. Besides, the

electrolyte-supported SOFC with the thin Ni-YSZ anode completely failed after the 10 h in the fuel mixture of ethanol and steam with the S/C ratio of 3.1 under a constant current of 20 mA at 800 ℃ [49]. Despite these, promising characteristics of methanol and ethanol fuels, involving complete miscible nature with water, relatively high volumetric energy density, liquid state at normal conditions and less coking threatening [8,31], have enabled the researchers to develop more durable and powerful alcohol-fuelled SOFCs. More importantly, both methanol and ethanol could be generated from biomass sources [4,11,50,51], which indicates that integrating direct alcohol SOFC with renewable bio-fuels production could provide an efficient and carbon-neutral power production technology to the SOFC community, benefiting both environment and economy.

Methanol has been considered the convenient carrier for syngas because methanol is primarily generated based on the reforming of natural gas in the current industry [50]. Besides, thanks to the absence of a C-C bond in the molecular structure, methanol can be conveniently decomposed back to the hydrogen-rich gas mixture at the typical operating temperature of SOFCs, because the frequently used anode metal phase of Ni metal could predominantly catalyse the methanol decomposition process, followed by the kinetically slower water gas shift reaction in the presence of steam [52]. Besides, based on experimental observations, the mixture of carbon monoxide and hydrogen with an approximate ratio of 2 was the main product of Ni-based anode off-gas when pure methanol was used as the fuel [48], which was consistent with the thermodynamic analysis [53]. Therefore, because of the easy decomposition nature of methanol under the catalytic effect of nickel cermet, methanol-fuelled SOFC tends to show excellent electrochemical performance, which has been proved by various studies. For example, an experimental test conducted by Sasaki et al [54] indicated that direct-methanol SOFC showed the comparable current-voltage characteristic to that of simulated complete reformed gas (the mixture of carbon monoxide and hydrogen with a molar ratio of 2:1) at 1000 ℃. In

addition, maximum power densities of 0.6 and 1.3 W cm^{-2} at 650 ℃ and 800 ℃, respectively, were achieved when Ni-YSZ anode-supported SOFC operated on pure methanol [55]. Besides, with a more effective low-temperature electrolyte material of SDC, more excellent performance with a P_{max} (Maximum power density) of 698 mW cm^{-2} at 650 ℃ was obtained with pure methanol fuel [56]. Moreover, methanol-fuelled SOFC presented a P_{max} of 0.82 W cm^{-2} at 600 ℃ mainly because of the fabricated thinner electrolyte (6 μm) of SDC and more efficient cathode material of LSCF ($La_{0.6}Sr_{0.4}Co_{0.2}Fe_{0.8}O_3$) [57]. Based on analyses of experimental studies mentioned above, methanol could be thought of as a promising alternative fuel to SOFCs.

1.3.1 Carbon formation mechanism of methanol-fuelled SOFCs

However, commonly used Ni-based anode likely suffers from severe graphitic carbon deposition when carbon-containing fuels, including methanol, are fed, which could rapidly deteriorate the cell performance and even irreversibly destroy the cell structure. One interesting phenomenon related to carbon formation comparison between methanol and methane fuels on Ni-YSZ anodes is worth noting that according to the investigation of coke formation rates on Ni-YSZ anodes after exposure to various carbon-containing fuels at 750 ℃ conducted by Qu et al. [58], feeding methane fuel was the most susceptible condition to cause carbon deposition compared to methanol fuel, while based on observations of thermal imaging and vibrational Raman spectroscopy measurements [59], carbon formation induced by methanol fuel was more significant than that of methane fuel when electrolyte-supported SOFC with the Ni-YSZ anode was operated at 715 ℃ under OCV condition. The possible underlying reason for these two contrasting comparisons might be the difference in carbon formation mechanisms for these two C1 fuels. Different from methane that carbon formation is largely due to methane cracking reaction, deposited carbon in methanol-fuelled SOFCs is primarily generated via the Boudouard reaction from the decomposed carbon monoxide [60]. Boudouard reaction is

thermodynamically favourable at lower temperatures, which indicates that carbon deposition would take place at a relatively lower temperature (below 700 ℃ [45]). Besides, results of equilibrium calculations and experimental tests also showed that the amounts of deposited carbon would increase with the decrease of operating temperature [53,61], which poses a more serious degradation threat to low or intermediate temperature methanol-fed SOFCs. Therefore, at a relatively higher temperature of 750 ℃, the methane cracking reaction could be promoted, leading to a higher coke formation rate in comparison to methanol fuel, while for the relatively lower operating temperature of 715 ℃, the deposited carbon from the Boudouard reaction will be thermodynamically favoured and methane cracking reaction will be limited [45,62], leading to the opposite carbon deposition phenomena for methane and methanol fuels at different operating temperatures. Therefore, various strategies from the perspectives of thermodynamics and kinetics were reported to tackle the coking issue which has been experimentally observed in various research works to improve the durability of methanol-fed SOFCs with Ni-based anodes [48,56,57,60,63,64].

1.3.2 Strategies to suppress the carbon formation for methanol-fuelled SOFCs

The addition of steam to the methanol stream could be a straightforward and effective way to suppress carbon deposition in methanol-fed SOFCs. With the addition of sufficient steam in methanol fuel, the partial pressure of carbon monoxide could be decreased since added water will promote water gas shift reaction to move forward. Besides, water gasification of carbon reaction could also be proceeded to remove the possible generated carbon, thereby preventing carbon formation in anode. It was reported that there was no carbon deposition on Ni-YSZ catalyst at 1000 ℃ when the mixture of methanol and steam with a molar ratio of 1.0/3.0 was supplied [65]. Besides, at least 2 mole steam per mole methanol was needed to guarantee the stable operation of anode-supported SOFC with Ni-YSZ as the anode for more than 120 h under 0.221 A cm^{-2} at 750 ℃ [64]. The discrepancy between these two S/C ratios can be

attributed to the fact that current density could also play a role in carbon mitigation because high concentrations of electrochemical products tend to consume carbon monoxide. In light of equilibrium calculations [53], the minimum fuel utilization for methanol fuel was about 2.1% at 800 ℃ to avoid coking issue, and higher current density or fuel utilization is required for lower temperatures. For example, low fuel utilization of 0.4% estimated by methanol flow rate and current led to a substantial performance decrease from 100 to about 50 mW cm^{-2} at 800 ℃ within 12 hours for the SOFC with Ni-YSZ anode, while for the cell with modified Ni-YSZ anode by ZDC ($Zr_{0.35}Ce_{0.65}O_{2-\delta}$), the improved performance of 240 mW cm^{-2} due to mixed conducting properties of ZDC could be maintained for 12 h at same operating temperature because of enhanced fuel utilization (about 2.2%), though a small amount of carbon was detected by EDX measurement [48]. In addition, adding the coking resistance material doped-CeO_2 could also help to improve carbon tolerance, which was evidenced by less carbon deposition on the modified anode than that of Ni-YSZ anode at OCV condition [48]. Similarly, with high current density condition and SDC as anode ionic phase, long-term operations of consecutive 160 hours at three operating temperatures (550, 600 and 650 ℃) and 60 hours at 600 ℃ for the methanol-fuelled SOFC were achieved at 0.5 V and 0.8 A cm^{-2}, respectively [56,57]. Carbon deposition could also be mitigated by incorporating or alloying other metals to modify the coking tolerance ability as well as the catalytic activity of Ni-based cermet anode. Cu is chemically inert to carbon deposition and was also reported to be the active catalyst to provide the desired fast kinetics for the methanol decomposition process, especially at low temperatures [52]. In addition, Cu shows a higher promotion effect for water gas shift reaction compared to Ni so high production of hydrogen and less carbon monoxide could be achieved through the combination of Ni and Cu [4]. Therefore, with the copper infiltrated Ni-GDC ($Gd_{0.1}Ce_{0.9}O_{1.95}$) anode, both electrochemical performance and durability of methanol-fed SOFC were enhanced significantly at a low temperature of 550 ℃ [60]. The P_{max} of cell in

methanol fuel was increased to 0.42 W cm^{-2} for the infiltrated anode from 0.18 W cm^{-2}, which was mainly due to the improvement of methanol conversion and thus increased yields of direct fuels. Cell with pristine anode experienced immediate degradation after 15 h because of severe filamentous graphitic carbon distinguished by SEM image, while stable performance was maintained for over 50 hours for the modified counterpart when methanol was fed at 550 ℃, which demonstrated higher carbon tolerance capacity of the proposed SOFC [60]. Further, Pd nanoparticles were successfully deposited into the porous Ni scaffold of electrolyte-supported SOFC through the atomic layer deposition (ALD) technique [63]. Both power output and stability against carbon were considerately enhanced with the fabricated heterogeneous Ni-Pd bimetallic anode due to higher kinetics towards chemical/electrochemical reactions and intrinsic high coking resistance of Pd metal. In addition, other coke tolerant materials such as basic oxides (Pr_4O_7 and Pr_6O_{11} [66], NbO_x [67], and La_2O_3 or Sm_2O_3 [68]) and metals (Mo [69], and Co [70]) were reported to add into Ni-SDC ($Ce_{0.8}Sm_{0.2}O_{1.9}$) anode to reasonably improve carbon tolerance of composite SDC-carbonate electrolyte-supported SOFCs.

1.4 Research gaps

The above-mentioned experimental studies demonstrate the feasibility of high-performance direct methanol SOFCs with the state-of-the-art Ni-based anode configuration. However, although the investigations of the methanol-fuelled-SOFC were significantly conducted, less simulation models were established and studied.

Firstly, the present literature is lacking a detailed numerical modelling study on the complicated chemical and physical processes in the SOFC as the chemical reactions, electrochemical reactions, and transport processes are highly coupled. For example, the operating temperature may significantly affect chemical reaction rates, which in turn may influence the gas composition and subsequently affect the fuel cell power output. A

comprehensive understanding of these phenomena is essential to optimize operating conditions and fuel cell micro- and macro-structures for performance enhancement.

Secondly, although the state-of-the-art Ni-based anode is less susceptible to methanol fuel compared to methane due to the presence of the C-O bond in the methanol molecular structure, the coking issue is still an obstacle to the wide application of SOFC fed by methanol fuel. Supplying sufficient steam to methanol stream could be an effective strategy to prevent carbon deposition. However, excess steam could lower the performance of the SOFC system due to the dilution effect. Besides, the durability of methanol-fuelled SOFC could be substantially influenced by the use of steam in the anode. This is because highly coupled fluid flow, chemical/electrochemical reactions and heat/mass transfer processes complicate the temperature field inside the cell, which could induce thermal stress resulting from the temperature gradient and the mismatch of thermal expansion coefficients. Meanwhile, the local low temperature might thermodynamically favour carbon formation in methanol-fuelled SOFC. Therefore, for the stable and efficient operation of methanol fuelled SOFC, a comprehensive understanding of chemical/electrochemical reactions as well as heat and mass transfers is essential for identifying suitable operating conditions.

Thirdly, due to uneven electrochemical reactions and heat transfer of gas convective flows, non-uniform temperature distributions within SOFC assembly or stack were frequently observed, especially for internal reforming SOFCs, which poses a threat to material deterioration and structural integrity. Lots of theoretical and experimental works conducted with a focus on thermal control and management have tried to solve the problems mentioned above, but several challenges have still limited the commercialization of these strategies. Besides, different from the battery, SOFC is an open system that thermally interacts with reacting gases, which indicates that cell thermal state will be considerably influenced by gas conditions, especially for cathode air, but the cooling effectiveness and thermal/electrical

responses of air conditions have not been fully understood yet. Therefore, a validated mathematic model is used to further identify the knowledge of temperature gradient profiles in cell components, especially the ceramic electrolyte, which will be critically essential for operating condition selection, structure design and failure assessment of realistic SOFCs.

1.5 Objectives of PhD research

In general, it is hard to perform in-situ detection of SOFC internal characteristics in experimental tests considering the high operating temperature as well as the small size of fuel cell structure. Fortunately, the numerical method provides an effective and facile way to conduct SOFC investigations, especially for the SOFC operating on hydrocarbon fuel since understanding complex chemical/electrochemical and physical processes is essential for performance optimization and stable operation in terms of thermal stress as well as coking issue. Therefore, the main objectives of my PhD research are as follow:

1. To stablish a numerical model to describe the complicated physical and chemical phenomena inside the cell when methanol is used as fuel for tubular SOFC since subsequent optimizations of operating conditions and micro- and macro-structures is essential to for performance enhancement.

2. To investigate the effects of adding steam to the main methanol fuel, because, although supplying sufficient steam to methanol stream could be an effective strategy to prevent carbon deposition, electrochemical performance and cell durability of methanol-fuelled SOFC could be influenced by the use of steam in the anode.

3. To study the thermal responses of air conditions and find effective strategies to improve the thermal safety of methanol-fuelled SOFC due to non-uniform temperature distribution within SOFC assembly or stack

Based on these objectives, a 2D comprehensive model for direct methanol SOFC is developed and parametric simulations are performed. In chapter 2, the methodology of

computer simulation is introduced. Basic sub-models for each chemical/physical process are summarised. In chapter 3, the model is focused on the complicated processes inside the cell and structure optimization. In chapter 4, the thermal effects of SOFC running on steam/methanol are greatly investigated with the focus on the S/C of fuel mixture. In chapter 5, the effects of air condition on temperature gradient are mainly studied to provide useful guidance for the operating condition selection, structure design and failure assessment. In chapter 6, conclusions and outlook are given to discuss the main results of current research work and future directions of methanol-fulled SOFC modelling, respectively.

Chapter 2: Methodology

Based on the principles of SOFC, five sub-models, including chemical reaction model, electrochemical reaction model, computational fluid dynamics model, mass and heat transfer models, are needed to be considered to describe detailed processes of SOFC in the developed mathematic model. Governing equations for each model will be given in the following section.

2.1 Chemical reaction model

Reaction rates and related heat could be calculated by the chemical reaction model. MDR and WGSR are expected to take place in the anode layer based on assumptions, while these reactions in anode channel could be negligible due to the lack of catalyst [71]. Reaction rates for MDR (R_{MDR}) and reversible WGSR (R_{WGSR}) can be calculated as shown below:

The MDR [72]:

$$R_{MDR} = k_D p^l_{CH_3OH} E_{qD} \tag{2.1}$$

$$E_{qD} = 1 - \frac{p^l_{CO}\left(p^l_{H_2}\right)^2}{K_{eq,D} p^l_{CH_3OH}} \tag{2.2}$$

$$K_{eq,D} = 1.718 \times 10^{14} \exp\left(-\frac{95419}{RT}\right) \tag{2.3}$$

The WGSR [73]:

$$R_{WGSR} = k_{sf}\left(p^l_{H_2O} p^l_{CO} - \frac{p^l_{H_2} p^l_{CO_2}}{K_{ps}}\right) \tag{2.4}$$

$$k_{sf} = 0.0171 \exp\left(-\frac{103191}{RT}\right) \tag{2.5}$$

$$K_{ps} = \exp\left(-0.2935Z^3 + 0.6351Z^2 + 4.1788Z + 0.3169\right) \tag{2.6}$$

$$Z = \frac{1000}{T(K)} - 1 \tag{2.7}$$

where k_D is the tuning parameter used for model validation; R and T denote universal gas constant and temperature, respectively; p^l_i represents the local partial pressure of species i. It should be mentioned that the chemical reaction rates are only influenced by partial pressures

of gas species and the temperature based on above equations, so the conditions that affect gas compositon and working temperature are sure to influence the chemical reaction rates and then SOFC electrochemical performance.

According to thermodynamics, enthalpy changes of formation (ΔH) in the form of heat absorption or generation will be accompanied by the occurrences of chemical reactions. Therefore, chemical heat changes (Q_{che}) associated with MDR and WGSR could be determined by Eq. (2.8), involving the heat consumption by endothermic MDR (ΔH_{MDR}, Eq. (2.9)) and heat generation from exothermic WGSR (ΔH_{WGSR}, Eq. (2.10)),

$$Q_{che} = R_{MDR}\Delta H_{MDR} + R_{WGR}\Delta H_{WGSR} \tag{2.8}$$

$$\Delta H_{MDR} = 2h_{H_2} + h_{CO} - h_{CH_3OH} \tag{2.9}$$

$$\Delta H_{WGSR} = h_{CO_2} + h_{H_2} - h_{CO} - h_{H_2O} \tag{2.10}$$

where h_i is the enthalpy of formation of species i, which can be calculated by the definition of enthalpy (Eq. (2.11)).

$$h(T) = h(T_0) + \int_{T_0}^{T} C_p(T)\, dT \tag{2.11}$$

2.2 Electrochemical reaction model

Electricity power and irreversible heat produced from electrochemical oxidation and reduction reactions could be described by the electrochemical reaction model. In electrochemistry, the general Butler-Volmer (BV) equation is used to link the current density with activation overpotential (η_{act}). In the present study, hydrogen and carbon monoxide participate in electrochemical reactions as fuels. Therefore, current density (i) produced from Eqs. (1.1), (1.2) and (1.3) could be determined by:

$$i = i_0 \left\{ \exp\left(\frac{\alpha n F \eta_{act}}{RT}\right) - \exp\left(\frac{-(1-\alpha) n F \eta_{act}}{RT}\right) \right\} \tag{2.12}$$

where i_0 is exchange current density. In the previous experimental research, the rate of CO electrochemical oxidation is about 0.32-0.52 times that of H_2 electrochemical oxidation rate.

Thus, exchange current densities for H_2, CO and O_2 are set to be 5300 A m^{-2}, 3000 A m^{-2} and 2000 A m^{-2}, respectively. More detailed information can be found in ref. [74]. *n*, α and *F* are the number of electrons generated from a single electrochemical reaction, charge transfer coefficient, and Faraday constant, respectively. The operating potential (*V*) can be given by the subtraction of activation and ohmic overpotential losses from thermodynamic equilibrium potential (*E*, Nernst potential):

$$V = E - \eta_{act,a} - \eta_{act,c} - \eta_{ohmic} \tag{2.13}$$

here, η_{ohmic} signifies the overpotential related to ion and electron transports; *E* of the cell is actually an average of E_{H_2} and E_{co} [71] whose calculations use local partial pressures of relevant species, so concentration overpotentials have already been implicitly included in Eqs. (2.14) and (2.15) [75,76]. Besides, anode activation overpotentials for each direct fuel could be easily derived from Eq. (2.13).

$$E_{H_2} = E_{H_2}^T + \frac{RT}{2F}\left[\frac{p_{H_2}^l \left(p_{O_2}^l\right)^{0.5}}{p_{H_2O}^l}\right] \tag{2.14}$$

$$E_{CO} = E_{CO}^T + \frac{RT}{2F}\left[\frac{p_{CO}^l \left(p_{O_2}^l\right)^{0.5}}{p_{CO_2}^l}\right] \tag{2.15}$$

$$E_{H_2}^T = 1.253 - 0.00024516T \tag{2.16}$$

$$E_{CO}^T = 1.46713 - 0.0004527T \tag{2.17}$$

Besides, Ohm's law is used to describe ohmic potential losses (η_{ohmic}):

$$i_l = -\sigma_l^{eff} \nabla(\emptyset_l) \tag{2.18}$$

$$i_s = -\sigma_s^{eff} \nabla(\emptyset_s) \tag{2.19}$$

where $\emptyset_l$ and $\emptyset_s$ represent ionic and electronic phase potentials, respectively; σ_l^{eff} and σ_s^{eff} denote the effective conductivities of ion and electron in electrodes, which can be determined by material intrinsic conductivities and the volume fractions of ionic (V_l) and electronic (V_s)

phases in electrodes as well as the tortuosity (τ) of porous structures [77], as calculated by Eqs. (2.20) and (2.21).

$$\sigma_l^{eff} = \sigma_l \cdot \frac{V_l}{\tau_l} \tag{2.20}$$

$$\sigma_s^{eff} = \sigma_s \cdot \frac{V_s}{\tau_s} \tag{2.21}$$

The heat will be released during electrochemical processes since from the perspective of thermodynamics, the maximum electrical energy available in the fuel is Gibbs free energy (ΔG) [10]. Therefore, based on the second law of thermodynamics (Eq. (2.22)), the heat (Q_{ele}) related to electrochemical reactions can be written as:

$$T\Delta S = \Delta H - \Delta G \tag{2.22}$$

$$Q_{ele} = \frac{i_{H_2} T\Delta S_{H_2}}{2F} + \frac{i_{CO} T\Delta S_{CO}}{2F} \tag{2.23}$$

here, $T\Delta S$ represents irreversible energy loss of electrochemical reactions, and ΔS is the entropy change of hydrogen or carbon monoxide electrochemical reactions, which can be determined by [71]:

$$\Delta S_{H_2} = s_{H_2O} - 0.5 s_{O_2} - s_{H_2} \tag{2.24}$$

$$\Delta S_{CO} = s_{CO_2} - 0.5 s_{O_2} - s_{CO} \tag{2.25}$$

where, s_i is the entropy of species i, which can be calculated by the definition of entropy (Eq. (2.26)).

$$s(T) = S(T_0) + \int_{T_0}^{T} \frac{C_p(T)}{T} dT \tag{2.26}$$

2.3 Computational fluid dynamics model

The CFD model is used to simulate the gas flow in both channels and porous electrodes. The continuity equation (Eq. (2.27)) and classic NS (Navier-Stokes) equation (Eq. (2.28)) at steady state are applied in fuel and gas channels [71].

Mass conservation:

$$\rho \nabla \cdot U = 0 \tag{2.27}$$

Momentum conservation:

$$\rho(U \cdot \nabla) \cdot U = -\nabla p + \nabla \cdot [\mu(\nabla U + \nabla U^T)] \tag{2.28}$$

Owing to mass exchange between anode and cathode because of the anion transfer, a source term is included in the continuity equation to account for the mass transfer (Eq. (2.29)). The Brinkman equations, the modified NS equations with Darcy's term, are utilized to describe the momentum conservation in the porous electrodes (Eq. (2.30)) [78]:

Mass conservation:

$$\rho \nabla \cdot U = Q_m \tag{2.29}$$

Momentum conservation:

$$\frac{1}{\varepsilon}\rho(U \cdot \nabla) \cdot U\frac{1}{\varepsilon} = -\nabla p + \nabla \cdot \left[\mu\frac{1}{\varepsilon}(\nabla U + \nabla U^T) - \frac{2}{3}\mu\frac{1}{\varepsilon}(\nabla \cdot U)\right] - \left(\mu\kappa^{-1} + \frac{Q_m}{\varepsilon^2}\right)U \tag{2.30}$$

where κ and ε are the permeability and porosity of porous media, respectively; p and U are the pressure and mass average velocity of gas mixture, respectively; source term Q_m denotes the oxygen transferred from cathode to the anode; μ represents the dynamic viscosity of gas mixture and can be written as:

$$\mu = \sum_{i=1}^{n} \frac{y_i \mu_i}{\sum_{j=1}^{n}(y_i\sqrt{\frac{M_j}{M_i}})} \tag{2.31}$$

where M_i and y_i are the molecular weight and molar fraction of species i, respectively, and dynamic viscosity for each gas (μ_i) can be found in Table 2.1.

Table 2.1 Dynamic viscosity of gas species.

μ_i	Value	Unit
CO	$(23.811 + 0.53944 \times T - 1.5411 \times 10^{-4} \times T^2) \times 10^{-7}$	Pa s
CO_2	$(11.811 + 0.49838 \times T - 1.0851 \times 10^{-4} \times T^2) \times 10^{-7}$	Pa s
H_2	$(27.758 + 0.212 \times T - 3.28 \times 10^{-5} \times T^2) \times 10^{-7}$	Pa s
H_2O	$(-36.826 + 0.429 \times T - 1.62 \times 10^{-5} \times T^2) \times 10^{-7}$	Pa s
CH_3OH	$(-14.236 + 0.38935 \times T - 6.2762 \times 10^{-5} \times T^2) \times 10^{-7}$	Pa s
O_2	$(44.224 + 0.562 \times T - 1.13 \times 10^{-4} \times T^2) \times 10^{-7}$	Pa s
N_2	$(42.606 + 0.475 \times T - 9.88 \times 10^{-5} \times T^2) \times 10^{-7}$	Pa s

2.4 Mass transfer model

Mass transfer model is employed to calculate the concentration of each uncharged gaseous species in SOFC due to various complicated processes, involving mixing, convection, diffusion etc. Therefore, the molar conservation equations of species *i* at steady state are shown below:

In channels:

$$\nabla \cdot J_i + c(u \cdot \nabla) y_i = 0 \tag{2.32}$$

In electrodes:

$$\nabla \cdot J_i + c(u \cdot \nabla) y_i = R_i \tag{2.33}$$

where c is gas mixture concentration; J_i represents the molar diffusion flux of species i;, and R_i is the mole change rate of species i as a result of electrochemical/chemical processes; u denotes the molar average velocity of gas mixture.

Diffusion flux of species i in Eqs. (2.32) and (2.33) is calculated by the Stefan-Maxwell approach [79]. The molecular diffusion or continuum diffusion plays a major role in fuel or air channels [80], while in porous electrodes, both molecular diffusion and Knudsen diffusion need to be considered [81]. Therefore, steady-state diffusion models are described by:

In channels:

$$\sum_{j=1, j\neq i}^{n} \frac{y_j N_i - y_i N_j}{D_{ij}} = -c \frac{dy_i}{dx} \tag{2.34}$$

In electrodes:

$$\sum_{j=1, j\neq i}^{n} \frac{y_j N_i - y_i N_j}{D_{ij}^{eff}} = -c \frac{dy_i}{dx} \tag{2.35}$$

here N_i denotes the molar flux of species i; D_{ij} is the binary diffusion coefficient of species i and j, which can be given by Fuller et al. expression (Eq. (2.36)) [82]; D_{ij}^{eff} is the effective binary diffusion coefficient of species i and j considering molecular diffusion and Knudsen diffusion with the correction of microstructures of porous electrodes (Eq. (2.37)) [83],

$$D_{ij} = \frac{0.00143T^{1.75}}{2p\left(v_i^{1/3}+v_j^{1/3}\right)^2}\left(\frac{1}{M_i}+\frac{1}{M_j}\right)^{1/2} \tag{2.36}$$

$$D_{ij}^{eff} = \frac{\varepsilon}{\tau}\left(\frac{1}{D_{ij}}+\frac{1}{D_{ik}}\right)^{-1} \tag{2.37}$$

here v_i represents special molecule diffusion volume, which can be found in Table 2.2.

Knudsen diffusion coefficient (D_{ik}) can be calculated based on the kinetic theory [84], as expressed below:

$$D_{ik} = \frac{2}{3}r\sqrt{\frac{8RT}{\pi M_i}} \tag{2.38}$$

where r represents the mean pore radius of the electrode.

Table 2.2 Special molecule diffusion volume of each species [85].

v_i	Value	Unit
CO	18.0	cm^3
CO_2	26.7	cm^3
H_2	6.12	cm^3
H_2O	13.1	cm^3
CH_3OH	31.25	cm^3
O_2	16.3	cm^3
N_2	18.5	cm^3

2.5 Heat transfer model

A heat transfer model is developed to simulate the temperature field in the whole computational domain. Heat transfer processes inside the SOFC are complicated, including the heat generation from electrochemical reactions, irreversible overpotential loss, and exothermic WGSR, as well as the heat consumption by endothermic MDR, leading to the nonuniform temperature distribution. Therefore, general energy conservation equations are applied:

In channels:

$$\rho C_p u \cdot \nabla T + \nabla \cdot \left(-\lambda_g \nabla T\right) = 0 \tag{2.39}$$

In electrodes or electrolyte:

$$\rho C_p u \cdot \nabla T + \nabla \cdot \left(-\lambda_{eff} \nabla T\right) = Q_e \tag{2.40}$$

$$\lambda_g = \sum_{i=1}^{n} y_i \lambda_i \tag{2.41}$$

$$C_p = \sum_{i=1}^{n} y_i C_{p,i} \tag{2.42}$$

$$\lambda_{eff} = (1-\varepsilon)\lambda_{sol} + \varepsilon\lambda_g \tag{2.43}$$

where λ_{sol} represents the thermal conductivity of solid structure; thermal conductivity (λ_g) and heat capacity (C_p) of gas mixture can be estimated by mole fraction averaging (Eqs. (2.21) and (2.42) [82,86]; effective thermal conductivity (λ_{eff}) is determined by the volume fractions of solid phase and gas phase (Eq. (2.43)). Thermodynamic properties of gas species and solid structure materials can be found in Table 2.3 and Table 2.4, respectively.

Q_e (W m^{-3}) is the source term accounting for heat generation consumption in SOFC. Source terms to be applied to anode, electrolyte, and cathode are calculated by Eqs. (2.44), (2.45) and (2.46), respectively,

In anode:

$$Q_e = Q_r + Q_{ele} + i_{H_2}\eta_{act,H_2} + i_{CO}\eta_{act,CO} + \left(\frac{i_l^2}{\sigma_l^{eff}} + \frac{i_s^2}{\sigma_s^{eff}}\right) \tag{2.44}$$

In electrolyte:

$$Q_e = \frac{i_l^2}{\sigma_l^{eff}} \tag{2.45}$$

In cathode

$$Q_e = \left(i_{H_2} + i_{CO}\right)\eta_{act,O_2} + \left(\frac{i_l^2}{\sigma_l^{eff}} + \frac{i_s^2}{\sigma_s^{eff}}\right) \tag{2.46}$$

here $i_{H_2}\eta_{act,H_2}$ and $i_{CO}\eta_{act,CO}$ are the heat generations related to activation overpotentials of H_2 and CO electrochemical oxidations, respectively, which are applied based on the distributions of η_{act,H_2} and $\eta_{act,CO}$in electrodes; $\frac{i_s^2}{\sigma_s^{eff}}$ or $\frac{i_l^2}{\sigma_l^{eff}}$ represents the ohmic heat due to the electron or ion resistance, which will be applied to corresponding components.

Table 2.3 Thermodynamic properties of gas species [85].

Gas species	Value	Unit

λ_i		
CO	$0.00158 + 8.2511 \times 10^{-5} \times T - 1.9081 \times 10^{-8} \times T^2$	W m^{-1} K^{-1}
CO_2	$-0.012 + 1.0208 \times 10^{-4} \times T - 2.2403 \times 10^{-8} \times T^2$	W m^{-1} K^{-1}
H_2	$0.03591 + 4.5918 \times 10^{-4} \times T - 6.4933 \times 10^{-8} \times T^2$	W m^{-1} K^{-1}
H_2O	$0.00053 + 4.7093 \times 10^{-5} \times T + 4.9551 \times 10^{-8} \times T^2$	W m^{-1} K^{-1}
CH_3OH	$-0.007797 + 4.167 \times 10^{-5} \times T + 1.217 \times 10^{-7} \times T^2$	W m^{-1} K^{-1}
O_2	$0.00121 + 8.6157 \times 10^{-5} \times T - 1.3346 \times 10^{-8} \times T^2$	W m^{-1} K^{-1}
N_2	$0.00309 + 7.593 \times 10^{-5} \times T - 1.1014 \times 10^{-8} \times T^2$	W m^{-1} K^{-1}
$C_{p,i}$		
CO	$29.556 - 6.5807 \times 10^{-3} \times T + 2.013 \times 10^{-5} \times T^2 - 1.2227 \times 10^{-8} \times T^3 + 2.2617 \times 10^{-12} \times T^4$	J mol^{-1} K^{-1}
CO_2	$27.437 + 4.2315 \times 10^{-2} \times T - 1.9555 \times 10^{-5} \times T^2 + 3.9968 \times 10^{-9} \times T^3 - 2.9872 \times 10^{-13} \times T^4$	J mol^{-1} K^{-1}
H_2	$25.399 + 2.1078 \times 10^{-2} \times T - 3.8549 \times 10^{-5} \times T^2 + 3.188 \times 10^{-8} \times T^3 + 8.7585 \times 10^{-12} \times T^4$	J mol^{-1} K^{-1}
H_2O	$33.933 - 8.4186 \times 10^{-3} \times T + 2.9906 \times 10^{-5} \times T^2 - 1.7825 \times 10^{-8} \times T^3 + 3.6934 \times 10^{-12} \times T^4$	J mol^{-1} K^{-1}
CH_3OH	$40.046 - 3.8287 \times 10^{-2} \times T + 2.4529 \times 10^{-4} \times T^2 - 2.1679 \times 10^{-7} \times T^3 + 5.9909 \times 10^{-11} \times T^4$	J mol^{-1} K^{-1}
O_2	$29.526 - 8.8999 \times 10^{-3} \times T + 3.8083 \times 10^{-5} \times T^2 - 3.2629 \times 10^{-8} \times T^3 + 8.8607 \times 10^{-12} \times T^4$	J mol^{-1} K^{-1}
N_2	$29.342 - 3.5395 \times 10^{-3} \times T + 1.0076 \times 10^{-5} \times T^2 - 4.3116 \times 10^{-9} \times T^3 + 2.5935 \times 10^{-13} \times T^4$	J mol^{-1} K^{-1}

Table 2.4 Thermodynamic property of materials [87,88].

Material	C_p, J mol^{-1} K^{-1}	λ, W m^{-1} K^{-1}	ρ, kg m^{-3}
Ni/YSZ	390	6.23	6870
YSZ	525	2.57	6086
YSZ/LSM	398	3.47	3814.8

Chapter 3: Modelling of the high-performance direct methanol solid oxide fuel cells

3.1 Introduction

Due to the limitations of hydrogen, direct use of methanol fuel in SOFC is promising considering its high electrochemical performance as well as the easy transportation of methanol fuel. However, the present literature is lacking a detailed numerical modelling study on complicated chemical and physical processes in SOFC when methanol is feeding, and a comprehensive understanding of these phenomena is essential for performance enhancement by optimizing operating conditions as well as micro- and macro-structures.

In this chapter, the 2D mathematic model fully considers chemical reactions (methanol reforming reaction and water gas shift reaction), electrochemical reactions and mass transfer in a tubular SOFC running on CH_3OH fuel. The typical SOFC configuration of Ni/YSZ-YSZ-YSZ/LSM is used. The modelling results are compared with experimental results from Jiang et al. [55] for model validation. Detailed parametric simulations are conducted to investigate the effects of operating conditions (inlet temperature and operating potential) and structural parameters (cell length and anode thickness) on the performance of CH_3OH fuelled SOFC.

3.2 Model development

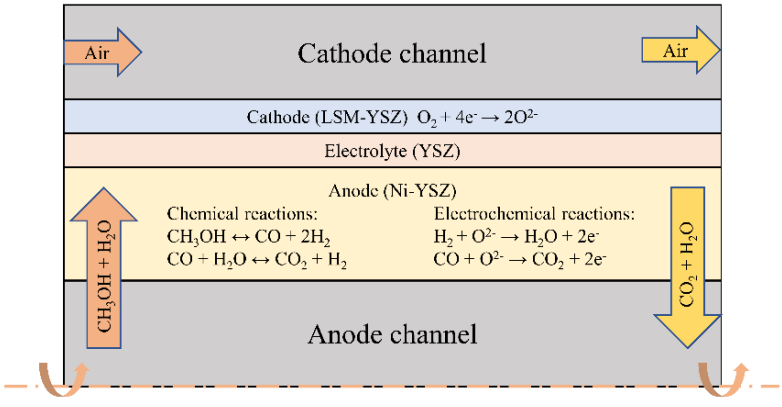

Figure 3.1 Schematic of anode-supported SOFC operating on pure methanol.

In this section, a numerical model is developed for methanol-fuelled SOFC. The schematic of the anode-supported SOFC and the working mechanism are shown in Figure 3.1. According to the experimental set-up from Jiang et al.'s study [55], the computational domain of SOFC includes anode channel (fuel channel), Ni/YSZ porous anode, YSZ dense electrolyte, YSZ/LSM porous cathode, and cathode channel (air channel). In addition to gas transport through porous electrodes, chemical reactions also take place in the porous anode. The dense electrolyte is a gas-tight, oxygen-ion conducting layer which separates the gases of cathode and anode. It is worth noting that the tubular geometry consistent with the experiment set-up is used for the developed SOFC. Considering the axisymmetriy of the structure and limited computer calculation resource, simplified 2D mathematic model is used for simulation works. The physical properties of materials and specific dimensions of SOFC are summarized in Table 3.1. Since some parameters are not specified in the experimental work, they are chosen from several available studies for model validation.

Table 3.1 Model parameters [55,74,89,90].

Parameter	Expression or value	Unit
Bulk electronic conductivity		
Ni	$3.27 \times 10^6 - 1065.3 \times T$	S m^{-1}
LSM	$4.2 \times 10^7/T \times e^{\frac{-1150}{T}}$	S m^{-1}
Bulk ionic conductivity		
YSZ	$3.34 \times 10^4 \times e^{\frac{-10300}{T}}$	S m^{-1}
Porosity		
Cathode	0.46	
Anode	0.46	
Permeability		
Cathode	1.76×10^{-11}	m^2
Anode	1.76×10^{-11}	m^2
S_{TPB}		
Cathode	3.33×10^5	m^2 m^{-3}
Anode	2.66×10^5	m^2 m^{-3}
Thickness		
Anode channel	2	mm
Anode	0.6	mm
Electrolyte	0.01	mm
Cathode	0.1	mm
Cathode channel	2	mm

Cell length	9	mm
Tortuosity of porous electrode	3	

In operation, CH_3OH and air are supplied to the anode channel and cathode channel, respectively. CH_3OH is diffused from anode channel into a porous anode where with the Ni metal catalyst, CH_3OH fuel is converted to CO and H_2 through methanol decomposition reaction (MDR, Eq. (3.1)). Due to the generation of steam from hydrogen electrochemical oxidation, water gas shift reaction (WGSR, Eq. (3.2)) will take place to produce CO_2 and more H_2 in the anode catalyst layer.

$$CH_3OH \leftrightarrow CO + 2H_2 \tag{3.1}$$

$$CO + H_2O \leftrightarrow CO_2 + H_2 \tag{3.2}$$

At the triple phase boundary of the porous anode, both H_2 and CO can be electrochemically oxidized by O^{2-} to produce H_2O and CO_2, generating electrons. The electrons are subsequently collected by the current collector and transported via an external circuit to the cathode, where electrons react with O_2 molecules to form O^{2-}, followed by O^{2-} transport from cathode to anode via the dense electrolyte. Therefore, as long as the fuel and air are supplied to the anode and cathode, the electrical power can be generated continuously.

In this model, only MDR and WGSR are considered to be the possible chemical reactions in the porous anode. The methanation reaction ($CO + 3H_2 \leftrightarrow CH_4 + H_2O$) requires high pressure and a relatively low temperature, which is not favoured under the fuel cell operation condition [65]. Although the Boudouard reaction is also thermodynamically unfavoured in SOFC because of its exothermic nature, it should be noticed that carbon may deposit on the anode catalyst surface due to the fast kinetics of the Boudouard reaction caused by the high temperature in the cell, and carbon deposition could be detrimental to the performance of SOFCs by blocking pores, covering TPB, and even destroying the anode structure (under extreme conditions) [91]. Boudouard reaction is assumed to be negligible in the present work as the O atom in CH_3OH does not favour the formation of C, in comparison with CH_4 fuel.

This assumption is also consistent with experimental results without any noticeable carbon deposition in their stability tests [54–56,61]. However, it should be noted that other chemical reactions may become significant under certain conditions. For example, carbon deposition may happen under certain temperatures and current densities. They can be considered in subsequent studies when more reliable data are available.

Based on the principles of SOFC running on pure methanol fuel, the main assumptions used in simulations are presented below.

(1) Only H_2 and CO can be electrochemically oxidized due to their relatively high reaction kinetics.

(2) The catalyst sites for electrochemical oxidations of H_2/CO and electrochemical reduction of O_2 are uniformly distributed in porous anode and cathode, respectively.

(3) In addition, the electron conduction in electrodes and oxygen ion (O^{2-}) transport in anode-electrolyte-cathode are assumed to be homogeneous and continuous.

(4) All gases are treated as ideal gases, which obey the ideal gas law ($PV = nRT$), and the dynamic viscosity of ideal gas species is independent of the pressure.

(5) The temperature distribution is considered to be uniform within the whole cell due to the small cell size, and all parameters are calculated at a given constant temperature.

(6) The fluid flow in SOFC is considered the laminar flow due to the relatively low Reynolds number.

3.3 Numerical methods and validation

The governing equations of the model are solved by the Finite Element Method using commercial software COMSOL 5.4. The computation domain is discretized into 52,000 elements to ensure the grid independence of results. The preliminary simulation results are compared with experimental data with good agreement as shown in Figure 3.2, and the average error between simulation and experimental data at 1073 K is 6.05%, which validates the present

model. The operating conditions and tuning parameter for the validation are summarized in Table 3.2. Same parameters (except typical operating conditions and structural dimensions) are used for the subsequent parametric simulations.

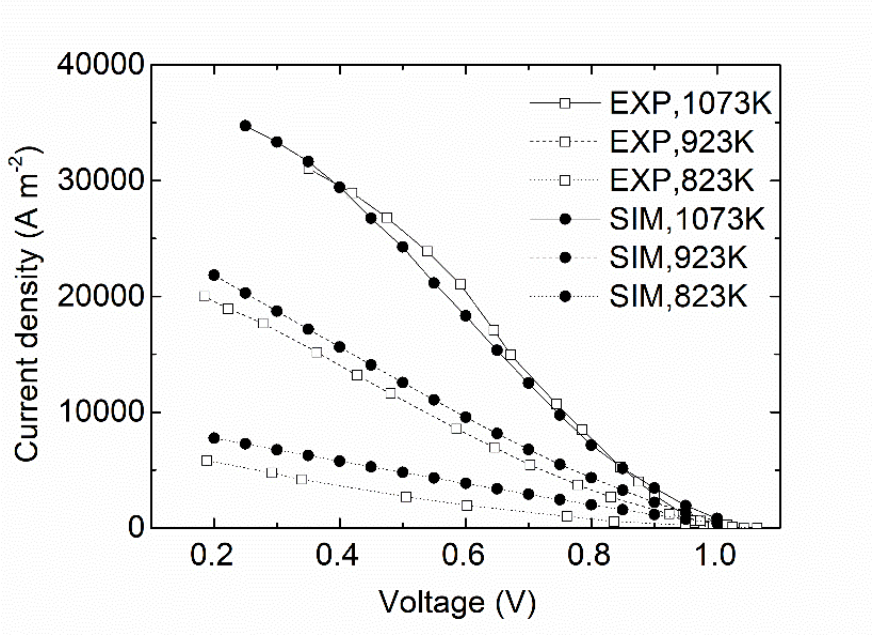

Figure 3.2 Model validation for the methanol-fuelled SOFC at 1073 K, 923 K and 823 K.

Table 3.2 Operation parameters for model validation.

Parameters	Value	Unit
Anode inlet fuel flow rate (liquid)	0.2	ml min^{-1} (std)
Cathode inlet gas flow rate/velocity	600/1.13(1073 K)	SCCM/m s^{-1}
Anode inlet gas composition	CH_3OH (100%)	
Cathode inlet gas composition	O_2 (21%) + N_2 (79%)	
Operating temperature	1073, 923, 873	K
Operating pressure	1	atm
Operating potential	0.2 - 1.0	V
H_2 exchange current density	5300	A m^{-2}
CO exchange current density	3000	A m^{-2}
O_2 exchange current density	2000	A m^{-2}
Equilibrium constant of methanol decomposition reaction, k_D	0.004	

3.4 Results and discussions

3.4.1 Base case

Figure 3.3 shows the distributions of chemical reaction rates and the molar fractions of species at an inlet temperature of 1073 K, and operating potential of 0.6 V. It is found that the

MDR rate is the highest (405 mol m^{-3} s^{-1}) at the inlet near the gas channel and decreases significantly along the anode layer (Figure 3.3a), which is mainly caused by the low concentration of CH_3OH in the anode downstream (Figure 3.3b). Because of the high MDR rate, the molar fraction of CH_3OH decreases considerably along the gas channel. Besides, the distribution of the WGSR rate is different from that of MDR. For WGSR, the rate is highest (15.2 mol m^{-3} s^{-1}) at the outlet near the electrolyte and increases along the anode (Figure 3.3c), which is because of the high concentration of the reactant (H_2O) near the interface of the electrolyte and anode in downstream (Figure 3.3d). The high molar fraction of water near the outlet in the porous anode is mainly due to the gas transport and electrochemical reaction: fast electrochemical reaction at TPB consuming more H_2 and producing more H_2O, and slow diffusion leading to the accumulation of H_2O in the anode layer, thus causing huge concentration gradient between the gas channel and porous anode.

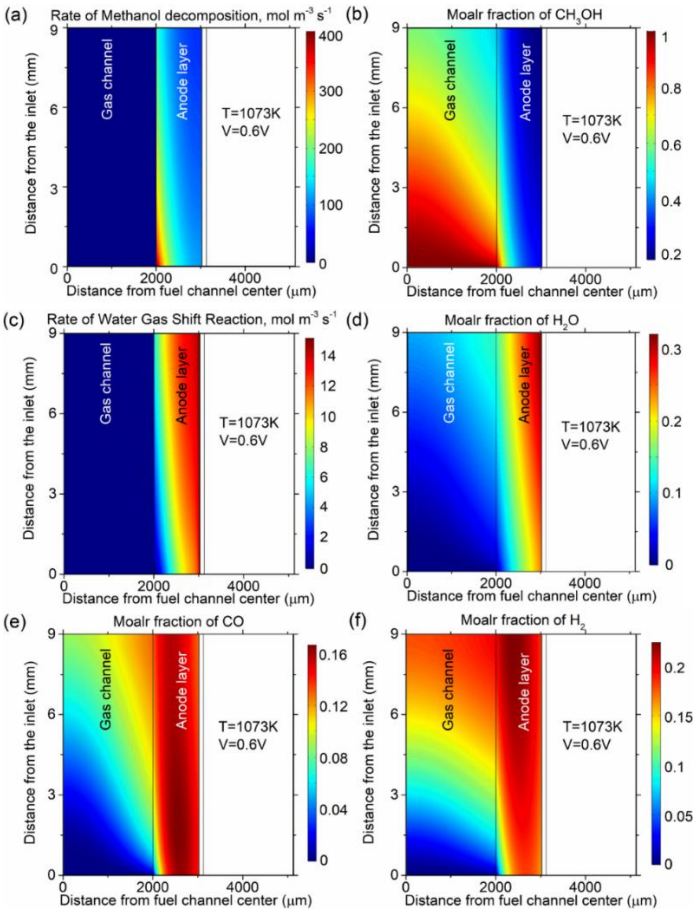

Figure 3.3 Reaction rate distributions and species molar fractions at 1073 K, 0.6 V: (a) MDR;

(b) CH_3OH; (c) WGSR; (d) H_2O; (e) CO; (f) H_2.

It can be observed that a high molar fraction of CO near the inlet (Figure 3.3e) is mainly due to the locally high rate of MDR (producing more CO) and low rate of WGSR (consuming less CO), as shown in Figure 3.3a and Figure 3.3c. Besides, molar fraction of CO exhibits a small increase initially and then a gradual decline (Figure 3.4). This is because of combined effects of continuous decreased CO generation rate and increased CO consumption rate, showing highest CO concentration near the fuel inlet (Figure 3.3e). For comparison, the molar fraction of H_2 shows an opposite trend and H_2 almost accumulates near the outlet (Figure 3.3f), which is due to the locally high rate of WGSR (producing more H_2), as evidenced by the species fraction distribution in Figure 3.4.

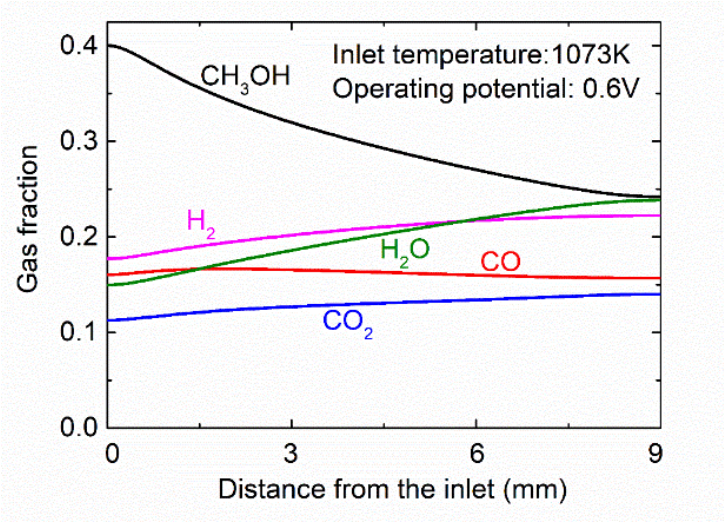

Figure 3.4 Gas composition at the center of porous anode at 1073 K, 0.6 V.

3.4.2 The effect of temperature

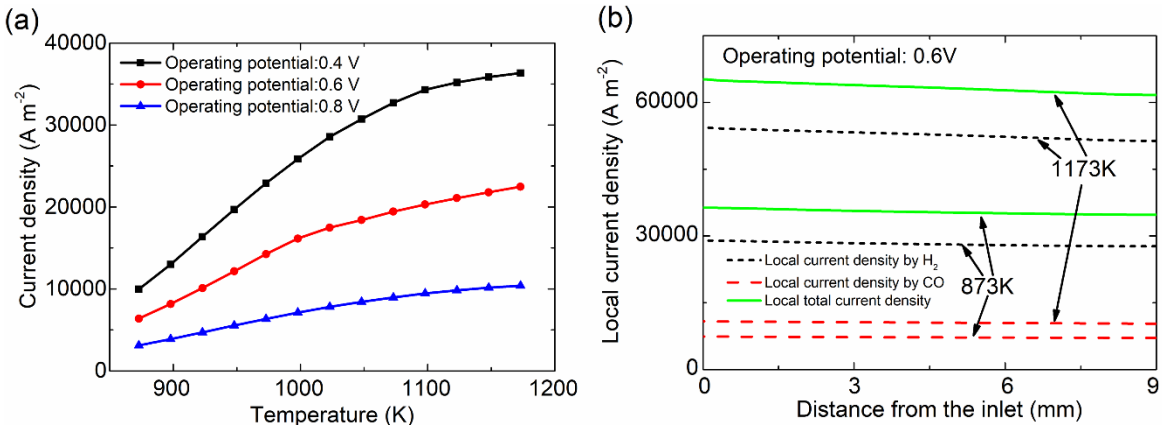

Figure 3.5 (a) The effect of temperature on the output current density at different operating potentials; (b) The current source distribution at the anode-electrolyte interface.

It is known that inlet temperature has a great positive effect on both chemical reactions (MDR and WGSR) and electrochemical oxidations of fuels (CO and H_2). Simulations are conducted to explore the power output of SOFC with the increase of temperatures from 873 K to 1173 K. The output current density of SOFC fuelled by pure methanol is shown in Figure 3.5a. As expected, the current densities are increased considerably with the increase in operating temperature. This phenomenon is mainly caused by the high rate of methanol decomposition reaction (generating more CO and H_2) and fast water gas shift reaction kinetics (producing more H_2) at a high operating temperature. Besides, a high temperature can also benefit the ionic conduction in electrolyte significantly and the rates of electrochemical reactions (generating more electrons per unit time), which can be proved by the current sources of SOFC at the anode-electrolyte interface (Figure 3.5b).

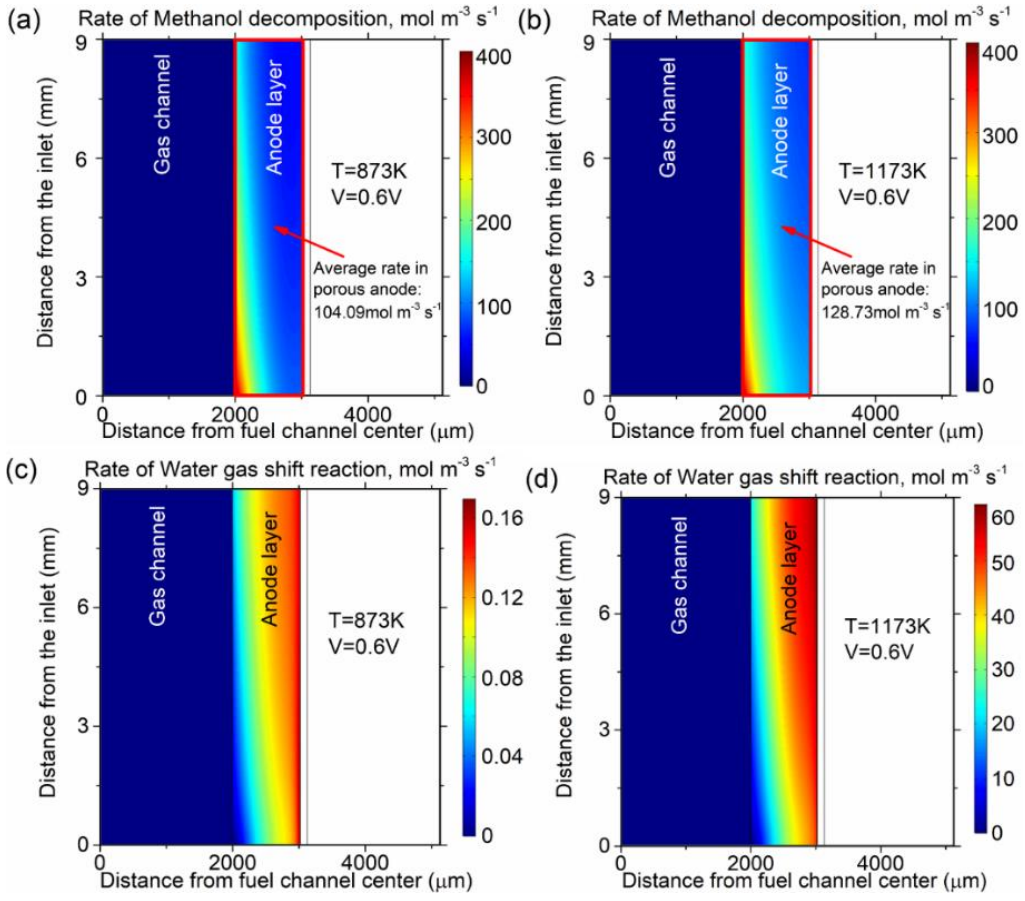

Figure 3.6 Reaction rate distributions at different temperatures: (a) MDR at 873 K; (b) MDR at 1173 K; (c) WGSR at 873 K; (d) WGSR at 1173 K.

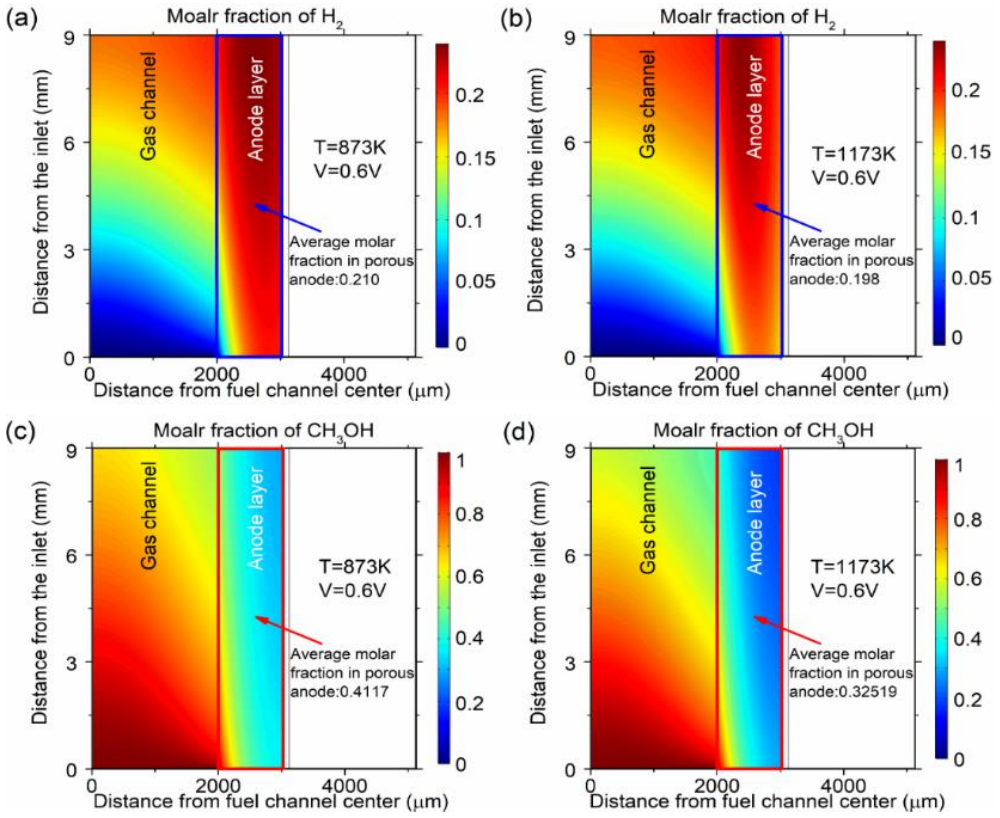

Figure 3.7 Species molar fractions at different temperatures: (a) H_2 at 873 K; (b) H_2 at 1173 K; (a) CH_3OH at 873 K; (b) CH_3OH at 1173 K.

In addition, the rates of MDR and WGSR are all increased with the increase in temperature. Although the peak rates for MDR remain the same for both two temperatures, the average rate of MDR in the porous anode is increased from about 104 mol m^{-3} s^{-1} at 873 K to approximate 129 mol m^{-3} s^{-1} at 1173 K (Figure 3.6a and b). Moreover, for WGSR, the rate is increased considerably as temperature rises (Figure 3.6c and d), and the peak rate at 1173 K (60.4 mol m^{-3} s^{-1}) is much higher than that at 873 K (0.17 mol m^{-3} s^{-1}). The higher rates of MDR and WGSR at 1173 K tend to consume more CH_3OH and produce more H_2 and CO, which will increase the Nernst potentials caused by H_2 and CO fuels. Besides, high temperature is likely to lower the ohmic overpotential loss because oxygen ion conductivity is sensitive to the temperature [92]. Therefore, a high output current density can be obtained at a high temperature

thanks to the temperature effects on the Nernst potentials and the ohmic overpotential losses. Increased chemical reactions (MDR and WGSR) produce more hydrogen. On the other hand, high output current density consumes more hydrogen. As a result, these combined effects cause a slightly lower average molar fraction of hydrogen at 1173 K than that at 873 K (Figure 3.7a and b). However, more methanol is consumed, causing a larger drop in the average CH_3OH molar fraction in the anode when the temperature is increased to 1173 K (Figure 3.7c and d).

3.4.3 The effect of operating potential

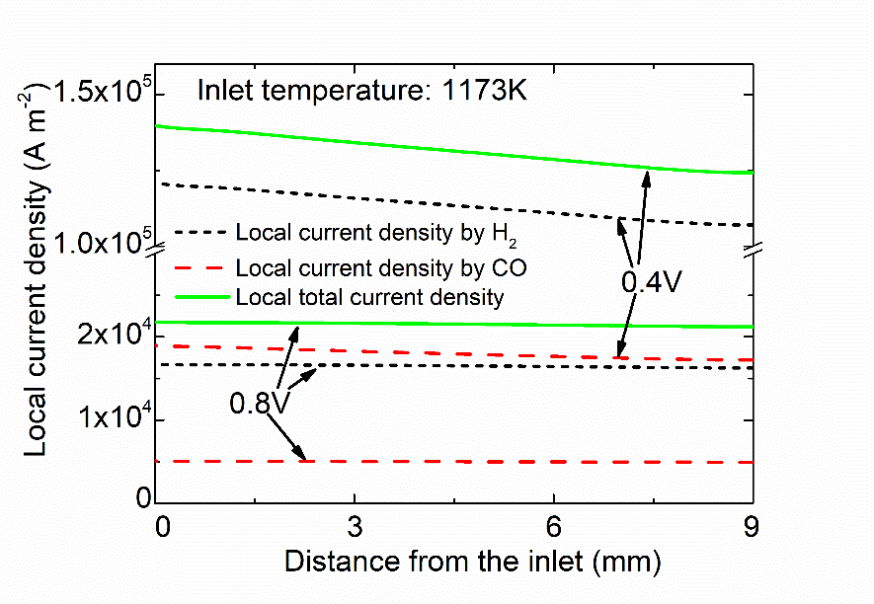

Figure 3.8 The current source distributions at the anode-electrolyte interface.

Simulations are conducted at typical operating potentials (0.4 V, 0.6 V and 0.8 V) since the performance of an SOFC can be profoundly influenced by operating potential. Output current densities are presented in Figure 3.5a. As expected, the output current density is increased significantly with the decrease of operating potential, especially at high temperatures. In addition, current sources by both H_2 and CO fuels are highly enhanced at a low voltage, and so does the total current source (Figure 3.8). Highly increased consumptions of H_2 and CO fuels by electrochemical reactions lead to more generations of water and carbon dioxide at low operating potential, which can be proved by the differences in molar fractions of water and

carbon dioxide at different operating potentials. The peak molar fractions for CO_2 and H_2O are increased considerably from 0.0504 to 0.265 and from 0.116 to 0.498, respectively (Figure 3.9).

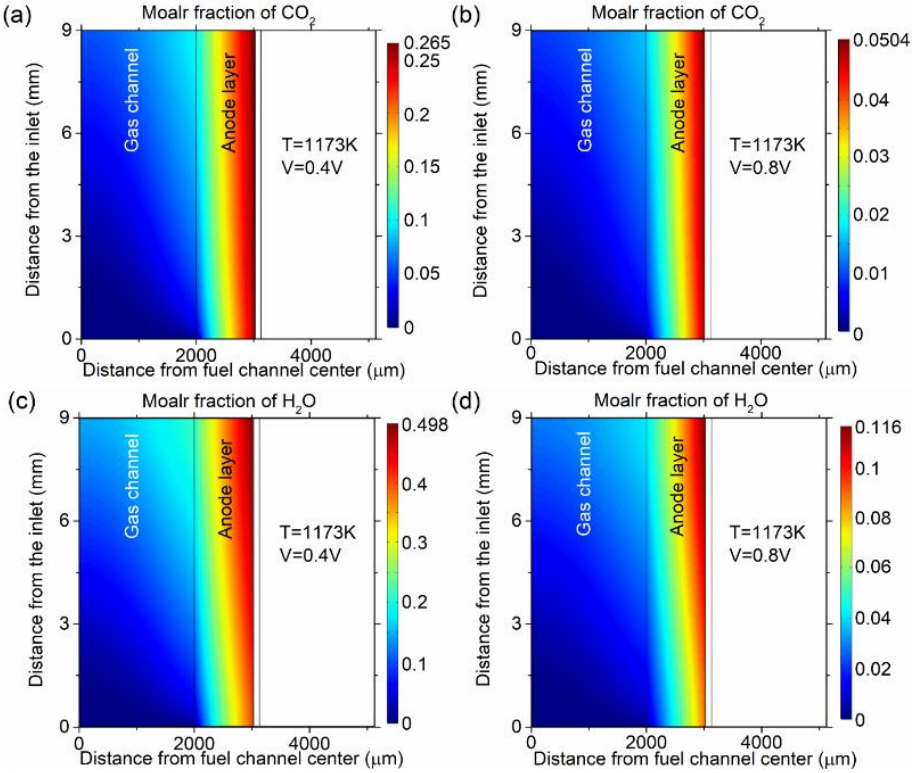

Figure 3.9 Molar fractions of CO_2 at: (a) 0.4 V; (b) 0.8 V; molar fractions of H_2O at: (c) 0.4 V; (d) 0.8 V.

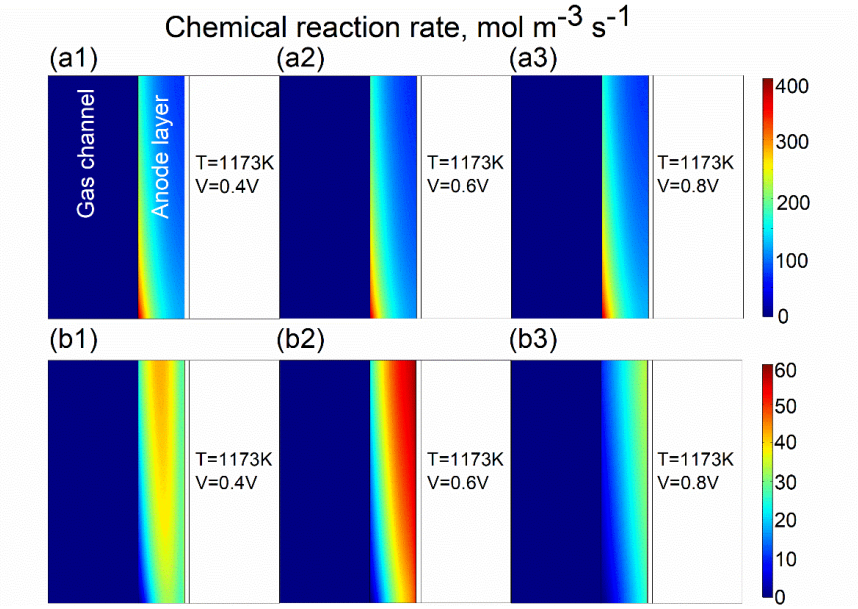

Figure 3.10 The reaction rate distributions at different potentials: (a1-a3) MDR; (b1-b3) WGSR.

The rate distributions of MDR and WGSR at three typical operating potentials (0.4 V 0.6 V 0.8 V) are also shown in Figure 3.10. It is obvious that peak rates and rate distributions for MDR in these three situations almost remain the same. For comparison, WGSR rates are quite different as the operating potential increases from 0.4 V to 0.8 V, which is mainly caused by the gas composition variation in the cell (Figure 3.11). When the operating potential is 0.4 V, high output current density tends to consume more CO and H_2 fuels, which favours the water gas shift reaction to generate H_2 but consume more CO as the hydrogen electrochemical oxidation is faster [71]. When the potential increases to 0.6 V, the molar fraction of CO is increased due to the decreased current density. Besides, H_2 consumption still benefits the water gas shift reaction despite low current density. Therefore, the higher molar fraction of CO at 0.6 V makes the rate of WGSR higher than the rate at 0.4 V. As the potential rises to 0.8 V, higher molar fraction of CO, lower consumption of hydrogen and lower generation of water because of the lower current density cause the lower rate of WGSR.

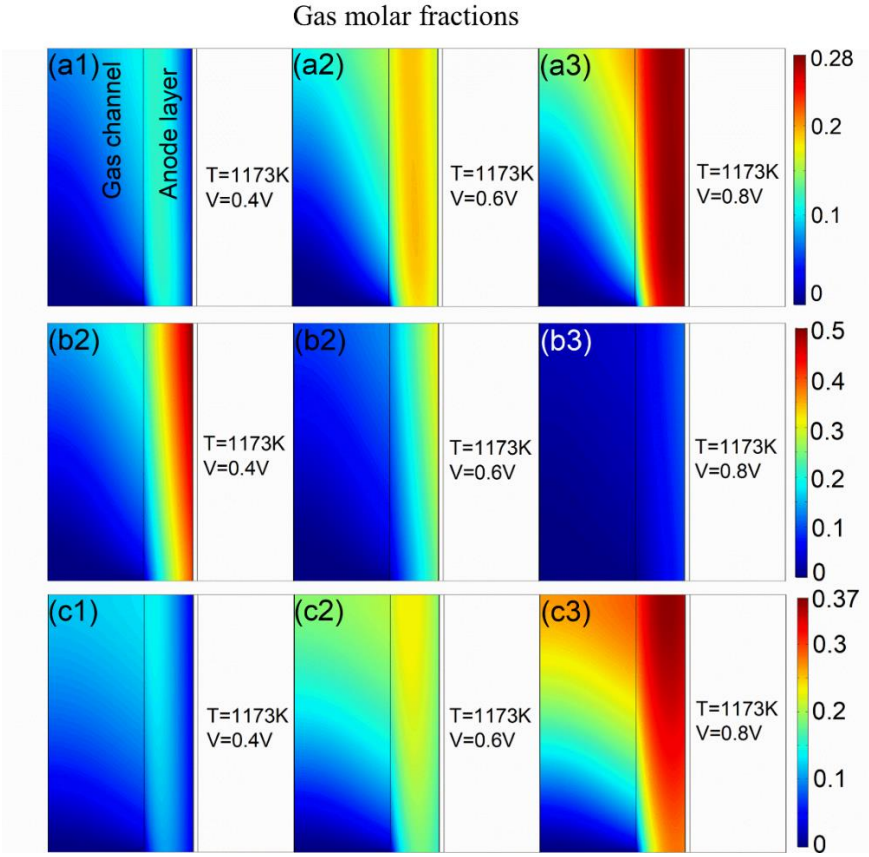

Figure 3.11 Gas compositions: (a1-a3) CO; (b1-b3) H_2O; (c1-c3) H_2.

3.4.4 The effect of structural dimensions

In tubular SOFCs, cell length and anode thickness are important structural parameters, because the longer length and thicker anode can provide more space for electrochemical/chemical reactions, which will affect the gas composition in the porous anode and thus the power output of SOFC. Therefore, the simulation is conducted to investigate the effects of the cell length and anode thickness on SOFC performance and methanol conversion at 1073 K and 0.6 V.

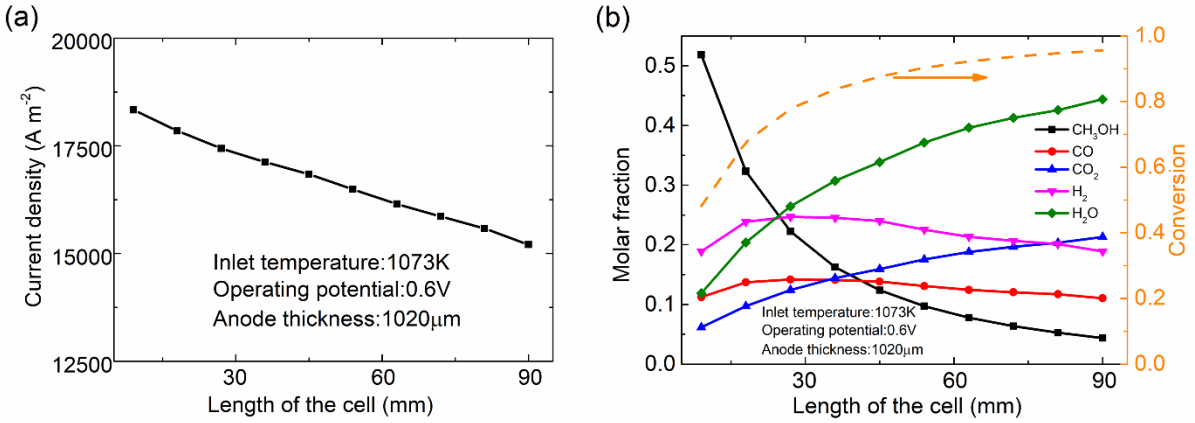

Figure 3.12 The effects of cell length on: (a) the output current density; (b) the CH_3OH conversion and gas composition at the outlet of the fuel channel.

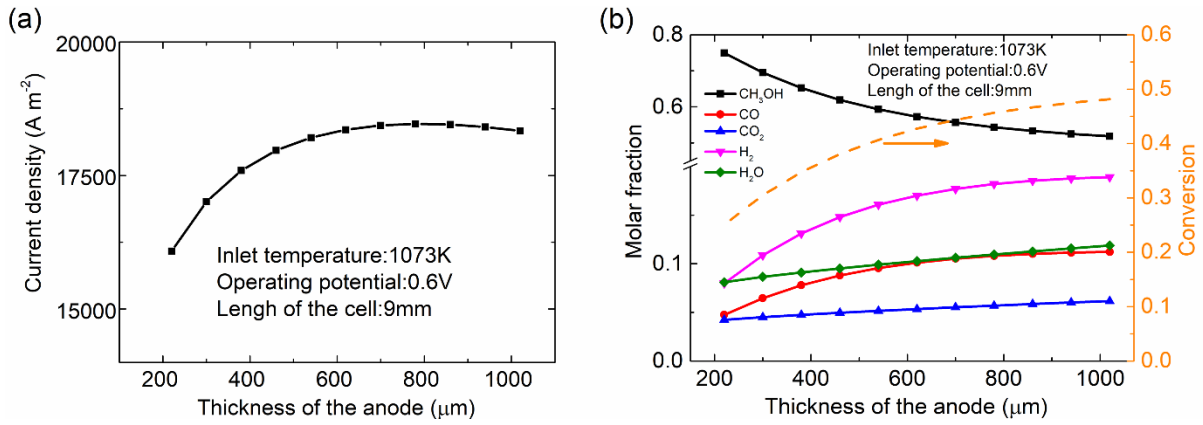

Figure 3.13 The effects of anode thickness on: (a) the output current density; (b) the CH_3OH conversion and gas composition at the outlet of the fuel channel.

The calculated output current density based on the different lengths is shown in Figure 3.12a. It can be observed that current density is decreased slightly when the cell length is increased from 9 mm to 90 mm, which is mainly caused by the combined effects of the decreased CO and H_2 and the increased H_2O and CO_2 (Figure 3.12b). It should be noted that as the cell length increases, uniform temperature assumption could not be suitable for current model due to the larger scale SOFC. Therefore, further investigation on performance effect of cell length could be conducted with considering heat transfer in future. Figure 3.12b shows the methanol conversion and gas molar fraction variations at the outlet of the fuel channel while the length varies. It indicates that methanol conversion is increased considerably at the beginning of the length increase and varies slightly when the length of SOFC exceeds 50 mm (reaches > 0.9 when the length is longer than 54 mm). Different from the effect of cell length on current density, anode thickness tends to benefit the electrochemical performance. Figure 3.13a shows that the current density is increased with increasing anode thickness. However, as the anode thickness is over 800 μm, a further increase in anode thickness causes the SOFC performance to decrease slightly. This is because a thicker anode benefits methanol conversion for H_2 and CO production (Figure 3.13b) but a too thick anode will cause a high gas diffusion resistance. As a result, an optimal anode thickness between 600 μm and 800 μm is suggested for the present direct methanol SOFC model. Cell length and anode thickness both benefit the methanol conversion, while they have different influences on SOFC performance. The increase in methanol conversion is due to more catalyst reaction sites, and the different effects on current density are because of different fuel concentrations.

3.5 Chapter conclusions

In this chapter, A 2D mathematic model is developed to investigate the current-potential characteristic of pure methanol-fuelled SOFC with considering the MDR and WGSR in the anode catalytic layer. It is found that the MDR rate is the highest (405 mol m^{-3} s^{-1}) near the

anode inlet and decreases along cell length, leading to a decrease in methanol concentration along the fuel channel, while the WGSR rate is the highest (15.2 mol m^{-3} s^{-1}) in anode downstream due to the reactant accumulation, which causes locally different distributions of hydrogen and carbon monoxide. Inlet temperature can considerably affect SOFC performance by facilitating the chemical and electrochemical reactions as well as ion conduction. Current density and gas composition are all significantly influenced by the operating potential. Current density is decreased with increasing potential, and the fuels (hydrogen and carbon monoxide) tend to accumulate in the anode at high operating potentials due to fewer consumptions. Although a thicker anode benefits the methanol conversion, anode thickness should not be too high to avoid significant resistance for gas diffusion (600 μm - 800 μm is suggested for the present model). In addition, the current density of SOFC is found to decrease with increasing cell length because of the gradual consumption of direct fuels for electrochemical reactions.

The chapter provides useful information to understand the mechanisms of SOFC running on pure methanol. Specific operating conditions and structural dimensions are found to improve the performance of SOFC.

Chapter 4: Thermo-electrochemical modelling of high temperature methanol-fuelled solid oxide fuel cells

4.1 Introduction

Typical Ni-based anode of SOFC might suffer from graphitic carbon deposition when methanol is used as a fuel, which could decrease the performance and durability of SOFC [48]. Fortunately, severe coking by methanol fuel could be thermodynamically less favourable than other hydrocarbons due to the presence of a C-O bond in methanol, instead of a C-C bond like ethanol (C_2H_5OH) [31]. Pure methanol fuelled anode-supported SOFC achieved a high power density of 0.6 and 1.3 W cm^{-2} at 650 ° and 800 ℃, respectively, and no visible carbon on the Ni/YSZ (yttria-stabilized zirconia) anode was detected after tests [55]. The SOFC with Ni/SDC (samarium-doped ceria) anode ran stably up to 160 hours with no degradations in both current density and voltage (0.5 V) when methanol was used as the fuel, demonstrating high resistance towards carbon formation [56]. With the same anode material, the stability test conducted by Meng et al. [57] exhibited reasonable stable operation for 60 hours at 0.8 A cm^{-2} and 600 ℃, and no carbon was deposited in the active anode layer although a small amount of carbon was detected in anode channel. High current density operation could be one of the most effective thermodynamic strategies to address the coking issue since high concentrations of electrochemical reaction products (carbon dioxide and steam) could suppress carbon formation thermodynamically [31]. If the current density is high enough, durable operation of dry methane fuelled SOFC could be achieved without carbon deposition [62]. Therefore, according to Cimenti et al [48], the long-term durability should be tested under low current density or OCV (open circuit voltage) to evaluate the coking resistance of SOFC anode. For example, deposited carbon was observed on the Ni-YSZ anode after 12 hours' operation with pure methanol at OCV condition, which subsequently led to severe electrode delamination from

electrolyte [93]. As the SOFC system needs to operate under various working conditions in practice including a zero output situation [48], coking formation could be an issue for pure methanol fuelled SOFC with Ni-based anode [53].

Apart from incorporating doped-ceria with high oxygen storage capacity into the anode ionic phase [48], several strategies were developed to inhibit carbon deposition for methanol fuelled SOFC, such as modifications of Ni-based anode with other metals (copper [60], palladium [63], molybdenum [69], and cobalt [70]) or the addition of coke tolerant basic oxides (La_2O_3, Sm_2O_3 [68], NbO_x [67], Pr_4O_7 and Pr_6O_{11} [66]). However, due to complicated manufacturing procedures, high cost and relatively low catalytic activity, these modification approaches are unlikely to be used for commercially practical applications. One simple and effective thermodynamic method to tackle the coking issue is to supply enough oxygen carrier agent to pure methanol fuel, such as steam [94]. According to the literature, the deposited carbon in methanol-fuelled SOFCs may be generated mainly from the Boudouard reaction (Eq. (4.1)) [60]. The supply of steam in the fuel stream could promote water gas shift reaction (WGSR, Eq. (3.2)) to reduce the partial pressure of carbon monoxide and produce more hydrogen or react with deposited carbon to form hydrogen and carbon monoxide (Eq. (4.2)), eventually preventing carbon formation. Laosiripojana et al. [65] found no carbon formation when the methanol/steam mixture with the ratio of 1.0/3.0 was supplied to Ni/YSZ catalyst at 1000 ℃. The stability test of Ni/YSZ anode SOFC operating on the mixture of methanol and steam with a ratio of 1.0/2.0 conducted by Ru et al. [64] achieved a stable output up to 120 hours at a current density of 0.221 A cm^{-2} and at 750 ℃.

$$2CO(g) \leftrightarrow CO_2(g) + C(s) \quad (4.1)$$

$$H_2O(g) + C(s) \leftrightarrow CO(g) + H_2(g) \quad (4.2)$$

The above-mentioned studies demonstrate the feasibility of strategies for suppressing carbon formation in methanol-fuelled SOFC with Ni-based anode, especially the strategy of supplying

sufficient steam to the fuel stream. Although sufficient steam could inhibit carbon formation, excess steam could lower the performance of the SOFC system [78]. Besides, the durability of methanol-fuelled SOFC could be substantially influenced by the use of steam in the anode. This is because the endothermic internal reforming or decomposition reaction of methanol would cause the local cooling and result in significant temperature gradients, though the electrochemical reactions and the overpotential losses tend to generate heat [8]. Therefore, highly coupled fluid flow, chemical/electrochemical reactions and heat/mass transfer processes complicate the temperature field inside the cell, which could induce thermal stress resulting from the temperature gradient and the mismatch of material TECs [15]. Meanwhile, the local low temperature might thermodynamically favour carbon formation in methanol-fuelled SOFC [53]. For stable and efficient operation of methanol fuelled SOFC, a comprehensive understanding of chemical/electrochemical reactions as well as heat and mass transfer is essential for identifying suitable operating conditions. However, although the thermal behaviour of SOFCs has been extensively studied, no thermo-electrochemical model has been reported for SOFC running on methanol and steam mixture. The temperature field and the interplay of various operation parameters have not been understood yet.

In this work, the 2D numerical model from the last chapter [74] is extended to fully describe the performance and the thermal behaviours of a tubular SOFC operating on methanol/steam fuel with the typical Ni/YSZ-YSZ-YSZ/LSM configuration without considering the carbon formation due to the operating conditions adopted in this chapter. Modelling results are compared with the experimental data [55] for model validation. The thermal coupling of the methanol conversion process and electrochemical reactions of carbon monoxide as well as hydrogen are conducted in detail to examine the effects of operating conditions (applied potential and inlet temperature) and fuel conditions (fuel composition and flow rates) on the power output and temperature distribution of SOFC.

4.2 Model development

In this work, the mixture of H_2O/CH_3OH with various S/C ratios is supplied to the SOFC anode channel for power generation. The computational domain includes five components, involving anode channel, porous Ni/YSZ composite anode, gas-tight YSZ ceramic electrolyte, porous YSZ/LSM composite cathode, and cathode channel based on the experimental work studied by Jiang et al [55]. Note that interconnect rib is not included in the geometry of the fuel cell because a 2D model is conducted in this simulation work. Because interconnect rib is an important component for the integrity of fuel cell, which could significantly affect the gas transport, chemical reactions and thus the performance of SOFCs, the rib effect could be considered in future 3D simulation work. In addition, there are some modifications of structural dimensions in the current work compared to our previous study [74], and typical geometric parameters used in this simulation work are listed in Table 4.1.

Table 4.1 Structure dimensions of SOFC Model.

Parameter	Expression or value	Unit
Thickness		
Anode channel	2	mm
Anode	0.6	mm
Electrolyte	0.01	mm
Cathode	0.1	mm
Cathode channel	2	mm
Cell length	6	cm

During operation, ambient air and steam/methanol mixture are supplied to air and fuel gas channels, respectively. Methanol can be easily converted into syngas under the catalytic effect of Ni metal via methanol decomposition reaction as methanol fuel diffuses into the anode. Meanwhile, carbon monoxide tends to react with sufficient steam supplied or generated from the electrochemical oxidation of hydrogen to produce more hydrogen through water gas shift reaction. Besides, although a certain amount of methane could be produced from the

methanation reaction in practice, due to the requirements of high pressure and a relatively low temperature for the methanation process [65], methane is considered negligible in present work.

The produced hydrogen and carbon monoxide are oxidized to form the steam and carbon dioxide at TPB by O^{2-} transported from the cathode where the oxygen molecules are reduced by the electrons transferred from the anode through the external circuit.

Based on the mechanism demonstrated above, the following assumptions are adopted.

(1) Only electrochemical oxidations of hydrogen and carbon monoxide are considered.

(2) The ionic/electronic phases are assumed to be continuous and homogeneous.

(3) The active catalyst sites for chemical/electrochemical reactions are uniformly distributed in electrodes and nickel metal will not be re-oxidized by steam.

(4) Gases are assumed to be ideal gases.

(5) The laminar flow is adopted in the fluid flow since the Reynolds number of the fuel stream or air stream is relatively low.

(6) The heat radiation effect is assumed to be negligible.

4.3 Numerical methods and validation

The model is developed and calculated by the commercial software COMSOL using the Finite Element Method. The mesh of 52 000 elements is selected to achieve grid-independence of results. The numbers of mesh elements for cell length, anode channel, anode, electrolyte, cathode, and cathode channel widths are 200, 30, 150, 10, 40, and 30, respectively. The model was validated by comparing with experimental results [55] in our earlier work [74]. The parametric computations are conducted afterwards to investigate the effects of operating conditions on performance and thermal characteristics. The operating conditions are summarized in Table 4.2.

Table 4.2 Working parameters for parametric simulations.

Parameters	Value	Unit
Anode fuel flow rate (liquid)	0.05-1	ml min^{-1} (std)

Cathode gas flow rate	10-600	SCCM
S/C ratio at the anode inlet	H_2O/CH_3OH (1/1 – 8/1)	
Cathode inlet gas composition	O_2/N_2 (21%/79%)	
Inlet temperature	898-1173	K
Operation potential	0.2-0.9	V
Operation pressure	1	atm

4.4 Results and discussions

4.4.1 The effects of operating voltage

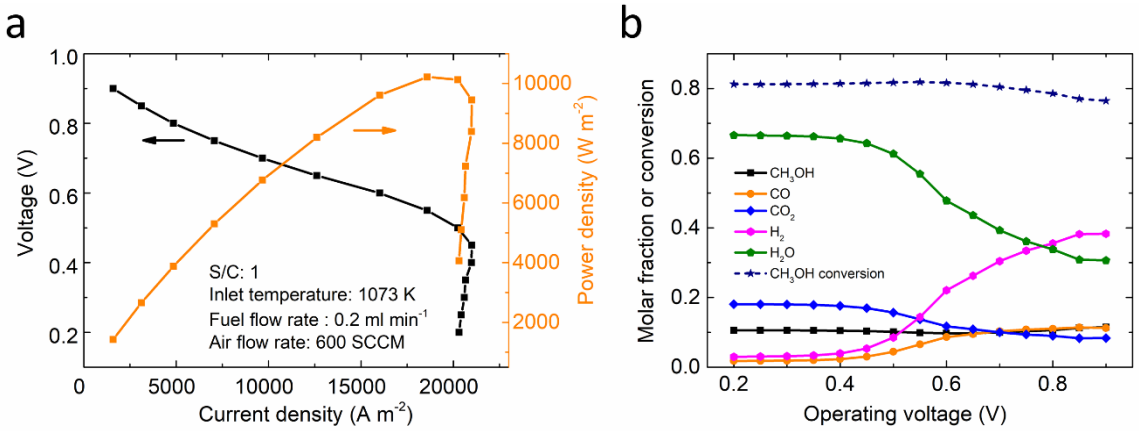

Figure 4.1 The effects of operating voltage on: (a) current density and power density; (b) anode gas fraction at the outlet and methanol conversion.

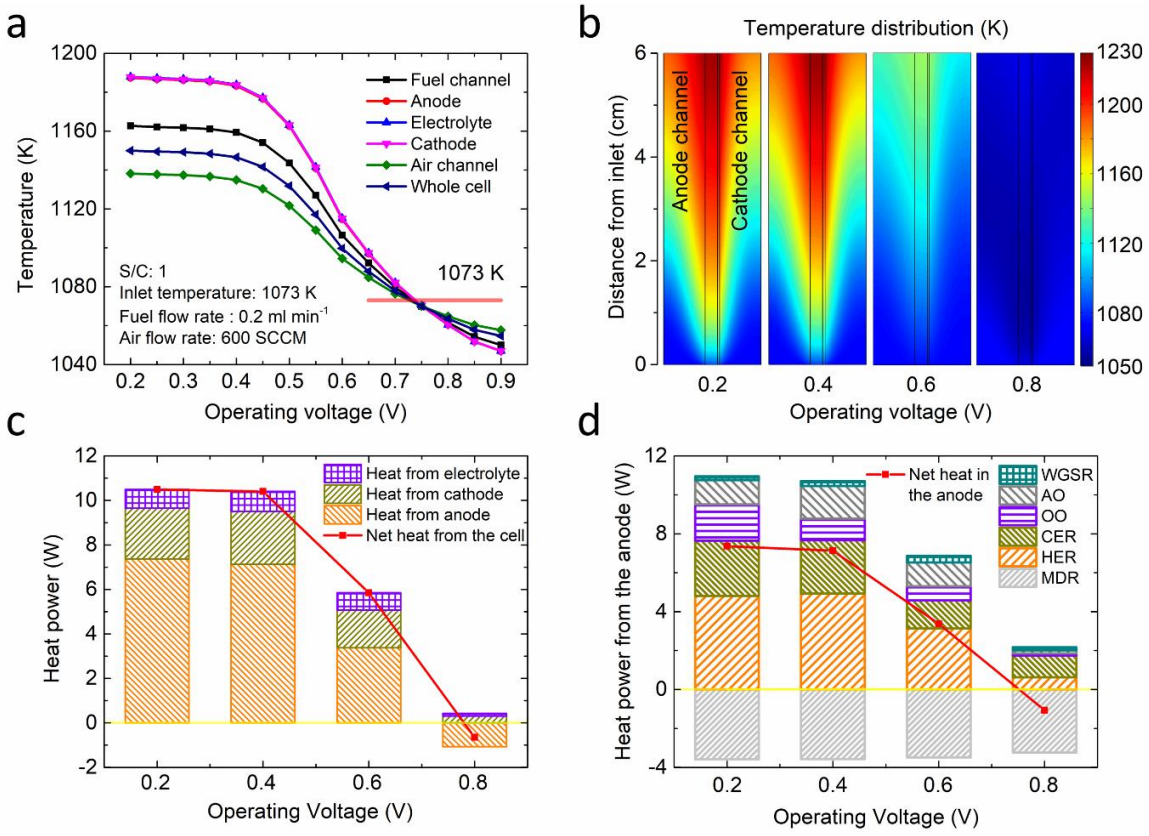

Figure 4.2 The effects of operating voltage on: (a) average temperature of each component; (b) temperature distribution; (c) heat source of each component; (d) heat source of anode (AO: activation overpotential; OO: ohmic overpotential; CER: carbon monoxide electrochemical reaction; HER: hydrogen electrochemical reaction).

Simulations are conducted at an inlet temperature of 1073K to investigate the effects of operating voltage on the performance of SOFC running on steam/methanol mixture with a molar ratio of 1/1. The calculated current density shown in Figure 4.1a is found to be significantly affected by operating voltage changing from 0.9 V to 0.2 V when flow rates for fuel and air are 0.2 ml min^{-1} and 600 SCCM, respectively.

As expected, the current density is greatly improved from 1585 A m^{-2} to 20997 A m^{-2} when the voltage decreases from 0.9 V to 0.45 V. Meanwhile, a peak power density of 10220 W m^{-2} is achieved at 0.55 V, which is much higher than that (usually less than 1000 W m^{-2}) of typical room temperature direct methanol fuel cells (DMFCs) [95,96]. Besides, the gas composition is also greatly influenced. Highly consumptions of direct fuels (carbon monoxide and hydrogen) for electrochemical reactions and increased products (steam and carbon dioxide) are observed in Figure 4.1b at a high current density. As a result, the enhanced consumption of hydrogen and carbon monoxide fuel help improve the methanol conversion slightly to be above 0.8 as the voltage is decreased from 0.9 V to 0.6 V. However, increased amount of gas molar number because of decomposition reaction, and the relatively low methanol concentration limit the further increase in methanol conversion, as the voltage is further decreased from 0.6 V to 0.2 V (Figure 4.1b). As the methanol conversion is not further increased and the syngas fuel is consumed by electrochemical reactions, the current density is found to decrease slightly with a further decrease in operating voltage from about 0.45 V to 0.2 V (Figure 4.1a).

The operating voltage also has a strong influence on cell temperature distribution, as illustrated in Figure 4.2a and b. The average temperature of each component is found to

increase with decreasing voltage due to the increased rate of heat generation from electrochemical reactions and various overpotential losses (Figure 4.2c and d). More importantly, when the operating voltages are 0.2 V and 0.4 V, the temperature of fuel cell is increased significantly along the cell length, as shown in Figure 4.2b, which is mainly because of the highly enhanced exothermic processes at low operating voltages (Figure 4.2c) and also the heat convection effect caused by the gas supply. Therefore, a huge difference in the temperature within the fuel cell should be avoided in practical operation since a high-temperature gradient could induce unbearable thermal stress and even the failure of the whole fuel cell. One interesting phenomenon from Figure 4.2a is that the average temperatures of anode, cathode and electrolyte are nearly the same. This is because the high thermal conductivities of solid materials ensure fast heat conduction. In addition, due to the endothermic methanol decomposition reaction, thermal neutral status can be attained between 0.7 V to 0.8 V (Figure 4.2a), which indicates that the total heat generation rate is equal to the rate of heat consumption by the MDR (Figure 4.2c and d). Despite the overall thermal balance, the highly non-uniform temperature distribution in SOFC could cause concerns for long-term performance and durability. For example, a cooling spot near the inlet can be seen at a potential of 0.8 V in Figure 4.2b, which is consistent with the operation of SOFC running on a fuel mixture of methane and steam [97]. The temperature of this region is found lower than inlet temperature because of the high rate of endothermic MDR and relatively low electrochemical reaction rate, which can cause local low cell performance and large thermal stress.

4.4.2 The effects of steam to carbon ratio

To prevent carbon deposition in SOFC anode, steam is supplied with methanol fuel. Different amounts of steam with the steam to carbon (S/C) ratio from 1 to 8 are supplied under different fuel flow rates at 1073 K and 0.6 V when the air flow rate is 600 SCCM. From Figure 4.3, it is clear to observe that current densities are decreased with increasing S/C ratio at various

fuel flow rates, which is mainly due to the high dilution effect on methanol fuel and the produced syngas fuel (Figure 4.4a). On the one hand, the methanol decomposition rate is decreased due to low methanol concentration (Figure 4.4b), causing much fewer productions of carbon monoxide and hydrogen for electrochemical reaction. On the other hand, the produced syngas fuel is also diluted by steam, leading to low local equilibrium potential and low current density. Meanwhile, the total heat generation is decreasing due to the decreased current density as the S/C ratio increases (Figure 4.4c), leading to a much more uniform temperature distribution in the cell (Figure 4.4d). In general, due to the porous nature of electrodes, fraction strengths of compressive stress for electrodes (e.g. 100 MPa for both NiO/YSZ and LSM/YSZ when the porosity is 0.4 [98]) are much lower than that of dense electrolyte (e.g. 1 GPa for YSZ [99]). Therefore, a more uniform temperature distribution in electrodes is significantly important for the durability of the SOFCs.

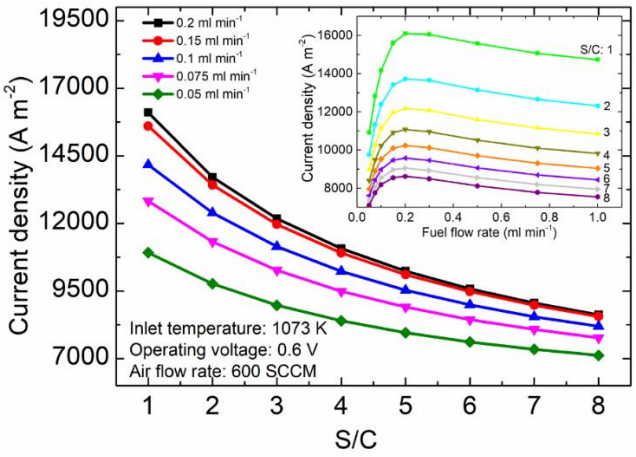

Figure 4.3 The effect of S/C ratio on current density.

Besides, the current densities can also be influenced by fuel flow rate (Figure 4.3). At a lower fuel flow rate, methanol is almost exhausted (Figure 4.5a), and syngas is insufficient in downstream for electrochemical reactions, as shown in Figure 4.5b. With increasing fuel flow rate, more methanol is supplied to produce more syngas, which will help increase the local equilibrium potential and thus local current density (Figure 4.5b). However, as the fuel flow

rate approaches 0.2 ml min^{-1}, the performance improvement becomes insignificant. A further increase in flow rate to 1.0 ml min^{-1} could even decrease the cell performance (Figure 4.3) as a high fuel flow rate can easily take away the produced CO and H_2, leading to low CO/H_2 concentrations (Figure 4.5b) and low SOFC performance. Furthermore, the conversion is decreasing with increasing fuel flow rate (Figure 4.5c), because at a higher velocity (Figure 4.5d) there is more unreacted methanol flowing away from the fuel channel (Figure 4.5a), leading to the low efficiency of fuel cell system. Also, an increase in the S/C ratio results in a drop in methanol conversion (Figure 4.5c) since a high S/C ratio leads to a fast fuel gas mixture velocity (Figure 4.5d). Moreover, it is also found that current density enhancement by fuel flow rate (less than 0.2 ml min^{-1}) is more significant at a low S/C ratio (Figure 4.3). This phenomenon is caused by the fact that methanol molar fraction increase by accelerating the fuel flow rate at a small S/C ratio is much more considerable than that at a high S/C ratio (Figure 4.6a), thus leading to larger performance improvement at a lower S/C ratio.

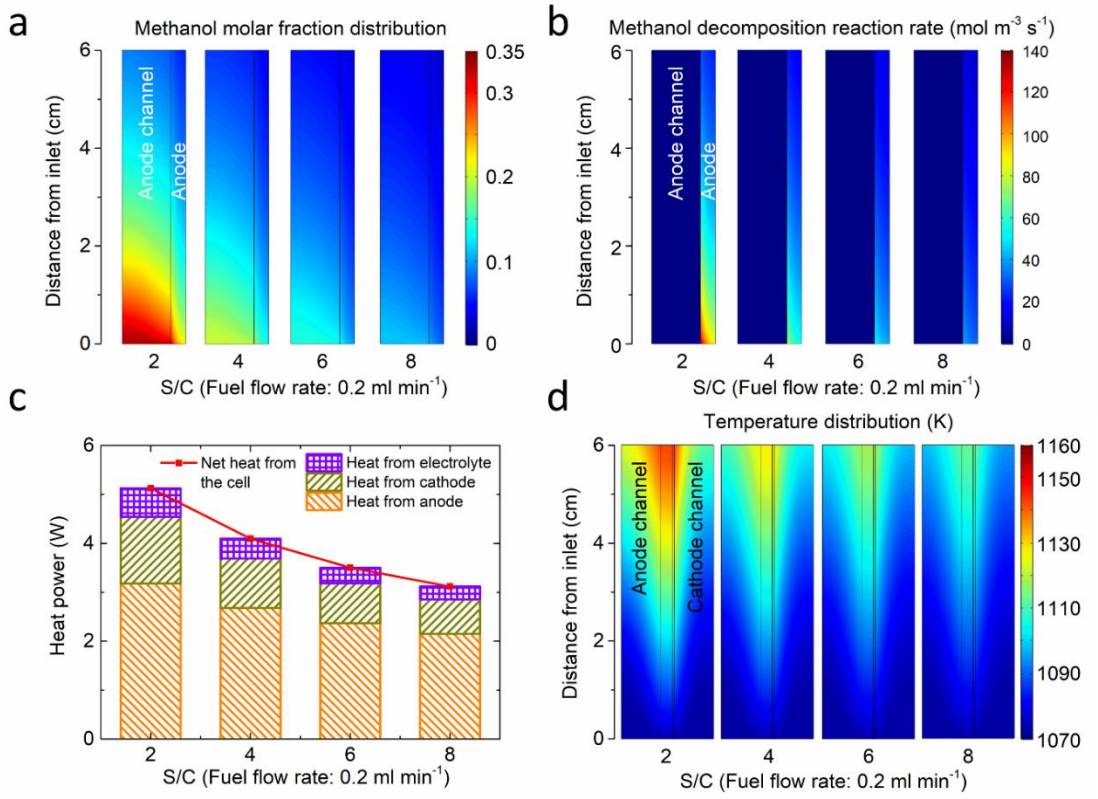

Figure 4.4 The effects of S/C ratio on: (a) methanol molar fraction; (b) MDR rate; (c) heat

source of each component; (d) temperature distribution.

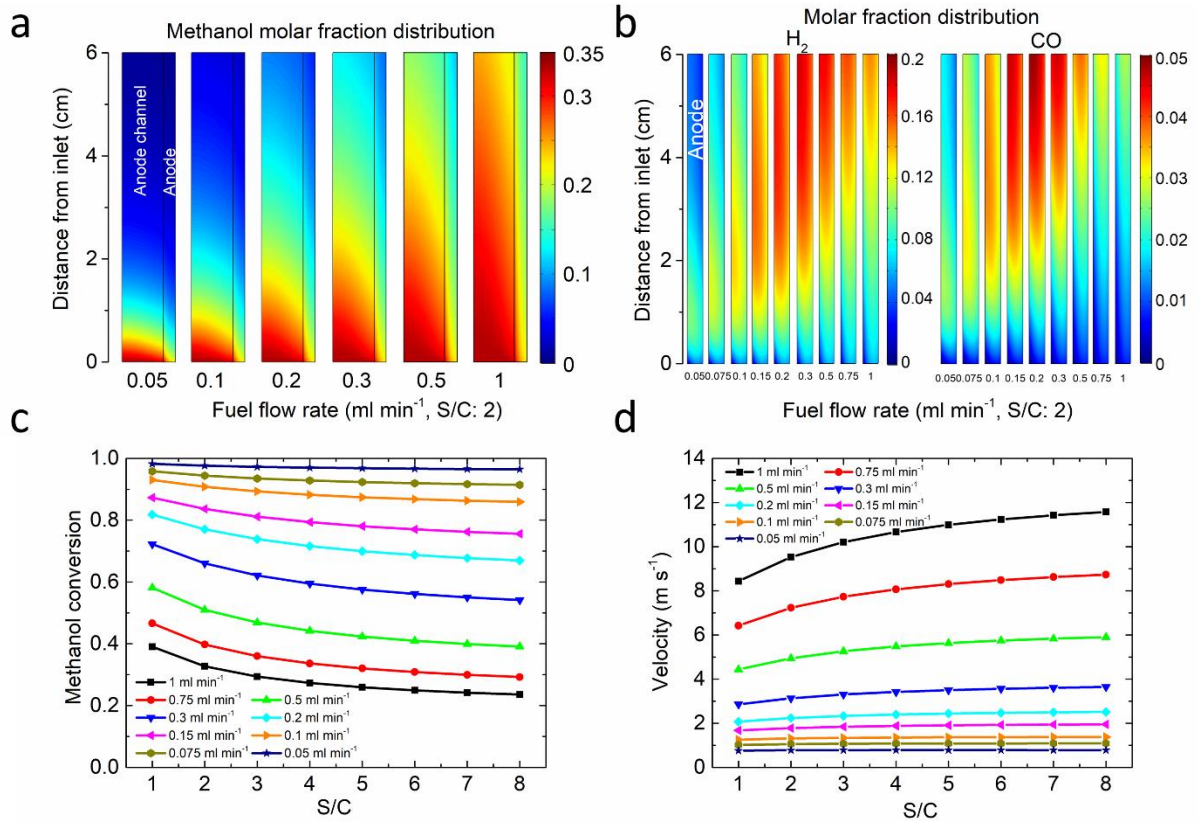

Figure 4.5 The effects of fuel flow rate on: (a) methanol molar fraction; (b) hydrogen and carbon monoxide molar fractions; (c) methanol conversion; (d) the average velocity at the centre of the fuel channel.

The fuel flow rate also plays a role in the temperature distribution within the whole cell. When the fuel flow rate increases from 0.05 ml min^{-1} to 0.1ml min^{-1}, the peak temperature near the outlet is found to increase because of increased current density (Figure 4.6b). However, there is a noticeable decrease in peak temperature when the fuel flow rate further increases from 0.1 ml min^{-1}, which is mainly caused by the multi-effect of a faster flow rate. As just mentioned, a relatively high fuel rate (less than 0.2 ml min^{-1}) can improve the performance of SOFC, so the total heat generation by electrochemical reactions and overpotential losses are accordingly increased. However, sufficient methanol benefits the endothermic methanol decomposition reaction, which is evidenced by the heat consumption shown in Figure 4.6d. This can lead to a slight drop in the total heat generation as the fuel flow rate is increased from

0.15 ml min^{-1}, as shown in Figure 4.6c. Therefore, the increase of peak temperature with increasing fuel flow rate from 0.05 ml min^{-1} to 0.1ml min^{-1} indicates higher heat generation than heat consumption. When the fuel flow rate is increased from 0.1 ml min^{-1} to 0.15 ml min^{-1}, the faster flow velocity (Figure 4.5d) in the fuel channel takes away more heat by convection leading to the decrease in peak temperature although the total heat is still increasing. Both faster fuel flow velocity and the drop of total heat generation decrease the peak temperature when the fuel flow rate increases from 0.15 ml min^{-1}.

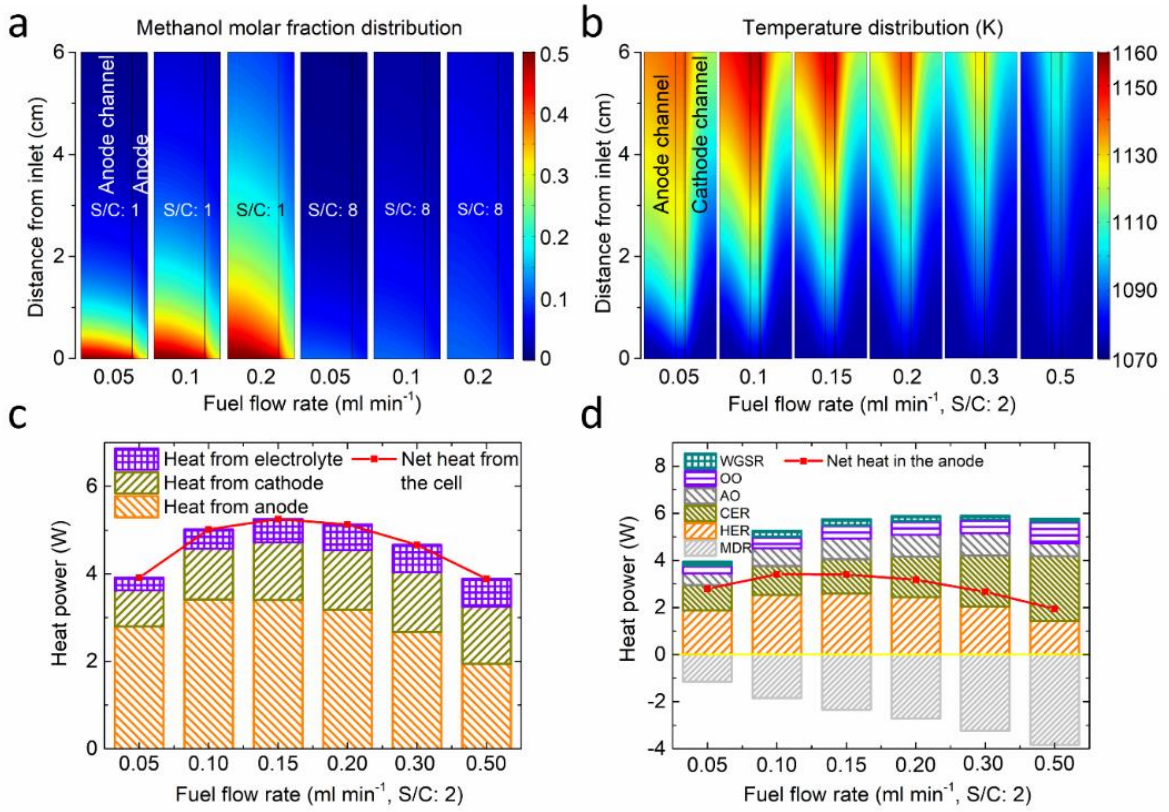

Figure 4.6 (a) effects of fuel flow rate and different S/C ratios on methanol molar fractions; The effects of fuel flow rate on: (b) temperature distribution; (c) heat source of each component; (d) heat source of the anode.

4.4.3 The effects of air flow rate

The air flow rate is another essential parameter for SOFC operation. Simulations are performed under various air flow rates and different S/C ratios at an inlet temperature of 1073 K, fuel flow rate of 0.2 ml min^{-1} and the operating potential of 0.6 V.

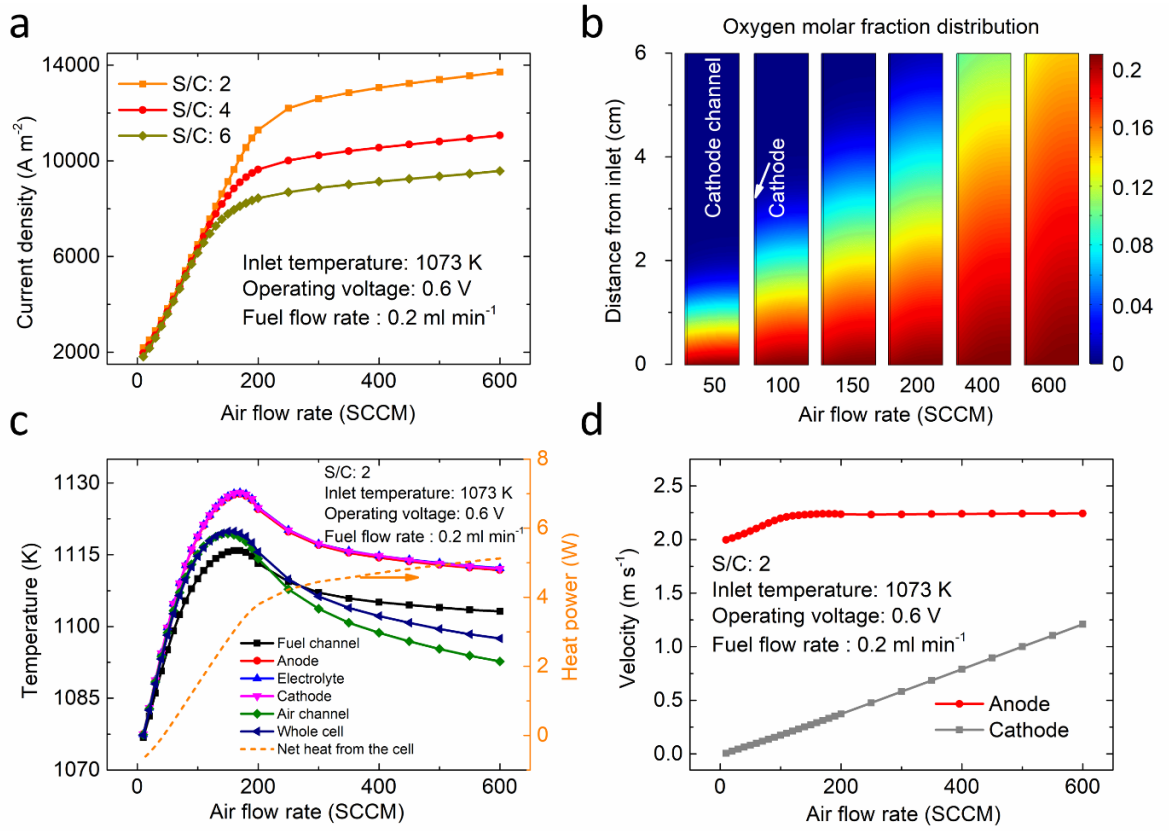

Figure 4.7 The effects of air flow rate on: (a) current density; (b) oxygen molar fraction; (c) average temperature of each component; (d) average velocities at the center of the fuel and air channels, respectively.

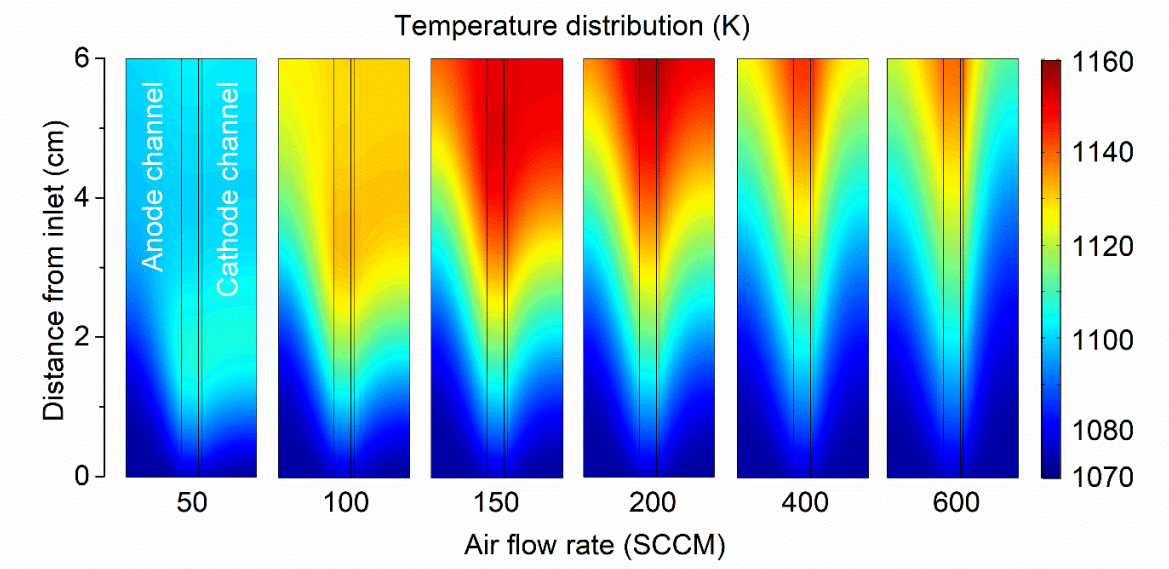

Figure 4.8 The effect of air flow rate on temperature distribution.

As can be seen from Figure 4.7a, the computed current densities increase very significantly with increasing air flow rate, especially below 200 SCCM. when the air flow rate is between 10 and 160 SCCM, current density curves show the same changes at different S/C ratios as the SOFC performance is limited by the low oxygen concentration in the cathode, especially the downstream (Figure 4.7b). When the air flow rate exceeds 200 SCCM, the oxygen supply is sufficient and anode gas composition determines the performance, causing different current densities under different S/C ratios (Figure 4.7a). From Figure 4.7c, the average temperature of each component is also greatly affected by the air flow rate. Due to the significantly increased current density and thus increased heat generation (orange line in Figure 4.7c) with increasing air flow rate, the average temperature of each component is found to increase as the air flow rate is increased from 10 to about 170 SCCM. However, a further increase in air flow rate causes average temperatures to decrease as the fast air flow can easily take away the generated heat (Figure 4.7d). The largest temperature drop occurs in air channel (olive line in Figure 4.7c), thereby leading to the drop in cell temperature, which is consistence with the temperature distributions in Figure 4.8. Normally, cell active cooling is achieved by the oversupply of air into the cathode channel [9], increasing energy consumption for heating air and thus the operating cost of SOFC. Figure 4.8 shows the temperature distribution under various air flow rates. The peak temperature is found in the middle and the temperature decreases along cell length from the peak temperature area at low air flow rates, mainly due to the exhausted oxygen (Figure 4.7b) and endothermic decomposition reaction. At high air flow rates, temperature increases along the cell length and peak temperature occurs at the outlet, which is caused by the fact that exothermic processes are greatly enhanced.

4.4.4 The effects of inlet temperature

Inlet temperature has great impacts not only on the reactions involved in SOFC but also on material properties and gas species. In addition, because of complex endothermic and

exothermic processes, the average cell temperature could be substantially different from the inlet temperature. Therefore, in this section, simulations are conducted to study the effects of the inlet gas temperature on SOFC performance under several S/C ratios at a potential of 0.6 V, and fuel and air flow rates of 0.2 ml min^{-1} and 600 SCCM, respectively.

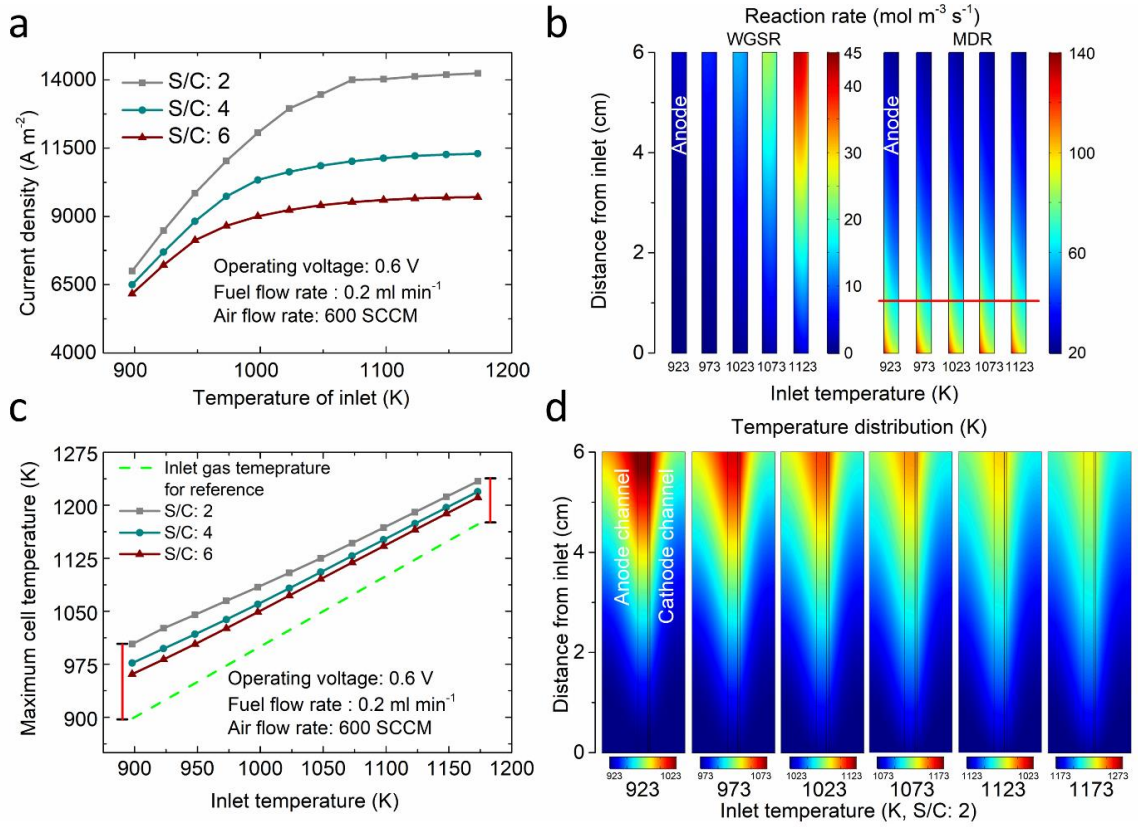

Figure 4.9 The effects of inlet temperature on: (a) current density; (b) rates of the WGSR and MDR; (c) maximum temperature in the SOFC; (d) temperature distribution.

As expected, simulated current densities are found to increase when the inlet temperature is changing from 893 K to 1173 K (Figure 4.9a) because of the higher rates of chemical/electrochemical reactions and higher ion conductivity at a higher operating temperature. Highly increased water gas shift reaction rate and slightly increased methanol decomposition rate tend to produce more direct fuels for power generation (Figure 4.9b). Although the maximum temperature increases with increasing inlet temperature, the difference between maximum temperature and inlet temperature becomes smaller (Figure 4.9c) due to the combined effect of faster gas velocities in fuel and air channels (Figure 4.10a) and slower rise

or even slight drop of total heat generation when inlet gas temperature is increasing (Figure 4.10b, c and d), enhancing the temperature uniformity (Figure 4.9d). Generally, after the significant increase at the beginning of temperature rise, total heat generation faces a decline from 1073 K for both S/C ratios of 4 (Figure 4.10c) and 6 (Figure 4.10d), and from 1123 K for the S/C ratio of 2 (Figure 4.10b). The slight decrease of heat generation at high inlet gas temperatures is mainly because the drop of heat power generated from electrolyte (Eq. (2.45)) caused by the improved ionic conductivity, could overcome the increases in heat generations from anode and cathode even though current densities are continuing improved (Figure 4.9a). It is also obviously observed that the porous anode contributes most to the total heat generation, which is mainly caused by the irreversible entropy changes of H_2 and CO electrochemical reactions at a higher current density (Eq. (2.44)).

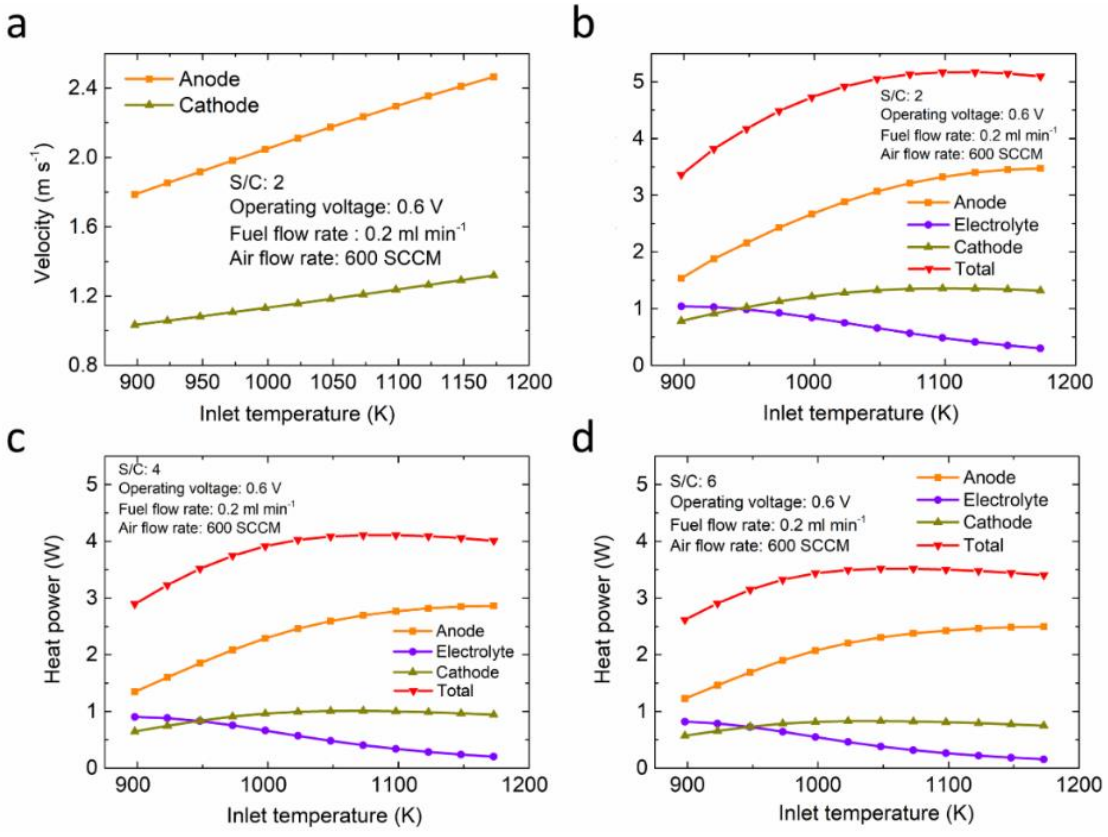

Figure 4.10 The effects of inlet temperature on: (a) average velocities at the centre of the fuel and air channels; (b) heat source of each component at a S/C ratio of 2; (c) heat source of each component at a S/C ratio of 4; (d) heat source of each component at a S/C ratio of 6.

4.5 Chapter Conclusions

A mathematic model is established to examine the thermal characteristics of a tubular methanol-fuelled SOFC with the addition of adequate steam into the fuel stream to suppress carbon deposition. The model fully considers the thermal coupling of endothermic methanol decomposition reaction with cell inefficiencies, investigating the influences of various essential operating parameters, involving applied potential, inlet gas temperature, steam to carbon ratio, as well as fuel and gas flow rates. Performance and the thermal effect indicators, including current density, temperature distribution, gas molar fraction, chemical reaction rate etc. are comprehensively discussed in parametric simulations.

The peak power density of 10220 W m^{-2} is attained when the fuel mixture with equal molar amounts of steam and methanol is fed into SOFC at 0.55 V and 1073 K. Stagnant methanol conversion and the nearly exhausted synthesis gas cause a slight drop in the current density as voltage further decreases from 0.45 V. High S/C ratio tends to dilute methanol fuel and the generated syngas, leading to the reductions in electrical power and the total heat generation. It is found that increasing the fuel (less than 0.2 ml min^{-1}) or air flow rates improves SOFC performance, and it also serves as a cooling strategy for cell temperature control. However, side effects of high fuel and air flow rates are low fuel conversion and additional energy input, which could negatively affect the efficiency of the whole system. The rise of inlet temperature from 898 K to 1173 K significantly enhances the power performance due to higher syngas production rates, higher oxygen ion conduction, and higher electrochemical reaction kinetics of electrodes at elevated inlet temperature. Meanwhile, the improved ion conduction and electrode reaction kinetics also contribute to the reduction of heat generation, leading to more uniform temperature distribution. Overall, the results of this chapter provide insightful information on the thermal characteristics of high-temperature methanol-fuelled SOFCs, which are critical for SOFC performance and durability.

Chapter 5: Temperature gradient analyses of tubular SOFC fuelled by methanol fuel

5.1 Introduction

Despite numerous benefits involved in the SOFC system, the question of thermal management has been a major challenge [100]. Because of uneven electrochemical reactions and heat transfer of gas convective flows, non-uniform temperature distributions within SOFC assembly or stack were frequently observed, especially for internal reforming SOFCs, which poses a threat to material deterioration and structural integrity. Local high temperatures higher than the design value could lead to nickel coarsening because of the relatively low melting temperature of nickel metal as well as thermally favourable sintering process [101], degrading anode functions and thereby lowering cell performance. For example, electrode sintering was found at the bottom part of a tubular SOFC operated on methane flame mode since the temperature of the corresponding position reached 1300 K [102]. Another thermal issue is that the temperature gradient arising from the non-uniform temperature distribution tends to negatively affect cell structure given the applied thermal stress, which may lead to the crack or delamination of brittle ceramic components that are more vulnerable under tensile stress [103]. For example, both delaminations between electrolyte and electrode as well as cracks in electrolytes were found in experimental tests due to the presence of temperature gradient [102,104], which is likely to result in the complete failure of SOFCs as their components cannot be replaced or repaired [9]. Therefore, under the complicated thermal environment of SOFC, cell components seem to be subject to the accelerated rate of property evolution and degradation, eventually contributing to the failure of fuel cell.

To solve the problems mentioned above, various efforts have been devoted to developing temperature control strategies in recent years. Zeng et al. [102] experimentally fabricated a

tubular SOFC with a liquid-sodium heat pipe aiming to equalize the temperature distribution. It is found that with the help of high thermal conductivity induced by the evaporation-transport-condensation process of liquid sodium, the axial temperature gradient was significantly decreased, leading to enhanced cell electrochemical performance and life span. Dillig et al. [105] and Marocco et al. [106] have drawn similar conclusions in their simulation investigations. Recently, Promsen et al. [107] proposed a novel concept of SOFC cooled by saturated water. The calculation results indicated the water-cooled stack exhibited better performance as a result of a more uniform temperature profile. Besides, thanks to the effective cooling of saturated water, the air flow rate could be greatly reduced since conventional means of heat dissipation in SOFC is typically carried out by oversupplying cathode gas, decreasing the parasitic loads related to air pre-heating and blower energies. However, although the design of combining SOFC with a heat pipe or water cooling tube shows benefits in enhancements of temperature uniformity and electrochemical performance, as well as cost reduction related to auxiliary devices, manufacture cost and system complexity remain a challenge, especially for SOFC stacks, because plenty of heat pipes should be fabricated into the stack to achieve sufficient cooling effect [106]. Besides, possible leakage of liquid metal from heat pipe might bring catastrophic damage to the cell system given the complicated gas environment and chemically reactive nature of liquid metal. Based on the same approach of increasing the thermal conductivity of solid cell components, utilization of metal support [108,109], metallic interconnect [110] or metal cathode flow distributor [111] in the fabrication of SOFC also exhibited a more uniform temperature distribution, leading to improved cell stability in terms of thermal stress [110]. However, as indicated from the numerical study conducted by Park et al. [112], the bonding layer between ceramic cell and metallic support resisted hydrogen mass transfer, resulting in a 17% decrease in average current density compared to cermet anode-supported SOFC. Besides, possible metal oxidation risk [113], accelerated poisoning of

cathode catalyst by Cr from ferritic stainless steel [114] as well as relatively poor electrochemical performance [115] have still limited the commercialization of this technology.

However, despite lots of theoretical and experimental works conducted with a focus on thermal control and management, as far as the author knows, no detailed thermo-electrochemical simulation has been investigated to identify the thermal characteristics, especially temperature gradient profile, of a SOFC operated on methanol fuel. Importantly, different from the battery, SOFC is an open system that thermally interacts with reacting gases, which indicates that cell thermal state will be considerably influenced by gas conditions [116], especially for cathode air, but the cooling effectiveness and thermal/electrical responses of air flow conditions have not been fully understood yet. Therefore, to fill this research gap, a validated mathematic model extended from our previous simulation works [74,117] is developed to further identify the knowledge of temperature gradient profiles in cell components, especially ceramic electrolyte, which will be critically essential for operating condition selection, structure design and failure assessment of realistic SOFCs.

5.2 Model development

A fuel mixture of methanol and steam (molar ratio:1) is supplied into the fuel channel to electrochemically generate electricity. Macro and micro-structural parameters, as well as the physical properties of materials adopted in present study, are set to be consistent with our previous work.

Based on the working mechanism of SOFC fuelled by methanol/steam mixture, assumptions adopted in the simulation are given below.

(1) As a result of kinetically fast reaction rates, only hydrogen and carbon monoxide could be electrochemically oxidized.

(2) Local temperature equilibrium hypothesis is applied for porous electrodes because of the negligible temperature difference of gas/solid phases [118].

(3) The heat transfer involved in the current model includes heat conduction as well as heat convection.

(4) Because of the relatively low Reynolds number in gas channels considering flow velocity and characteristic length, an incompressible laminar flow regime is used for bulk fuel and air flows.

(5) Gases simulated are treated as ideal gases.

(6) The evenly dispersed electrochemical/chemical reaction sites are assumed in both electrodes, and continuous and homogeneous ionic/electronic conductions are adopted.

5.3 Mathematic method and operating conditions

Table 5.1 Working conditions for parametric simulation.

Parameters	Value	Unit
Cathode gas flow rate	120-2400	SCCM
Cathode gas composition	O_2/N_2 (21%/79%)	
Anode flow rate (liquid)	0.2	ml min^{-1} (std)
Anode gas composition	H_2O/CH_3OH (molar ratio: 1/1)	
Inlet temperature	873-1113	K
Operating potential	0.5-0.9	V
Operating pressure	1	atm

The developed model is simulated by solving fully-coupled nonlinear equations through the Finite Element Method with a relative tolerance of 10^{-3}. To ensure grid independence, the model is composed of 30, 150, 10, 40, and 30 elements for anode channel, anode, electrolyte, cathode, and cathode channel widths, respectively, as well as 200 for cell length, generating 52,000 elements. Besides, the validation was conducted by comparing calculated polarization curves with experimental data [34], which could be readily found in our published studies [32,33]. Working conditions for the following parametric calculation are given in Table 5.1.

5.4 Results and discussions

5.4.1 The effects of air flow rate

Calculations are employed to examine the effects of air flow rate on tubular cell thermal/electrical performance under several typical operating temperatures. Here, operating potential is set as 0.5 V. This is because although a large current density or low operating potential is not desired in practical operations, negative thermal features are likely to become quite obvious under a considerably high current density.

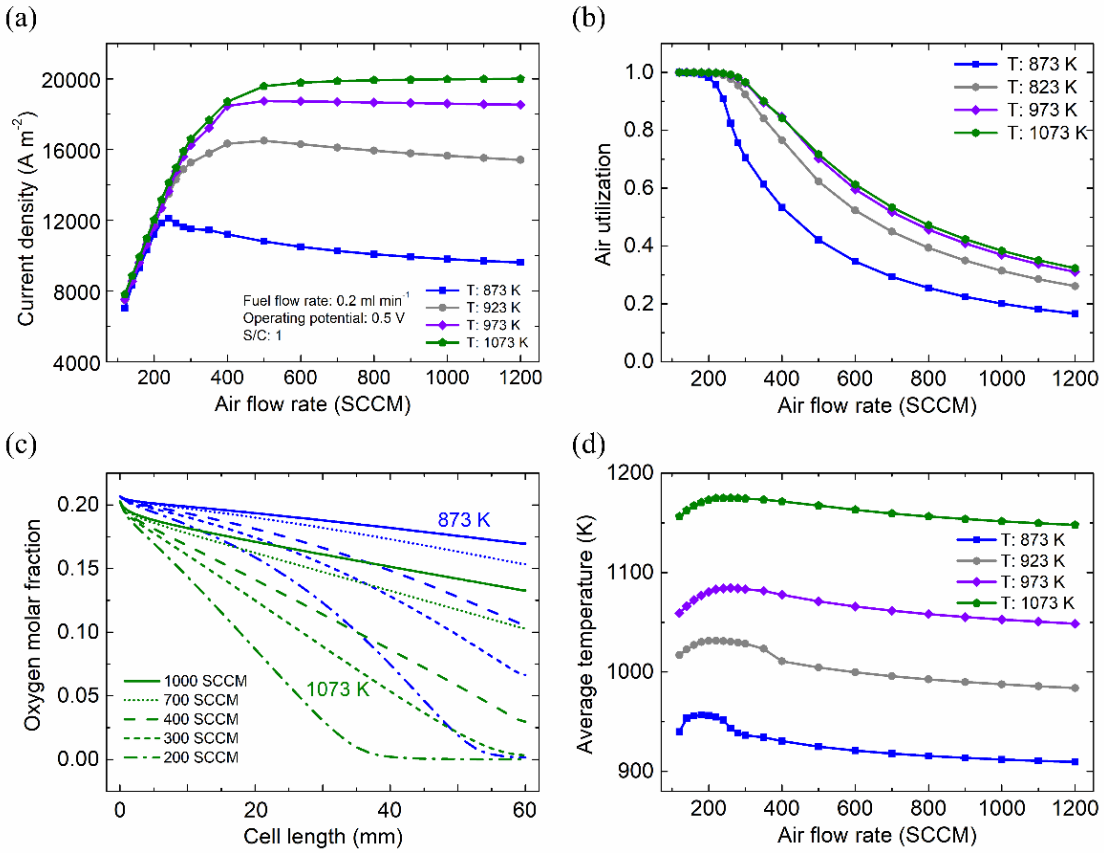

Figure 5.1 The effects of air flow rate on (a) current density; (b) air utilization; (c) oxygen molar fraction distributions along cell length at the middle of cathode; (d) anode-electrolyte-cathode average temperature at different temperatures.

Current densities (Figure 5.1a) are observed to be highly influenced by air flow rate. At a relatively low flow rate, current densities are nearly the same under different temperature conditions and are considerably increased as the air flow rate increases. It is mainly because

cell performance is restricted by insufficient oxygen supply for electrochemical reactions which could be evidenced by the complete consumption of oxygen (Figure 5.1b), especially near the outlet of cathode (Figure 5.1c). With a further increase to 1200 SCCM, the current density at 1073 K continues to be slightly enhanced, while power outputs for three relatively low-temperature conditions experience a gradual drop when the flow rate approximately exceeds a certain air flow rate (240 SCCM for 873 K, 500 SCCM for both 923 K and 973 K). These two different trends for cell performance are reasonable since relevant phenomena could be found in the available literature. With the increase in air flow rate or air ratio, decreased cell performance was frequently observed in several simulation studies from Xu et al. (973 K) [119] and Li et al. (973 K) [120], while enhanced power densities were also achieved with the rise of air flow rate in research works investigated by Colpan et al. (1173 K) [121] and Raj et al. (1073 K) [122]. The possible reason for these two opposite phenomena is because of different cell sensitivities to temperature change. At low operating temperatures, cell performance is more sensitive to temperature variation since as indicated in Figure 5.1a, a temperature increase by 50 K from 873 K leads to a substantial current density improvement (about 5800 A m^{-2}), while cell electrochemical performance at 1073 K is just 1400 A m^{-2} higher compared to the condition of 973 K. Therefore, despite increased oxygen concentration and thus decreased overpotential, the decrease of cell average temperature (Figure 5.1d) caused by cooling air dominates the power output at conditions of 873 K, 923 K and 973 K, causing the drop of cell performance. On the other hand, high operating temperature weakens the negative effect of average temperature decrease, which results in the insignificant continuous increase of power output when the air flow rate is faster than 500 SCCM at 1073 K.

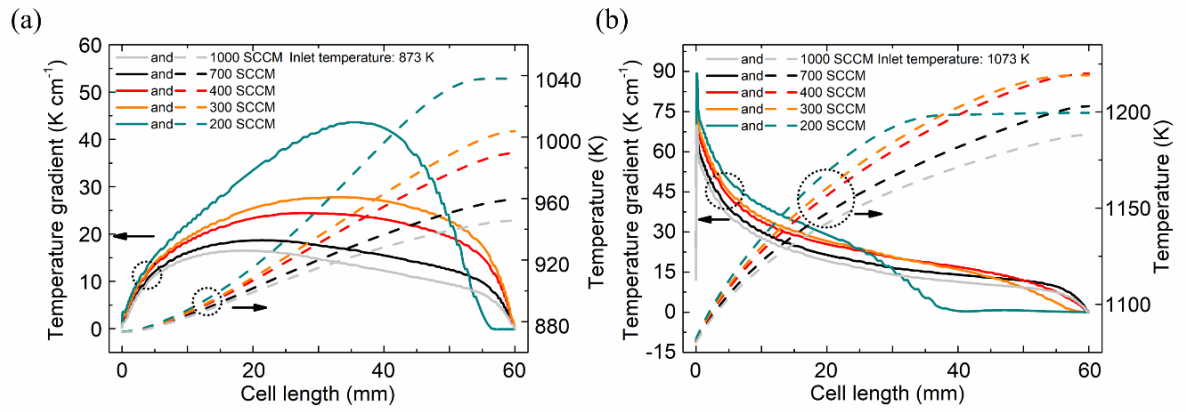

Figure 5.2 The effects of air flow rate on axial temperature gradient and temperature distributions at the middle of electrolyte at 873 K (a) and 1073 K (b).

In addition, the air flow rate tends to strongly impact cell thermal characteristics involving axial temperature gradient and temperature distributions in the ceramic electrolyte (Figure 5.2a and b). For the condition of 873 K, the peak temperature gradient approximately occurs at the middle of electrolyte because of relatively moderate current density (Figure 5.1a) and smooth increase of temperature along cell length near gas inlet (Figure 5.2a). Although limited by the inadequate oxygen and low chemical/electrochemical kinetics due to slow air flow and low operating temperature, respectively, the current density is only about 11000 A m^{-2} at an air flow rate of 200 SCCM, temperature gradient still reaches 43.5 K cm^{-1} because of poor heat convection and easily heat accumulation. Fortunately, with the rise of air flow rate and enhanced flow convective heat transfer capacity, the temperature gradient is found to be effectively suppressed within 20 K cm^{-1}, which could reduce the possibility of structural failure during practical SOFC operation. Besides, reduction of current density also plays a role in the control of high temperature gradient (Figure 5.1a), especially at the high air flow rate, since it is believed that various heat sources are strongly dependent on current density. It is observed that different from the distribution at 873 K, the largest axial temperature gradient is likely to exist near fuel inlet when the fuel cell is operated at 1073 K (Figure 5.2b), which is primarily because high operating temperature benefits the generations of direct fuels (hydrogen and

carbon monoxide), electrochemical reactions and YSZ electrolyte ion transport, leading to extreme elevated current density and thus huge temperature rising near fuel inlet (Figure 5.2b). Although increased air flow rate ensures sufficient oxygen supplement (Figure 5.1c) and enhanced power generation (Figure 5.1a), induced strong heat convection still helps to promote the heat dissipation under 1073 K, slightly improving temperature uniformity and reducing peak temperature gradient.

As the air flow rate continuously increases, mitigations of high temperature and peak temperature gradient seem to become continuously negligible for both operating temperature conditions (Figure 5.2a and b), which indicates that heat convective capacity arising from air flow is likely to show limited cooling effect on the exothermic cell when the air flow rate exceeds a certain value. Therefore, to better evaluate the effectiveness of this active cooling strategy, the excess air ratio is introduced to represent the actual air flow rate [107]. As can be observed from Figure 5.3, all peak temperature gradients show two stages with the increase of excess air ratio (air flow rate: 200-2400 SCCM), involving sudden and then gradual declines. At 1073 K, tripling the air ratio from 2 to 6 merely results in about an 18% reduction of the maximum temperature gradient, which demonstrates that the local high temperature gradient is unlikely to be efficiently eliminated to a safe value (less than 10 K cm^{-1} [100,123]) by simply increasing air flow rate at such high current density (0.5 V), especially for high-temperature conditions, which is consistent with Promsen's statement [107]. The underlying cause for the poor cooling effect of air flow could be the restricted heat convection between cell assembly and convective gas flow in the air channel, as evidenced by the heat transfer mechanism in cathode [116]. Different from the anode where heat generated from the thin interface is principally transported by mass transfer since convective flow resulting from mass exchange moves away from the anode functional layer [124], heat conduction serves as the predominant form of heat transfer in the cathode because air flows towards the cathode functional layer.

Besides, it is reported that the dimensionless number of π_z which characterizes the comparison of heat convection to conduction is 1.075 for anode which is 3 orders higher compared to the cathode. Therefore, simply accelerating the convective flow in the air channel could not be the most effective strategy to control temperature and temperature gradient within the safe region. Besides, an additional air flow normally comes with a cost [122] since it is reported that more than 10% of total cell electricity generation will be consumed by air blower devices [102,105,125]. Therefore, the air flow rate needs to be carefully controlled with considering material deterioration, structural integrity as well as cell efficiency.

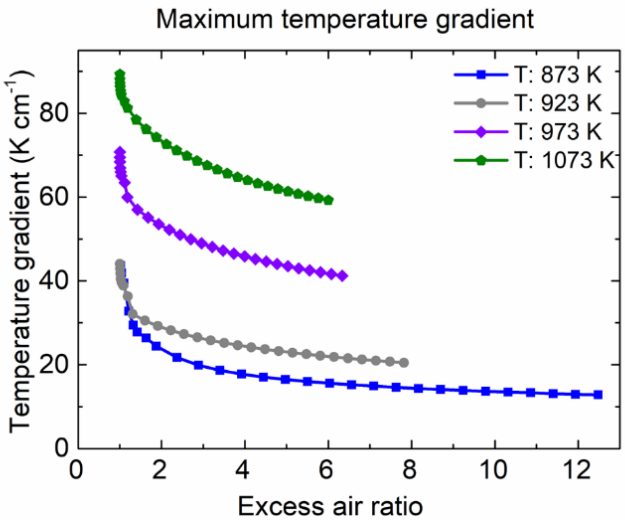

Figure 5.3 The effect of excess air ratio on maximum axial temperature gradient at the middle of electrolyte under different temperatures.

5.4.2 The effects of operating potential

As the key factor, the operating potential is expected to have a dramatic effect on thermal characteristics. The effects of operating potential at different temperatures are illustrated in Figure 5.4. Due to the endothermic methanol decomposition reaction, electrolyte temperature decreases initially and subsequently increases because of the synergistic promotion effects between local current density and actual cell temperature downstream. A local cooling spot near the gas inlet results in an abrupt fall of the axial temperature gradient, especially at a relatively high operating potential (Figure 5.4a and b). Localized low temperature could

negatively influence the current density (Figure 5.4c and d), contributing little to cell electrical performance, and the induced temperature gradient (-60 K cm^{-1}) is not within the safe area for long-term stable operation based on the recommendation value (10 K cm^{-1}) of maximum temperature gradient [100,123], increasing the failure possibility related to structural defects such as cracks and delamination given the applied thermal stress on the brittle ceramic structure. Fortunately, the peak temperature gradient caused by internal reforming operation could be effectively inhibited by properly adjusting operating potential, as it is found that free condition of extreme high positive or negative peak temperature gradient could be achieved between 0.5 and 0.6 V for the temperature of 873 K as well as 0.6 and 0.7 V at 1073 K (Figure 5.4a and b), achieving localized thermal neutral state. Therefore, an unbearable temperature gradient could be avoided by selecting suitable operating conditions for the fuel cell without sacrificing too much power generation since excessive heat generated from cell inefficiency could be consumed by endothermic decomposition reaction, showing an efficient and attractive operation of direct internal reforming in SOFC.

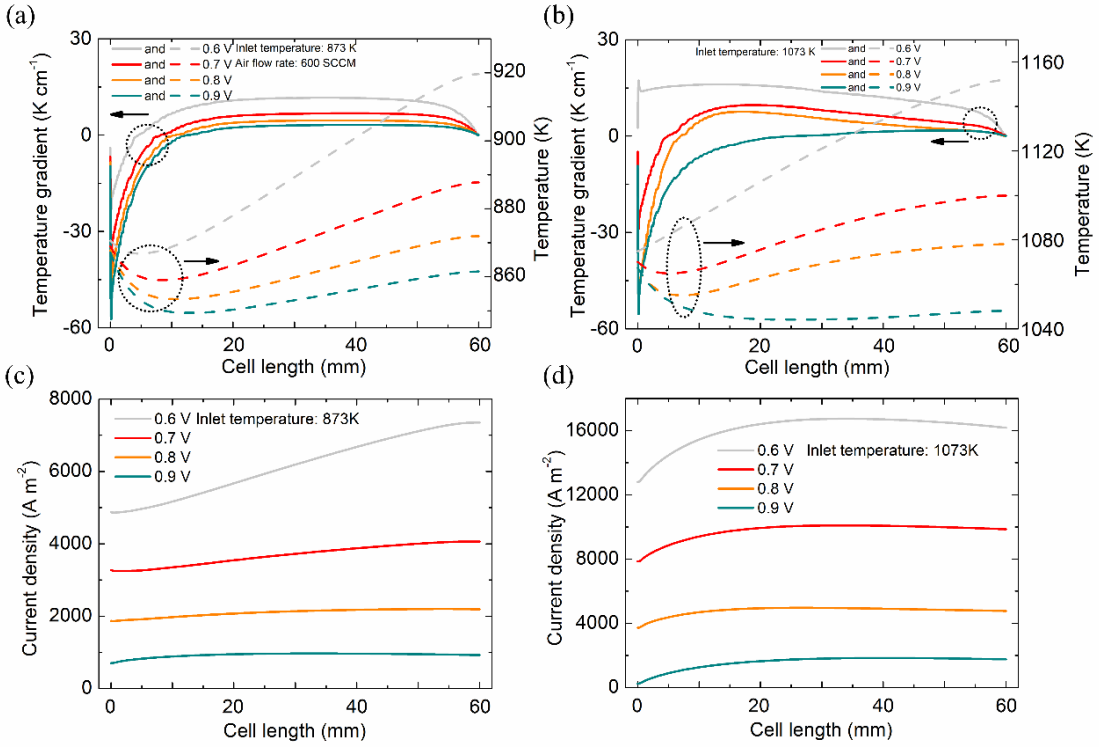

Figure 5.4 The effects of operating potential on axial temperature gradient and temperature

(a, b) as well as local current density (c, d) distributions at the middle of electrolyte under different temperatures of 873 K (a, c) and 1073 K (b, d).

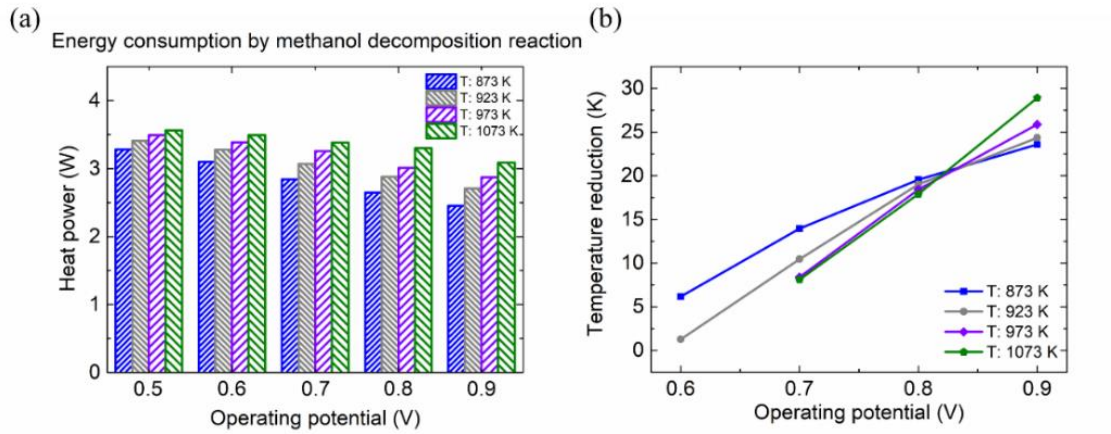

Figure 5.5 The effects of operating potential on: (a) energy consumption by endothermic methanol decomposition reaction; (b) maximum temperature reduction at the middle of electrolyte under different temperatures.

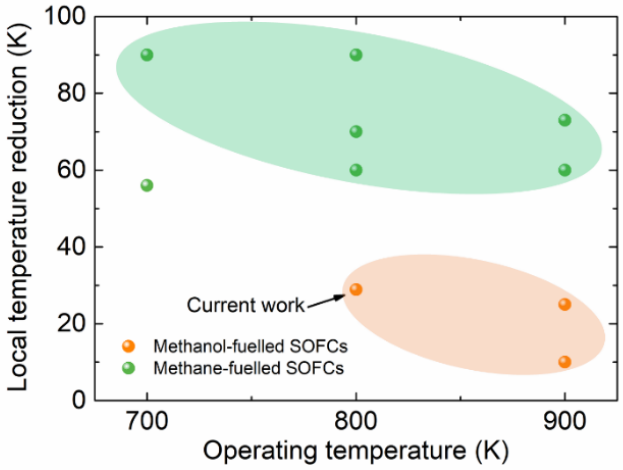

Figure 5.6 The comparison of local temperature reduction due to internal reforming reactions between methanol and methane-fuelled SOFCs [71,123,126–130].

In addition, temperature reduction near cell inlet induced by methanol decomposition reaction could also be affected. It is found that high operating temperature and low potential tend to favour the decomposition reaction (Figure 5.5a), which mainly arises from high reaction kinetics and promotion effects of hydrogen and carbon monoxide consumptions by faradic processes, respectively. Besides, despite high average current density at a high working

temperature, a more favoured endothermic reaction leads to a large temperature drop when the operating potential is 0.9 V (Figure 5.5b). In addition, different from frequently reported research studies that cells operated on methane fuel normally experienced large temperature drops, relatively lower temperature reduction (less than 30 K) is found in the present model, as demonstrated in Figure 5.6. Dokmaingam et al. have drawn a similar conclusion that methanol-fuelled IIR-SOFC (indirect internal reforming) provided the smoothest temperature change among various promising fuels including methane, biogas, methanol and ethanol [126]. The potential reason is related to different thermodynamical intensities of internal reforming reactions. Within the actual working temperature of SOFC (from 1000 K to 1200 K), the methanol decomposition reaction is moderately endothermic since associated reaction heat consumption is about 105 kJ mol^{-1}, while methane steam (226 kJ mol^{-1}) and dry (260 kJ mol^{-1}) reforming processes are highly endothermic [8,71]. Therefore, compared to methane reforming reactions, the methanol decomposition reaction is less endothermic and could lead to a lower temperature drop, which is beneficial to cell performance and durability especially when the fuel cell is operated at start-up or partial load condition, showing a very promising prospect of methanol as the fuel for SOFCs from thermodynamical perspective.

5.4.3 The effects of air inlet temperature

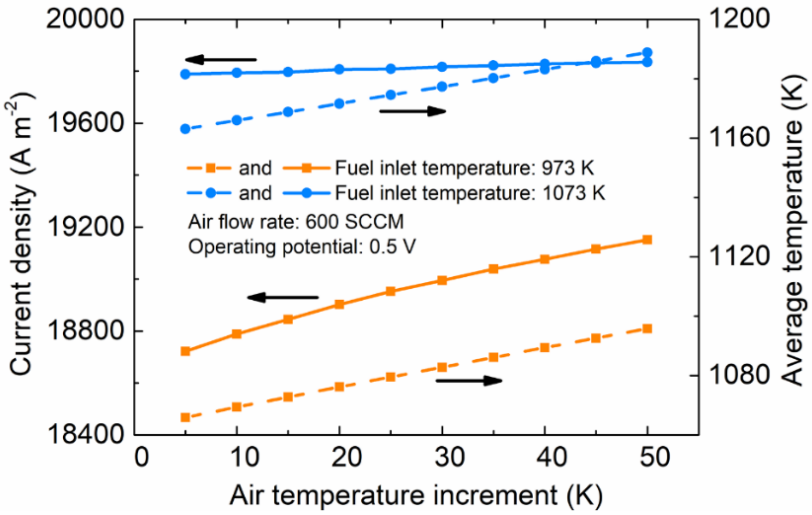

Figure 5.7. The effect of air temperature increment on electrochemical performance and the

average temperature of anode-electrolyte-cathode at 973 K and 1073 K.

Besides the cathode gas flow rate, the air inlet temperature is also likely to influence cell performance and thermal features. Therefore, the effects of cathode gas temperature are studied at fuel gas inlet temperatures of 973 K and 1073 K.

With the rising of air inlet temperature, calculated current densities are observed to increase because of the increased average temperature of cell assembly, as given in Figure 5.7. Besides, it is straightforward to understand that the current density at 973 K experiences a larger improvement in comparison to the condition of 1073 K because of higher cell sensitivity to temperature change, as demonstrated previously. Importantly, it is surprising that a small amount of air temperature increment tends to decrease the peak axial temperature gradient of electrolyte to some extent near the inlet (Figure 5.8a and b). For example, increasing air temperature by 5 K could reduce temperature gradients by about 18% for 973 K and 20% for 1073 K. However, with a further increase, the negative peak temperature gradient is likely to appear because of newly generated low-temperature spot, especially for large air temperature increments. The reason for the reduction of the peak temperature gradient is that warmer air flow tends to serve as a heat source to heat the front end of cell assembly, which could lead to the gradually gentle temperature increase at the corresponding position (Figure 5.8a and b), smoothing temperature gradient distributions, while excessive warmer air flow could cause a low-temperature spot because of heat transfer between the air stream and cell assembly when temperature difference becomes larger than 30 K, creating a new negative peak temperature gradient. Meanwhile, a comparable positive peak temperature gradient could also be formed in the subsequent position at 973 K, and this is mainly because of enhanced local current density in upstream (Figure 5.8c). Besides, low molar fractions of effective fuels in the anode (Figure 5.8d) due to the improved cell performance cause a more rapid drop of local current density downstream for high temperature increments of air (Figure 5.8c), which could lower heat

generation and thus temperature gradient. Compared to the condition of 973 K, the cell with a fuel inlet temperature of 1073 K achieves better control of temperature gradient since a small amount of air temperature increase could lead to more temperature gradient reduction and a further increment could not result in both huge negative and positive gradients because of higher current density and less cell sensitivity to temperature change, respectively.

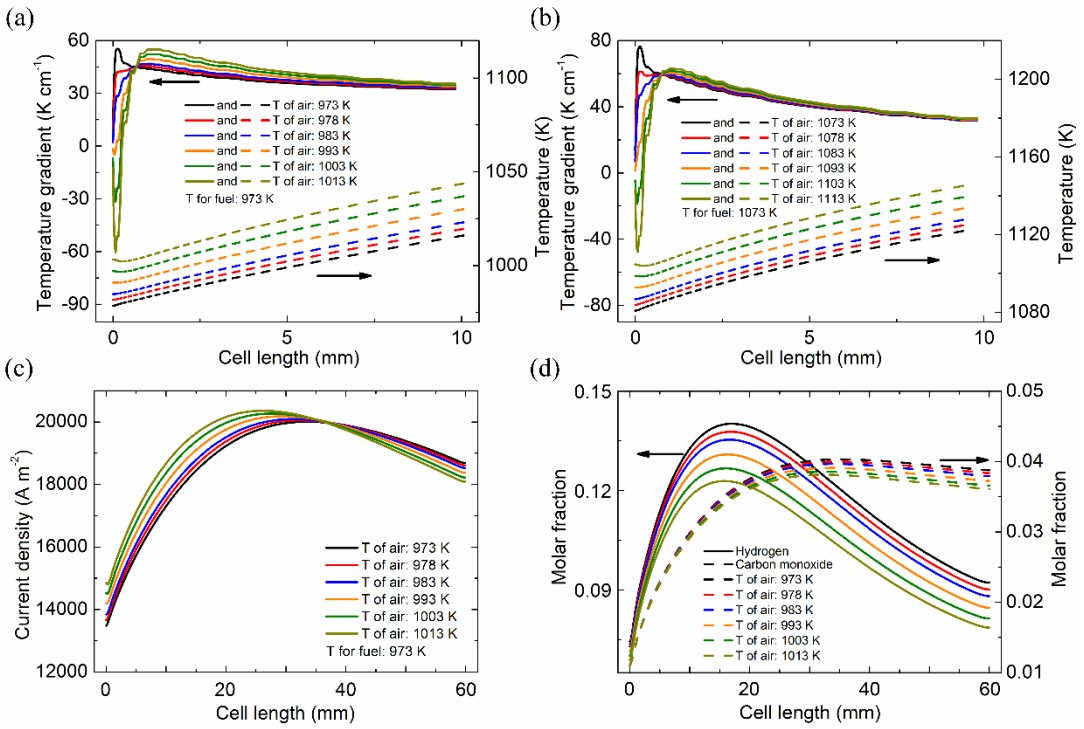

Figure 5.8 The effects of air temperature increment on axial temperature and temperature gradient distributions at the middle of electrolyte at 973 K (a) and 1073 K (b) in cell upstream (0 to 10 mm); (c) local current density distribution along cell length; (d) molar fractions of H_2 and CO along cell length at the middle of anode at 973 K.

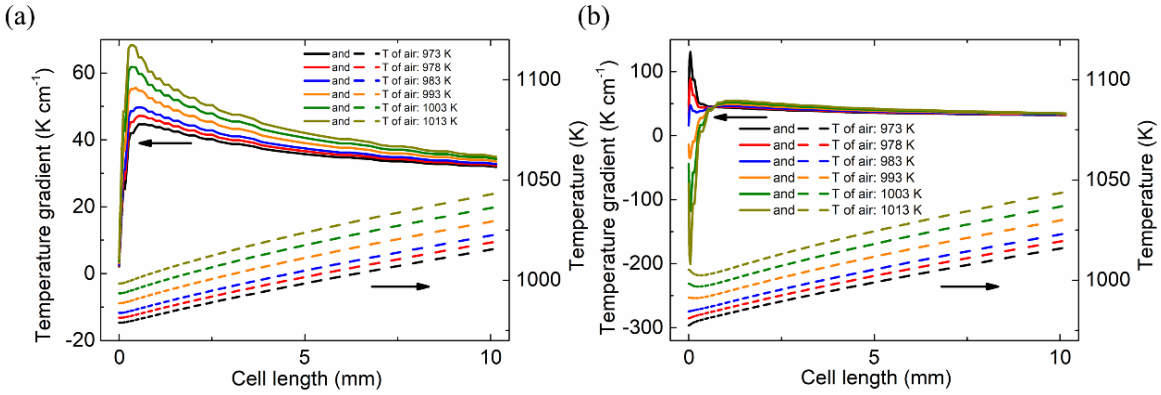

Figure 5.9 The effects of air temperature increment on axial temperature and temperature gradient distributions at the middle of the anode (a) and cathode (b) in cell upstream (0 to 10 mm) at 973 K.

However, the increase in air inlet temperature is likely to have a complicated effect on the temperature gradients of other components (Figure 5.9). Given the anode-supported structure used in this model, an increase in air temperature brings about the rise rather than reduction of temperature gradient for anode mainly because of the relatively long distance to the air channel and enhanced exothermic processes. On the other hand, a larger gradient drop could be observed in the cathode since cathode is the component with the shortest distance to the air channel. Therefore, different temperature effects on anode and cathode indicates that distance to the air channel palys a dominant role in temperature gradient change.

In general, simply increasing the temperature of incoming air could help to reduce the peak temperature gradient of electrolyte and thereby structural failure possibility since it is frequently reported that maximum tensile stress is likely to exist in the electrolyte of SOFC, especially for internal reforming operation [108–110,131,132], which makes electrolyte the most vulnerable component in practice. However, some attention should be given to the negative effects of this approach on other important components as it is shown that it is a trading-off in temperature gradient changes at different radial positions.

5.4.4 The effects of fuel/air flow arrangements

Table 5.2 Cell thermal and electrochemical characteristics comparison between different flow arrangements at 973 K.

Properties	Co-flow	Counter-flow
Current density (A m^{-2})	18722	19878
Maximum temperature (K)	1125.5	1129.4
Minimum temperature (K)	978.63	1014.4
Average temperature (K)	1066.4	1102.4
Maximum temperature gradient (K cm^{-1})	57.45	-382.58/136.66

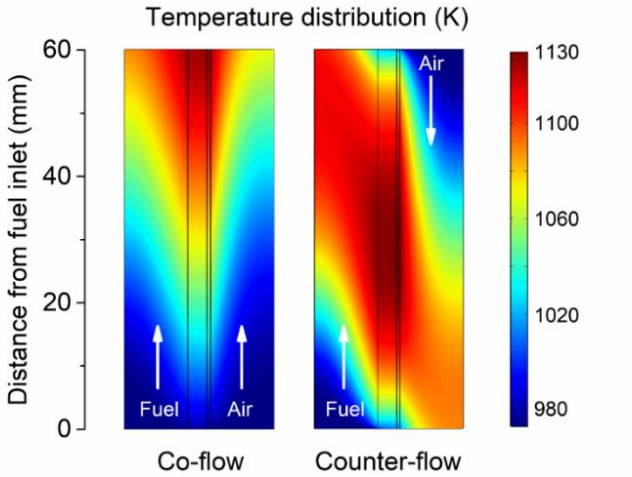

Figure 5.10 Cell temperature distributions of different flow arrangements at 973 K.

Flow arrangements of a tubular fuel cell, including co-flow and counter-flow, are critically important to cell electrochemical characteristics and thereby thermal management, so cells with different air flow directions are simulated to assess the heat dissipation capacity at 973 K and 0.5 V. As indicated in Figure 5.10, a distinctive discrepancy of temperature distributions is that cell with count-flow setup exhibits a larger high-temperature area compared to co-flow counterpart, especially in fuel inlet region where reforming reaction is primarily performed, which could produce more effective fuels for faradic processes, indicating more efficient waste heat recovery for endothermic decomposition reaction. Besides, a much higher average cell assembly temperature of 1102.4 K enables the count-flow cell to perform better, leading to higher current density (Table 5.2). Therefore, the cell with the counter-flow arrangement is characterised by higher power output and thereby efficiency, which coincides with many research works [97,110,121,123,133,134] from literature. However, a large high-temperature area is caused by poor heat dissipation because opposite directions of air and fuel flows diminish heat convection capacity, causing heat accumulation near the cell centre.

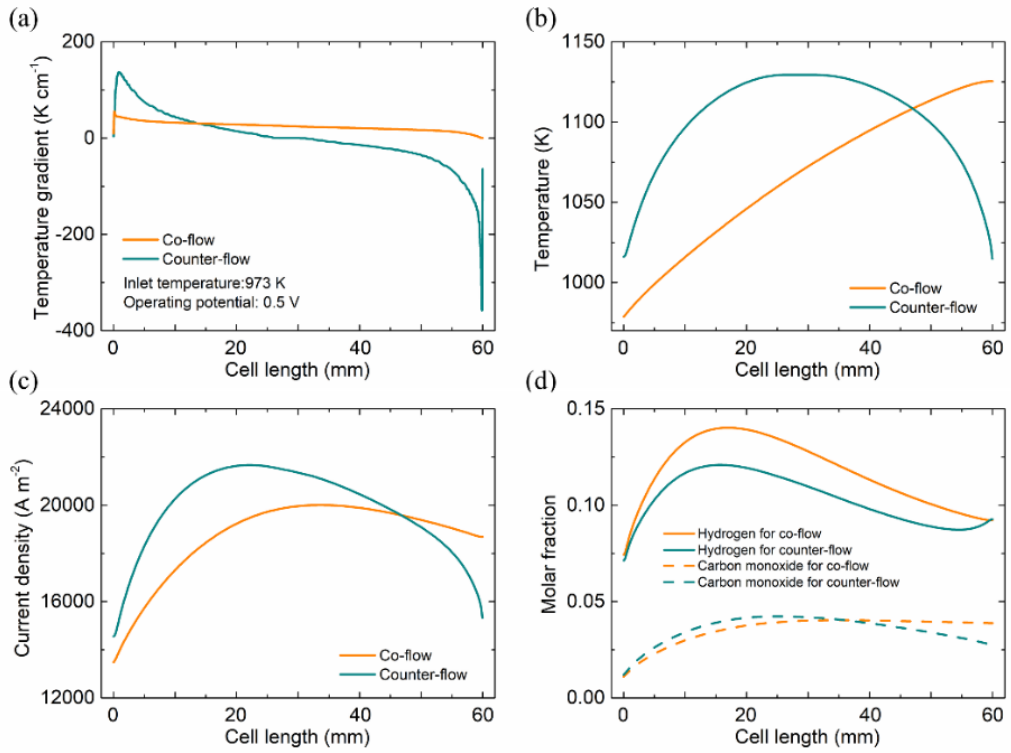

Figure 5.11 The axial temperature gradient (a), temperature (b) and current density (c) distributions of different flow arrangements along cell length at the middle of electrolyte; (d) molar fractions of H_2 and CO along cell length at the middle of anode under 973 K.

Quite different temperature distributions between these two configurations are sure to cause disparate temperature gradient distributions, as given in Figure 5.11. In addition to a higher positive peak gradient (136.66 K cm^{-1}) near the fuel inlet, a negative one (-382.58 K cm^{-1}) is also found near the air inlet for the counter-flow setting, which is because axial temperature tends to decrease from the cell centre (Figure 5.11b) due to the combined effects of cooler incoming air as well as decreased local current density (Figure 5.11c) that is evidenced by the slight increase of hydrogen fuel near air inlet (Figure 5.11d). Besides, it should be noted that the absolute value of the negative peak gradient is much higher than the positive one, which is mainly because the rate of temperature drop at the air inlet is higher compared to the temperature rising rate near the fuel inlet due to the anode-supported structure used in current model as well as the more rapid drop of current density near air inlet than current density

enhancement near fuel inlet (Figure 5.11c). Therefore, the co-flow configuration has a safer temperature profile, while much higher temperature gradients could be found in both fuel and air inlets for the counter-flow counterpart.

Radial temperature and temperature gradient distributions of cell assembly have not been discussed frequently due to negligible temperature variation along thickness direction since relatively high thermal conductivities enable solid materials to conduct heat efficiently. For the co-flow arrangement, the radial temperature difference is less than 1 K (Figure 5.12) because fuel and air flows follow the same temperature variation pattern, leading to relatively small temperature gradients at three typical positions (Figure 5.13). However, temperature along cell thickness exhibits different tendencies at different axial positions for counter-flow setting (Figure 5.12), showing opposite temperature changes at fuel and air inlets. Besides, relatively high gradient intensity (-60.5 K cm^{-1}) could be found at the interface of electrolyte and cathode near air inlet (fuel outlet) (Figure 5.13a), which is again because anode supportive structure enables the electrolyte to dissipate heat more rapidly through thin cathode near air inlet.

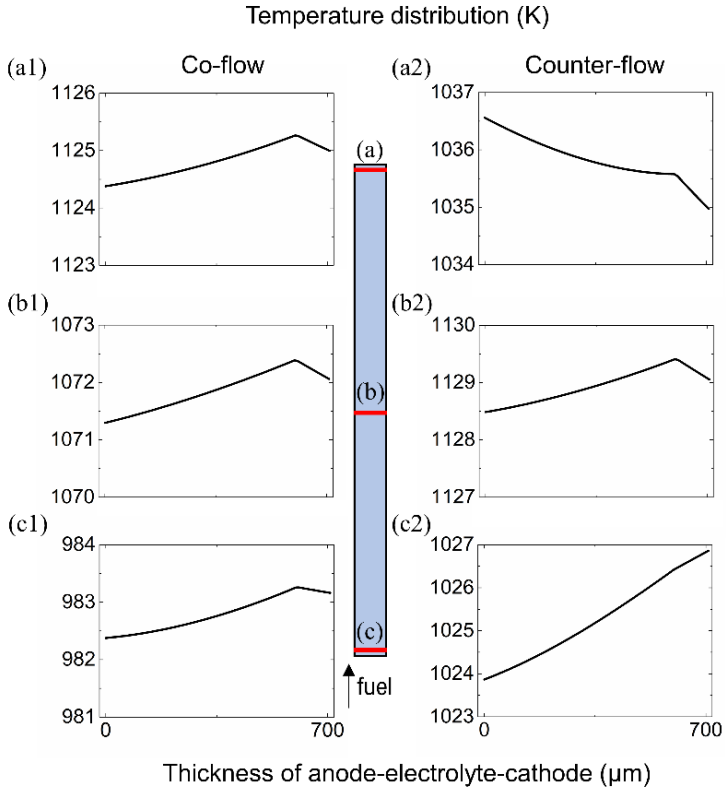

Figure 5.12 Radial temperature distributions at three positions of the cell under 973 K (a: 59 mm, b: 30 mm and c: 1 mm from fuel inlet).

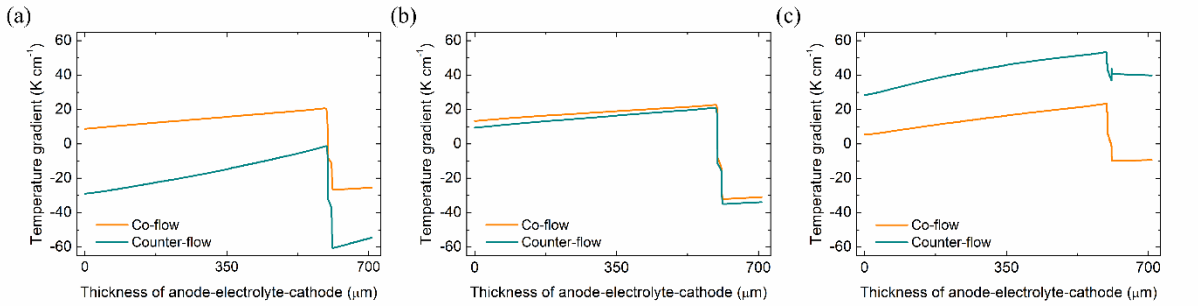

Figure 5.13 Radial temperature gradient distributions at three positions of the cell at 973 K (a: 59 mm, b: 30 mm and c: 1 mm from fuel inlet).

5.5 Chapter Conclusions

The developed two-dimensional axisymmetric model studies the thermal and electrochemical characteristics of tubular SOFC fed by equal molar amounts of methanol and steam. This validated numerical model fully considers mass and heat transfer processes, hydrogen/carbon monoxide electrochemical oxidations, as well as methanol conversion, and simulates the cell thermo-fluid environment under various working conditions, involving operating potential, air flow rate inlet temperature and gas flow arrangements. The main conclusions are as follows:

(1) Air flow rate tends to have a complicated effect on cell performance. Limited by the insufficient oxygen at relatively low air flow rates, current densities are found to be increased dramatically with the rise of air flow rate. However, with the further increase, power output experiences a gradual drop because of induced temperature decrease at conditions of 873 K, 923 K and 973 K, but a slight increase at 1073 K given the low cell sensitivity to temperature variation. Besides, as an active cooling strategy, the oversupply of cathode air could not effectively suppress the detrimental thermal features to a safe level due to the intrinsic heat transfer in the cathode at a considerably high current density.

(2) Because of the thermal coupling of cell inefficiencies as well as endothermic decomposition reaction, a localized thermal neutral state could be achieved by suitably adjusting operating potential, eliminating the peak axial temperature gradient of electrolyte. Compared to methane-fuelled SOFCs, SOFC operated on methanol fuel experiences a less temperature reduction (less than 30 K) near fuel inlet as a result of a less endothermic thermodynamical nature, causing fewer negative effects on cell performance and durability.

(3) Interestingly, increasing air inlet temperature by 5 K could suppress peak axial temperature gradients by about 18% at 973 K and 20% at 1073 K since warmer fresh air is likely to work as the heat source to heat the front end of fuel cell, while a further increase could lead to the generations of negative and positive temperature gradient peaks because of new cooling spot and elevated current density, respectively. However, as the result of anode supportive structure, increased air inlet temperature tends to have different effects on other components, increasing the failure possibility correspondingly.

(4) Different from the cell with a co-flow arrangement, high temperature concentrates at the cell centre for counter-flow counterpart, leading to enhanced electricity output and cell efficiency. However, because of poor heat dissipation capacity and enhanced heat generation, the cell with a counter-flow setting is characterized by higher local temperature gradients not only along cell length but the radial direction, making the counter-flow undesirable from the perspective of thermal stability.

Chapter 6: Conclusions and Outlook

6.1 Conclusions

Methanol is used as the primary fuel in this research work due to its various promising features, such as storage/transportation conveniences, relatively high volumetric energy density and importantly low coking threat. Based on the validated numerical model with considering hydrogen/carbon monoxide electrochemical oxidations and methanol conversion, detailed analyses of electrical, chemical and thermal characteristics of methanol-fuelled SOFC are conducted. The main conclusions are as follows:

Firstly, a simulation model without considering the heat transfer is developed to study a tubular SOFC running on the pure methanol. At a temperature of 1073K, a comparable peak power density (1.3 W cm^{-2}) to hydrogen fuel could be achieved, showing more favourable benefits to room temperature direct methanol fuel cells. The effects of operating and structural parameters on the SOFC characteristics are subsequently conducted involving inlet temperature, potential, anode thickness and cell length. The increase in inlet temperature is likely to enhance SOFC performance by facilitating the chemical and electrochemical reactions as well as ion conduction. Current density and gas composition are all significantly influenced by the operating potential. Longer cell and thicker anode are able to benefits the fuel conversion because of more catalyst sites for methanol decomposition reaction, while longer cell and too thicker anode could inevitably decrease cell performance due to gradual consumption of direct fuels and possible increased fuel diffusion resistance. Therefore, the anode with the thickness of 600 μm is considered for further thermal investigations based on the structural optimazition.

Secondly, to prevent carbon deposition in SOFC anode, the fuel mixture of steam and methanol is supplied to conduct the thermo-electrochemical modelling. Due to the dilution effect of steam on methanol fuel and the generated syngas, the increase in S/C tends to reduce

the electrical power and total heat generation. Besides, faster fuel and air flows show beneficial effects on electrochemical performance and cooling strategy. However, side effects are low fuel conversion and additional energy input, which could negatively affect the system efficiency. In addition to performance enhancement, The rise of inlet temperature from 898 K to 1173 K could contribute to the reduction of heat generation because of the improved ion conduction and electrode reaction kinetics, leading to more uniform temperature distribution.

Thirdly, despite thermal coupling of endothermic methanol decomposition with cell inefficiencies, thermal management is a challenging issue given the non-uniform temperature distribution and convective flows within SOFCs. Therefore, thermal responses of methanol-fuelled SOFC with focusing on the temperature gradient is investigated. Results show that despite large heat convection capacity, excessive air could not effectively suppress the harmful temperature gradient to a safe level due to the intrinsic heat transfer in the cathode at a considerably high current density. Fortunately, well control of current density by properly selecting operating potential could result in a local thermal neutral state, eliminating the peak axial temperature gradient of electrolyte. Thanks to less endothermic thermodynamical nature of methanol decomposition reaction, SOFC fuelled by methanol fuel experiences a less temperature reduction (less than 30 K) near the fuel inlet compared to methane-fuelled SOFCs. Interestingly, the maximum axial temperature gradient could be reduced by about 18% at 973 K and 20% at 1073 K when the air with a 5 K higher temperature is supplied. Also, despite the higher electrochemical performance observed, the cell with a counter-flow arrangement featured by a larger hot area and higher maximum temperature gradients is not preferable for a ceramic SOFC system considering thermal durability.

6.2 Outlook

Although this research work numerically gives a comprehensive understanding of the methanol-fuelled SOFC related to the performance enhancement and optimizations of cell structure and operating parameters, there are still several aspects to be studied in the future.

The thermal coupling of reforming reaction and electrochemical reaction could largely enhance the system efficiency, but rapid reforming reactions, especially in the high catalytic effect of the metal-based anode, may lead to severe local cooling that causes the steep thermal gradients, mechanically damaging the cell system. Meanwhile, anode, cathode, and electrolyte need to be equipped with specific properties by fabricating particular materials, leading to the mismatch of thermodynamic properties, especially the TEC. Therefore, induced thermal stress due to the non-uniform temperature field and TECs mismatch, as well as the fragile nature of ceramic electrolytes will considerably degrade the material and even induce delamination, thus leading to the failure of the whole system. Although the temperature gradient is well studied in chapter 5, it is worth noting that in addition to the temperature gradient, mechanical properties of cell components involving TEC, elasticity, Poisson's ratio etc., are likely to affect cell thermal stress conditions. Therefore, the investigation of thermal stress distribution in the direct methanol-fuelled SOFC is necessary since it is essentially important to avoid the mechanical failure caused by thermal stress and optimize the structural dimensions to improve the whole lifespan of the SOFC system.

Besides, methanol could also be used as the fuel for proton-ion-conductive SOFCs which use proton-conducting oxides as the electrolyte. Compared to the oxygen-conducting electrolyte, the proton-conducting counterpart with lower activation energy is particularly suitable for low-temperature SOFCs. Besides, the decrease in operating temperature could provide numerous benefits to the fuel cell system, such as more components material selection, quick start-up or shut-down time, simpler fabrication processes and mitigation of metal

sintering or other issues. Although it is the proton transferred from the anode to cathode, leaving the carbon monoxide unreacted in the anode side, conventional Ni-based anode is less susceptible to the carbon monoxide environment. Besides, special properties of some typical protonic ceramic materials like doped-$BaCeO_3$ or doped-$BaZrO_3$ may have a positive effect on the mitigation of coking issue. Therefore, the cogeneration of carbon monoxide and electricity could be possible for the methanol-fuelled proton-ion-conductive SOFC. Besides, modelling of methanol-fuelled proton-ion-conductive SOFC could form a basis for gas generation control and electrochemical performance enhancement.

References

[1] Alanne K, Cao S. An overview of the concept and technology of ubiquitous energy. Appl Energy 2019;238:284–302. https://doi.org/10.1016/j.apenergy.2019.01.100.

[2] Liao T, He Q, Xu Q, Dai Y, Cheng C, Ni M. Performance evaluation and optimization of a perovskite solar cell-thermoelectric generator hybrid system. Energy 2020;201. https://doi.org/10.1016/j.energy.2020.117665.

[3] Jurasz J, Canales FA, Kies A, Guezgouz M, Beluco A. A review on the complementarity of renewable energy sources: Concept, metrics, application and future research directions. Sol Energy 2020;195:703–24. https://doi.org/10.1016/j.solener.2019.11.087.

[4] Ni M, Leung DYC, Leung MKH. A review on reforming bio-ethanol for hydrogen production. Int J Hydrogen Energy 2007;32:3238–47. https://doi.org/10.1016/j.ijhydene.2007.04.038.

[5] Dawood F, Anda M, Shafiullah GM. Hydrogen production for energy: An overview. Int J Hydrogen Energy 2020;45:3847–69. https://doi.org/10.1016/j.ijhydene.2019.12.059.

[6] Perera F. Pollution from fossil-fuel combustion is the leading environmental threat to global pediatric health and equity: Solutions exist. Int J Environ Res Public Health 2018;15. https://doi.org/10.3390/ijerph15010016.

[7] Gür TM. Comprehensive review of methane conversion in solid oxide fuel cells: Prospects for efficient electricity generation from natural gas. Prog Energy Combust Sci 2016;54:1–64. https://doi.org/10.1016/j.pecs.2015.10.004.

[8] Cimenti M, Hill JM. Direct utilization of liquid fuels in SOFC for portable applications: Challenges for the selection of alternative anodes. Energies 2009;2:377–410. https://doi.org/10.3390/en20200377.

[9] Boldrin P, Brandon NP. Progress and outlook for solid oxide fuel cells for transportation applications. Nat Catal 2019;2:571–7. https://doi.org/10.1038/s41929-019-0310-y.

[10] McIntosh S, Gorte RJ. Direct hydrocarbon solid oxide fuel cells. Chem Rev 2004;104:4845–65. https://doi.org/10.1021/cr020725g.

[11] Badwal SPS, Giddey S, Kulkarni A, Goel J, Basu S. Direct ethanol fuel cells for transport and stationary applications - A comprehensive review. Appl Energy 2015;145:80–103. https://doi.org/10.1016/j.apenergy.2015.02.002.

[12] Shri Prakash B, Senthil Kumar S, Aruna ST. Properties and development of Ni/YSZ as an anode material in solid oxide fuel cell: A review. Renew Sustain Energy Rev 2014;36:149–79. https://doi.org/10.1016/j.rser.2014.04.043.

[13] Hosseinpour J, Sadeghi M, Chitsaz A, Ranjbar F, Rosen MA. Exergy assessment and optimization of a cogeneration system based on a solid oxide fuel cell integrated with a Stirling engine. Energy Convers Manag 2017;143:448–58. https://doi.org/10.1016/j.enconman.2017.04.021.

[14] Garcia RF, Carril JC, Gomez JR, Gomez MR. Energy and entropy analysis of closed adiabatic expansion based trilateral cycles. Energy Convers Manag 2016;119:49–59. https://doi.org/10.1016/j.enconman.2016.04.031.

[15] Khan MS, Lee SB, Song RH, Lee JW, Lim TH, Park SJ. Fundamental mechanisms involved in the degradation of nickel–yttria stabilized zirconia (Ni–YSZ) anode during solid oxide fuel cells operation: A review. Ceram Int 2016;42:35–48. https://doi.org/10.1016/j.ceramint.2015.09.006.

[16] da Silva FS, de Souza TM. Novel materials for solid oxide fuel cell technologies: A literature review. Int J Hydrogen Energy 2017;42:26020–36. https://doi.org/10.1016/j.ijhydene.2017.08.105.

[17] Gao Z, Mogni L V., Miller EC, Railsback JG, Barnett SA. A perspective on low-temperature solid oxide fuel cells. Energy Environ Sci 2016;9:1602–44. https://doi.org/10.1039/c5ee03858h.

[18] Dwivedi S. Solid oxide fuel cell: Materials for anode, cathode and electrolyte. Int J Hydrogen Energy 2020;45:23988–4013. https://doi.org/10.1016/j.ijhydene.2019.11.234.

[19] Shu L, Sunarso J, Hashim SS, Mao J, Zhou W, Liang F. Advanced perovskite anodes for solid oxide fuel cells: A review. Int J Hydrogen Energy 2019;44:31275–304. https://doi.org/10.1016/j.ijhydene.2019.09.220.

[20] Abdalla AM, Hossain S, Azad AT, Petra PMI, Begum F, Eriksson SG, et al. Nanomaterials for solid oxide fuel cells: A review. Renew Sustain Energy Rev 2018;82:353–68. https://doi.org/10.1016/j.rser.2017.09.046.

[21] Fergus JW. Electrolytes for solid oxide fuel cells. J Power Sources 2006;162:30–40. https://doi.org/10.1016/j.jpowsour.2006.06.062.

[22] Ling Y, Wang X, Ma Z, Wei K, Wu Y, Khan M, et al. Review of experimental and modelling developments for ceria-based solid oxide fuel cells free from internal short circuits. J Mater Sci 2020;55:1–23. https://doi.org/10.1007/s10853-019-03876-z.

[23] Jacobson AJ. Materials for solid oxide fuel cells. Chem Mater 2010;22:660–74. https://doi.org/10.1021/cm902640j.

[24] Chen Y, Yang L, Ren F, An K. Visualizing the structural evolution of LSM/xYSZ composite cathodes for SOFC by in-situ neutron diffraction. Sci Rep 2014;4. https://doi.org/10.1038/srep05179.

[25] Wang SF, Hsu YF, Chang JH, Cheng S, Lu HC. Characteristics of Cu and Mo-doped Ca3Co4O9-δ cathode materials for use in solid oxide fuel cells. Ceram Int 2016;42:11239–47. https://doi.org/10.1016/j.ceramint.2016.04.037.

[26] Hwang HJ, Moon JW, Lee S, Lee EA. Electrochemical performance of LSCF-based composite cathodes for intermediate temperature SOFCs. J Power Sources 2005;145:243–8. https://doi.org/10.1016/j.jpowsour.2005.02.063.

[27] Shao Z, Haile SM. A high-performance cathode for the next generation of solid-oxide fuel cells. Nature 2004;431:170–3. https://doi.org/10.1038/nature02863.

[28] Koide H, Someya Y, Yoshida T, Maruyama T. Properties of Ni/YSZ cermet as anode for SOFC. Solid State Ionics 2000;132:253–60. https://doi.org/10.1016/s0167-2738(00)00652-4.

[29] Kawada T, Sakai N, Yokokawa H, Dokiya M, Mori M, Iwata T. Characteristics of Slurry‐Coated Nickel Zirconia Cermet Anodes for Solid Oxide Fuel Cells. J Electrochem Soc 1990;137:3042–7. https://doi.org/10.1149/1.2086156.

[30] Wei K, Wang X, Budiman RA, Kang J, Lin B, Zhou F, et al. Progress in Ni-based anode materials for direct hydrocarbon solid oxide fuel cells. J Mater Sci 2018;53:8747–65. https://doi.org/10.1007/s10853-018-2205-8.

[31] Wang W, Su C, Wu Y, Ran R, Shao Z. Progress in solid oxide fuel cells with nickel-based anodes operating on methane and related fuels. Chem Rev 2013;113:8104–51. https://doi.org/10.1021/cr300491e.

[32] Marbán G, Valdés-Solís T. Towards the hydrogen economy? Int J Hydrogen Energy 2007;32:1625–37. https://doi.org/10.1016/j.ijhydene.2006.12.017.

[33] Van Mierlo J, Maggetto G, Lataire P. Which energy source for road transport in the future? A comparison of battery, hybrid and fuel cell vehicles. Energy Convers Manag 2006;47:2748–60. https://doi.org/10.1016/j.enconman.2006.02.004.

[34] Granovskii M, Dincer I, Rosen MA. Economic and environmental comparison of conventional, hybrid, electric and hydrogen fuel cell vehicles. J Power Sources 2006;159:1186–93. https://doi.org/10.1016/j.jpowsour.2005.11.086.

[35] Dincer I. Green methods for hydrogen production. Int J Hydrogen Energy 2012;37:1954–71. https://doi.org/10.1016/j.ijhydene.2011.03.173.

[36] Balat H, Kirtay E. Hydrogen from biomass - Present scenario and future prospects. Int J Hydrogen Energy 2010;35:7416–26. https://doi.org/10.1016/j.ijhydene.2010.04.137.

[37] Hosseini SE, Wahid MA. Hydrogen production from renewable and sustainable energy resources: Promising green energy carrier for clean development. Renew Sustain Energy Rev 2016;57:850–66. https://doi.org/10.1016/j.rser.2015.12.112.

[38] Nikolaidis P, Poullikkas A. A comparative overview of hydrogen production processes. Renew Sustain Energy Rev 2017;67:597–611. https://doi.org/10.1016/j.rser.2016.09.044.

[39] Kothari R, Buddhi D, Sawhney RL. Comparison of environmental and economic aspects of various hydrogen production methods. Renew Sustain Energy Rev 2008;12:553–63. https://doi.org/10.1016/j.rser.2006.07.012.

[40] Abdalla AM, Hossain S, Nisfindy OB, Azad AT, Dawood M, Azad AK. Hydrogen production, storage, transportation and key challenges with applications: A review. Energy Convers Manag 2018;165:602–27. https://doi.org/10.1016/j.enconman.2018.03.088.

[41] Acar C, Dincer I. The potential role of hydrogen as a sustainable transportation fuel to combat global warming. Int J Hydrogen Energy 2020;45:3396–406. https://doi.org/10.1016/j.ijhydene.2018.10.149.

[42] Shao Z, Haile SM, Ahn J, Ronney PD, Zhan Z, Barnett SA. A thermally self-sustained micro solid-oxide fuel-cell stack with high power density. Nature 2005;435:795–8. https://doi.org/10.1038/nature03673.

[43] Hibino T, Hashimoto A, Inoue T, Tokuno JI, Yoshida SI, Sano M. A low-operating-temperature solid oxide fuel cell in hydrocarbon-air mixtures. Science (80-) 2000;288:2031–3. https://doi.org/10.1126/science.288.5473.2031.

[44] Park S, Vohs JM, Gorte RJ. Direct oxidation of hydrocarbons in a solid-oxide fuel cell. Nature 2000;404:265–7. https://doi.org/10.1038/35005040.

[45] Perry Murray E, Tsai T, Barnett SA. A direct-methane fuel cell with a ceria-based anode. Nature 1999;400:649–51. https://doi.org/10.1038/23220.

[46] Yang BC, Koo J, Shin JW, Go D, Shim JH, An J. Direct Alcohol-Fueled Low-Temperature Solid Oxide Fuel Cells: A Review. Energy Technol 2019;7:5–19. https://doi.org/10.1002/ente.201700777.

[47] Wang W, Qu J, Julião PSB, Shao Z. Recent Advances in the Development of Anode Materials for Solid Oxide Fuel Cells Utilizing Liquid Oxygenated Hydrocarbon Fuels: A Mini Review. Energy Technol 2019;7:33–44. https://doi.org/10.1002/ente.201700738.

[48] Cimenti M, Alzate-Restrepo V, Hill JM. Direct utilization of methanol on impregnated Ni/YSZ and Ni-Zr0.35Ce0.65O2/YSZ anodes for solid oxide fuel cells. J Power Sources 2010;195:4002–12. https://doi.org/10.1016/j.jpowsour.2009.12.119.

[49] Elharati MA, Dewa M, Bkour Q, Mohammed Hussain A, Miura Y, Dong S, et al. Internal Reforming Solid Oxide Fuel Cell System Operating under Direct Ethanol Feed Condition. Energy Technol 2020;8:1–11. https://doi.org/10.1002/ente.202000350.

[50] Dalena F, Senatore A, Marino A, Gordano A, Basile M, Basile A. Methanol Production and Applications: An Overview. Elsevier B.V.; 2018. https://doi.org/10.1016/B978-0-444-63903-5.00001-7.

[51] Bozzano G, Manenti F. Efficient methanol synthesis: Perspectives, technologies and optimization strategiesa. Prog Energy Combust Sci 2016;56:71–105. https://doi.org/10.1016/j.pecs.2016.06.001.

[52] Palo DR, Dagle RA, Holladay JD. Methanol steam reforming for hydrogen production. Chem Rev 2007;107:3992–4021. https://doi.org/10.1021/cr050198b.

[53] Cimenti M, Hill JM. Thermodynamic analysis of solid oxide fuel cells operated with methanol and ethanol under direct utilization, steam reforming, dry reforming or partial oxidation conditions. J Power Sources 2009;186:377–84. https://doi.org/10.1016/j.jpowsour.2008.10.043.

[54] Sasaki K, Watanabe K, Teraoka Y. Direct-Alcohol SOFCs: Current-Voltage Characteristics and Fuel Gas Compositions. J Electrochem Soc 2004;151:A965. https://doi.org/10.1149/1.1756884.

[55] Jiang Y, Virkar A V. A High Performance, Anode-Supported Solid Oxide Fuel Cell Operating on Direct Alcohol. J Electrochem Soc 2001;148:A706. https://doi.org/10.1149/1.1375166.

[56] Liu M, Peng R, Dong D, Gao J, Liu X, Meng G. Direct liquid methanol-fueled solid oxide fuel cell. J Power Sources 2008;185:188–92. https://doi.org/10.1016/j.jpowsour.2008.06.076.

[57] Meng X, Zhan Z, Liu X, Wu H, Wang S, Wen T. Low-temperature ceria-electrolyte solid oxide fuel cells for efficient methanol oxidation. J Power Sources 2011;196:9961–4. https://doi.org/10.1016/j.jpowsour.2011.08.002.

[58] Qu J, Wang W, Chen Y, Wang F, Ran R, Shao Z. Ethylene glycol as a new sustainable fuel for solid oxide fuel cells with conventional nickel-based anodes. Appl Energy 2015;148:1–9. https://doi.org/10.1016/j.apenergy.2015.03.051.

[59] Eigenbrodt BC, Pomfret MB, Steinhurst DA, Owrutsky JC, Walker RA. Direct, in situ optical studies of Ni-YSZ anodes in solid oxide fuel cells operating with methanol and methane. J Phys Chem C 2011;115:2895–903. https://doi.org/10.1021/jp109292r.

[60] Jeon OS, Lee JG, Ji Y, Lee SH, Kwon O, Kim JP, et al. Effects of dispersed copper nanoparticles on Ni-ceria based dry methanol fuelled low temperature solid oxide fuel cells. RSC Adv 2019;9:6320–7. https://doi.org/10.1039/c8ra07586g.

[61] Saunders GJ, Preece J, Kendall K. Formulating liquid hydrocarbon fuels for SOFCs. J Power Sources 2004;131:23–6. https://doi.org/10.1016/j.jpowsour.2004.01.040.

[62] Lin Y, Zhan Z, Liu J, Barnett SA. Direct operation of solid oxide fuel cells with methane fuel. Solid State Ionics 2005;176:1827–35. https://doi.org/10.1016/j.ssi.2005.05.008.

[63] Jang DY, Koo J, Choi HR, Kim JW, Jeong HJ, Prinz FB, et al. Coke-Free Oxidation of Methanol in Solid Oxide Fuel Cells with Heterogeneous Nickel-Palladium Catalysts Prepared by Atomic Layer Deposition. ACS Sustain Chem Eng 2020;8:10529–35. https://doi.org/10.1021/acssuschemeng.0c03020.

[64] Ru Y, Sang J, Xia C, Wei WCJ, Guan W. Durability of direct internal reforming of methanol as fuel for solid oxide fuel cell with double-sided cathodes. Int J Hydrogen Energy 2020;45:7069–76. https://doi.org/10.1016/j.ijhydene.2019.12.222.

[65] Laosiripojana N, Assabumrungrat S. Catalytic steam reforming of methane, methanol, and ethanol over Ni/YSZ: The possible use of these fuels in internal reforming SOFC. J Power Sources 2007;163:943–51. https://doi.org/10.1016/j.jpowsour.2006.10.006.

[66] Li P, Wang R, Yan F. Effect of Pr addition into Ni based anode on direct methanol fueled solid oxide fuel cell. J Electroanal Chem 2020;859:113846. https://doi.org/10.1016/j.jelechem.2020.113846.

[67] Yao X, Fan L, Gan T, Hou N, Li P, Zhao Y, et al. Coking-resistant NbOx-Ni-Ce0.8Sm0.2O1.9 anode material for methanol-fueled solid oxide fuel cells. Int J Hydrogen Energy 2018;43:12748–55. https://doi.org/10.1016/j.ijhydene.2018.03.186.

[68] Li P, Fang L, Hou N, Li J, Yao X, Gan T, et al. Improved Performance of Ni-Mo Based Anode for Direct Methanol Solid Oxide Fuel Cells with the Addition of Rare Earth Oxides. J Electrochem Soc 2017;164:F1142–8. https://doi.org/10.1149/2.1021712jes.

[69] Li P, Yu B, Li J, Yao X, Zhao Y, Li Y. Improved activity and stability of Ni-Ce0.8Sm0.2O1.9 anode for solid oxide fuel cells fed with methanol through addition of molybdenum. J Power Sources 2016;320:251–6. https://doi.org/10.1016/j.jpowsour.2016.04.100.

[70] Ding G, Gan T, Yu J, Li P, Yao X, Hou N, et al. Carbon-resistant Ni1-xCox-Ce0.8Sm0.2O1.9 anode for solid oxide fuel cells fed with methanol. Catal Today 2017;298:250–7. https://doi.org/10.1016/j.cattod.2017.03.060.

[71] Ni M. Modeling and parametric simulations of solid oxide fuel cells with methane carbon dioxide reforming. Energy Convers Manag 2013;70:116–29. https://doi.org/10.1016/j.enconman.2013.02.008.

[72] Mizsey P, Newson E, Truong T binh, Hottinger P. The kinetics of methanol decomposition: A part of autothermal partial oxidation to produce hydrogen for fuel cells. Appl Catal A Gen 2001;213:233–7. https://doi.org/10.1016/S0926-860X(00)00907-8.

[73] Haberman BA, Young JB. Three-dimensional simulation of chemically reacting gas flows in the porous support structure of an integrated-planar solid oxide fuel cell. Int J Heat Mass Transf 2004;47:3617–29. https://doi.org/10.1016/j.ijheatmasstransfer.2004.04.010.

[74] Xu Q, Ni M. Modelling of high temperature direct methanol solid oxide fuel cells. Int J Energy Res 2021;45:3097–112. https://doi.org/10.1002/er.6003.

[75] Ni M. Modeling of SOFC running on partially pre-reformed gas mixture. Int J Hydrogen Energy 2012;37:1731–45. https://doi.org/10.1016/j.ijhydene.2011.10.042.

[76] Ni M. An electrochemical model for syngas production by co-electrolysis of H 2 O and CO 2. J Power Sources 2012;202:209–16. https://doi.org/10.1016/j.jpowsour.2011.11.080.

[77] Xu H, Chen B, Zhang H, Kong W, Liang B, Ni M. The thermal effect in direct carbon solid oxide fuel cells. Appl Therm Eng 2017. https://doi.org/10.1016/j.applthermaleng.2017.03.027.

[78] Chen B, Xu H, Tan P, Zhang Y, Xu X, Cai W, et al. Thermal modelling of ethanol-fuelled Solid Oxide Fuel Cells. Appl Energy 2019;237:476–86. https://doi.org/10.1016/j.apenergy.2019.01.025.

[79] Krishna R, Wesselingh JA. The Maxwell-Stefan approach to mass tranfer. Chem Eng Sci 1997;52:861–911. https://doi.org/10.1016/S0009-2509(96)00458-7.

[80] Vural Y, Ma L, Ingham DB, Pourkashanian M. Comparison of the multicomponent mass transfer models for the prediction of the concentration overpotential for solid oxide fuel cell anodes. J Power Sources 2010;195:4893–904. https://doi.org/10.1016/j.jpowsour.2010.01.033.

[81] Evans RB, Watson GM, Mason EA. Gaseous diffusion in porous media at uniform pressure. J Chem Phys 1961;35:2076–83. https://doi.org/10.1063/1.1732211.

[82] Todd B, Young JB. Thermodynamic and transport properties of gases for use in solid oxide fuel cell modelling. J Power Sources 2002;110:186–200. https://doi.org/10.1016/S0378-7753(02)00277-X.

[83] Veldsink JW, van Damme RMJ, Versteeg GF, van Swaaij WPM. The use of the dusty-gas model for the description of mass transport with chemical reaction in porous media. Chem Eng J Biochem Eng J 1995;57:115–25. https://doi.org/10.1016/0923-0467(94)02929-6.

[84] Poling BE, Prausnitz JM, O'Connell JP, Reid RC, Sherwood TK, Street RE. The properties of gases and liquids. vol. 12. 2001. https://doi.org/10.1063/1.3060771.

[85] Coker AK. Ludwig's Applied Process Design for Chemical and Petrochemical Plants. Gulf Prof Publ 2007. https://doi.org/10.1016/B978-0-7506-7766-0.X5000-3.

[86] Luo Y, Shi Y, Li W, Cai N. Comprehensive modeling of tubular solid oxide electrolysis cell for co-electrolysis of steam and carbon dioxide. Energy 2014;70:420–34. https://doi.org/10.1016/j.energy.2014.04.019.

[87] He Q, Yu J, Xu H, Zhao D, Zhao T, Ni M. Thermal effects in H2O and CO2 assisted direct carbon solid oxide fuel cells. Int J Hydrogen Energy 2020;45:12459–75. https://doi.org/10.1016/j.ijhydene.2020.02.169.

[88] Wiranarongkorn K, Banerjee A, Deutschmann O, Arpornwichanop A. Performance analysis and temperature gradient of solid oxide fuel cell stacks operated with bio-oil sorption-enhanced steam reforming. Int J Hydrogen Energy 2020;45:12108–20. https://doi.org/10.1016/j.ijhydene.2020.02.120.

[89] Xu H, Chen B, Liu J, Ni M. Modeling of direct carbon solid oxide fuel cell for CO and electricity cogeneration. Appl Energy 2016;178:353–62. https://doi.org/10.1016/j.apenergy.2016.06.064.

[90] Shi Y, Li C, Cai N. Experimental characterization and mechanistic modeling of carbon monoxide fueled solid oxide fuel cell. J Power Sources 2011;196:5526–37. https://doi.org/10.1016/j.jpowsour.2011.02.013.

[91] Lawlor V. Review of the micro-tubular solid oxide fuel cell (Part II: Cell design issues and research activities). J Power Sources 2013;240:421–41. https://doi.org/10.1016/j.jpowsour.2013.03.191.

[92] Ni M, Leung MKH, Leung DYC. Parametric study of solid oxide fuel cell performance. Energy Convers Manag 2007;48:1525–35. https://doi.org/10.1016/j.enconman.2006.11.016.

[93] Cimenti M, Hill JM. Importance of pyrolysis and catalytic decomposition for the direct utilization of methanol in solid oxide fuel cells. J Power Sources 2010;195:54–61. https://doi.org/10.1016/j.jpowsour.2009.07.007.

[94] Gao Z, Raza R, Zhu B, Mao Z. Development of methanol-fueled low-temperature solid oxide fuel cells. Int J Energy Res 2011;35:690–6. https://doi.org/10.1002/er.1718.

[95] Neelakandan S, Liu D, Wang L, Hu M, Wang L. Highly branched poly(arylene ether)/surface functionalized fullerene-based composite membrane electrolyte for DMFC applications. Int J Energy Res 2019;43:3756–67. https://doi.org/10.1002/er.4536.

[96] Munjewar SS, Thombre SB, Mallick RK. Approaches to overcome the barrier issues of passive direct methanol fuel cell – Review. Renew Sustain Energy Rev 2017;67:1087–104. https://doi.org/10.1016/j.rser.2016.09.002.

[97] Wang Y, Zhan R, Qin Y, Zhang G, Du Q, Jiao K. Three-dimensional modeling of pressure effect on operating characteristics and performance of solid oxide fuel cell. Int J Hydrogen Energy 2018;43:20059–76. https://doi.org/10.1016/j.ijhydene.2018.09.025.

[98] Liu X, Martin CL, Bouvard D, Di Iorio S, Laurencin J, Delette G. Strength of highly porous ceramic electrodes. J Am Ceram Soc 2011;94:3500–8. https://doi.org/10.1111/j.1551-2916.2011.04669.x.

[99] Yakabe H, Baba Y, Sakurai T, Yoshitaka Y. Evaluation of the residual stress for anode-supported SOFCs. J Power Sources 2004;135:9–16. https://doi.org/10.1016/j.jpowsour.2003.11.049.

[100] Zeng Z, Qian Y, Zhang Y, Hao C, Dan D, Zhuge W. A review of heat transfer and thermal management methods for temperature gradient reduction in solid oxide fuel cell (SOFC) stacks. Appl Energy 2020;280:115899. https://doi.org/10.1016/j.apenergy.2020.115899.

[101] Hubert M, Laurencin J, Cloetens P, Morel B, Montinaro D, Lefebvre-Joud F. Impact of Nickel agglomeration on Solid Oxide Cell operated in fuel cell and electrolysis modes. J Power Sources 2018;397:240–51. https://doi.org/10.1016/j.jpowsour.2018.06.097.

[102] Zeng H, Wang Y, Shi Y, Cai N, Yuan D. Highly thermal integrated heat pipe-solid oxide fuel cell. Appl Energy 2018;216:613–9. https://doi.org/10.1016/j.apenergy.2018.02.040.

[103] Zhang T, Zhu Q, Huang WL, Xie Z, Xin X. Stress field and failure probability analysis for the single cell of planar solid oxide fuel cells. J Power Sources 2008;182:540–5. https://doi.org/10.1016/j.jpowsour.2008.04.027.

[104] Dikwal CM, Bujalski W, Kendall K. The effect of temperature gradients on thermal cycling and isothermal ageing of micro-tubular solid oxide fuel cells. J Power Sources 2009;193:241–8. https://doi.org/10.1016/j.jpowsour.2009.01.097.

[105] Dillig M, Plankenbühler T, Karl J. Thermal effects of planar high temperature heat pipes in solid oxide cell stacks operated with internal methane reforming. J Power Sources 2018;373:139–49. https://doi.org/10.1016/j.jpowsour.2017.11.007.

[106] Marocco P, Ferrero D, Lanzini A, Santarelli M. Benefits from heat pipe integration in H2/H2O fed SOFC systems. Appl Energy 2019;241:472–82. https://doi.org/10.1016/j.apenergy.2019.03.037.

[107] Promsen M, Komatsu Y, Sciazko A, Kaneko S, Shikazono N. Feasibility study on saturated water cooled solid oxide fuel cell stack. Appl Energy 2020;279:115803. https://doi.org/10.1016/j.apenergy.2020.115803.

[108] Wang Y, Ren J, Shi Y, Li X. Numerical Model of Direct Internal Reforming SOFC: A Comparison between Anode-Support and Metal-Support. ECS Trans 2019;91:2013–22. https://doi.org/10.1149/09101.2013ecst.

[109] Ren J, Wang Y, Shi Y. Numerical simulation and thermal stress analysis of direct internal reforming SOFCs. Int J Green Energy 2021;00:1–11. https://doi.org/10.1080/15435075.2021.1946817.

[110] Selimovic A, Kemm M, Torisson T, Assadi M. Steady state and transient thermal stress analysis in planar solid oxide fuel cells. J Power Sources 2005;145:463–9. https://doi.org/10.1016/j.jpowsour.2004.11.073.

[111] Zhan R, Wang Y, Ni M, Zhang G, Du Q, Jiao K. Three-dimensional simulation of solid oxide fuel cell with metal foam as cathode flow distributor. Int J Hydrogen Energy 2020;45:6897–911. https://doi.org/10.1016/j.ijhydene.2019.11.221.

[112] Park J, Kim YM, Bae J. A numerical study on the heat and mass transfer characteristics of metal-supported solid oxide fuel cells. Int J Hydrogen Energy 2011;36:3167–78. https://doi.org/10.1016/j.ijhydene.2010.11.111.

[113] Tucker MC. Progress in metal-supported solid oxide fuel cells: A review. J Power Sources 2010;195:4570–82. https://doi.org/10.1016/j.jpowsour.2010.02.035.

[114] Tucker MC. Development of High Power Density Metal-Supported Solid Oxide Fuel Cells. Energy Technol 2017;5:2175–81. https://doi.org/10.1002/ente.201700242.

[115] Dogdibegovic E, Wang R, Lau GY, Tucker MC. High performance metal-supported solid oxide fuel cells with infiltrated electrodes. J Power Sources 2019;410–411:91–8. https://doi.org/10.1016/j.jpowsour.2018.11.004.

[116] Lee S, Park M, Kim H, Yoon KJ, Son JW, Lee JH, et al. Thermal conditions and heat transfer characteristics of high-temperature solid oxide fuel cells investigated by three-dimensional numerical simulations. Energy 2017;120:293–305. https://doi.org/10.1016/j.energy.2016.11.084.

[117] Xu Q, Xia L, He Q, Guo Z, Ni M. Thermo-electrochemical modelling of high temperature methanol-fuelled solid oxide fuel cells. Appl Energy 2021;291:116832. https://doi.org/10.1016/j.apenergy.2021.116832.

[118] Zheng K, Sun Q, Ni M. Local Non-Equilibrium Thermal Effects in Solid Oxide Fuel Cells with Various Fuels. Energy Technol 2013;1:35–41. https://doi.org/10.1002/ente.201200014.

[119] Xu H, Ma J, Tan P, Chen B, Wu Z, Zhang Y, et al. Towards online optimisation of solid oxide fuel cell performance: Combining deep learning with multi-physics simulation. Energy AI 2020;1:100003. https://doi.org/10.1016/j.egyai.2020.100003.

[120] Li Y, Yan H, Zhou Z, Wu WT. Three-dimensional nonisothermal modeling of solid oxide fuel cell coupling electrochemical kinetics and species transport. Int J Energy Res 2019;43:6907–21. https://doi.org/10.1002/er.4707.

[121] Colpan CO, Hamdullahpur F, Dincer I. Transient heat transfer modeling of a solid oxide fuel cell operating with humidified hydrogen. Int J Hydrogen Energy 2011;36:11488–99. https://doi.org/10.1016/j.ijhydene.2010.11.127.

[122] Raj A, Sasmito AP, Shamim T. Numerical investigation of the effect of operating parameters on a planar solid oxide fuel cell. Energy Convers Manag 2015;90:138–45. https://doi.org/10.1016/j.enconman.2014.10.055.

[123] Aguiar P, Adjiman CS, Brandon NP. Anode-supported intermediate temperature direct internal reforming solid oxide fuel cell. I: Model-based steady-state performance. J Power Sources 2004;138:120–36. https://doi.org/10.1016/j.jpowsour.2004.06.040.

[124] Lee S, Kim H, Yoon KJ, Son JW, Lee JH, Kim BK, et al. The effect of fuel utilization on heat and mass transfer within solid oxide fuel cells examined by three-dimensional numerical simulations. Int J Heat Mass Transf 2016;97:77–93. https://doi.org/10.1016/j.ijheatmasstransfer.2016.02.001.

[125] Fardadi M, McLarty DF, Jabbari F. Investigation of thermal control for different SOFC flow geometries. Appl Energy 2016;178:43–55. https://doi.org/10.1016/j.apenergy.2016.06.015.

[126] Dokmaingam P, Assabumrungrat S, Soottitantawat A, Laosiripojana N. Modelling of tubular-designed solid oxide fuel cell with indirect internal reforming operation fed by different primary fuels. J Power Sources 2010;195:69–78. https://doi.org/10.1016/j.jpowsour.2009.06.102.

[127] Dokamaingam P, Assabumrungrat S, Soottitantawat A, Laosiripojana N. Effect of operating conditions and gas flow patterns on the system performances of IIR-SOFC fueled by methanol. Int J Hydrogen Energy 2009;34:6415–24. https://doi.org/10.1016/j.ijhydene.2009.05.105.

[128] Iwai H, Yamamoto Y, Saito M, Yoshida H. Numerical simulation of intermediate-temperature direct-internal-reforming planar solid oxide fuel cell. Energy 2011;36:2225–34. https://doi.org/10.1016/j.energy.2010.03.058.

[129] Ni M. Electrolytic effect in solid oxide fuel cells running on steam/methane mixture. J Power Sources 2011;196:2027–36. https://doi.org/10.1016/j.jpowsour.2010.09.069.

[130] Ho TX, Kosinski P, Hoffmann AC, Vik A. Numerical analysis of a planar anode-supported SOFC with composite electrodes. Int J Hydrogen Energy 2009;34:3488–99. https://doi.org/10.1016/j.ijhydene.2009.02.016.

[131] Severson H, Assadi M. Analysis of residual and operational thermal stresses in a planar SOFC. J Fuel Cell Sci Technol 2013;10:1–14. https://doi.org/10.1115/1.4025051.

[132] Xu M, Li TS, Yang M, Andersson M, Fransson I, Larsson T, et al. Modeling of an anode supported solid oxide fuel cell focusing on thermal stresses. Int J Hydrogen Energy 2016;41:14927–40. https://doi.org/10.1016/j.ijhydene.2016.06.171.

[133] Russner N, Dierickx S, Weber A, Reimert R, Ivers-Tiffée E. Multiphysical modelling of planar solid oxide fuel cell stack layers. J Power Sources 2020;451. https://doi.org/10.1016/j.jpowsour.2019.227552.

[134] Wongchanapai S, Iwai H, Saito M, Yoshida H. Selection of suitable operating conditions for planar anode-supported direct-internal-reforming solid-oxide fuel cell. J Power Sources 2012;204:14–24. https://doi.org/10.1016/j.jpowsour.2011.12.029.